Universidade Estadual de Campinas

Faculdade de Engenharia Elétrica e de Computação

Andres Gil Molina

Nonlinear Optics in Waveguides: Optical Fibers and Silicon Nano-Waveguides

Óptica Não Linear em Guias de Onda: Fibras Ópticas e Nano-Guias de Onda de Silicio

Campinas, SP

2018

Andres Gil Molina

Nonlinear Optics in Waveguides: Optical Fibers and Silicon Nano-Waveguides

Óptica Não Linear em Guias de Onda: Fibras Ópticas e Nano-Guias de Onda de Silicio

Tese apresentada a Faculdade de Engenharia Elétrica e de Computação da Universidade Estadual de Campinas como parte dos requisitos exigidos para a obtenção do título de Doutor em Engenharia Elétrica, na área de Telecomunicações e Telemática.

Thesis Presented to the School of Electrical and Computer Engineering of the University of Campinas in Partial Fulfillment of the Requirements for the Degree of Doctor of Philosophy in Electrical Engineering, in the area of Telecommunications and Telematics.

Supervisor/Orientador: Prof. Dr. Lucas Heitzmann Gabrielli

ESTE EXEMPLAR CORRESPONDE À VERSÃO FINAL DA TESE DE DOUTORADO DEFENDIDA PELO ALUNO ANDRÉS GIL MOLINA E ORIENTADA PELO PROF. DR. LUCAS HEITZMANN GABRIELLI.

Campinas, SP

2018

Agência(s) de fomento e nº(s) de processo(s): CAPES

Ficha catalográfica
Universidade Estadual de Campinas
Biblioteca da Área de Engenharia e Arquitetura
Rose Meire da Silva - CRB 8/5974

G37n

Gil Molina, Andrés, 1986-
Nonlinear optics in waveguides : optical fibers and silicon nano-waveguides / Andrés Gil Molina. – Campinas, SP : [s.n.], 2018.

Orientador: Lucas Heitzmann Gabrielli.
Tese (doutorado) – Universidade Estadual de Campinas, Faculdade de Engenharia Elétrica e de Computação.

1. Fibras óticas. 2. Ótica não-linear. 3. Guias de ondas. 4. Silicio. 5. Fotônica. I. Gabrielli, Lucas Heitzmann, 1982-. II. Universidade Estadual de Campinas. Faculdade de Engenharia Elétrica e de Computação. III. Título.

Informações para Biblioteca Digital

Título em outro idioma: Óptica não linear em guias de onda : fibras ópticas e nano-guias de onda de silicio
Palavras-chave em inglês:
Optical fibers
Nonlinear optics
Waveguide
Silicon
Photonics
Área de concentração: Telecomunicações e Telemática
Titulação: Doutor em Engenharia Elétrica
Banca examinadora:
Lucas Heitzmann Gabrielli [Orientador]
Paulo Clóvis Dainese Junior
Marcelo Eduardo Vieira Segatto
Christiano José Santiago de Matos
Darli Augusto de Arruda Mello
Data de defesa: 07-11-2018
Programa de Pós-Graduação: Engenharia Elétrica

COMISSÃO JULGADORA – TESE DE DOUTORADO

Candidato: Andres Gil Molina

Data da Defesa: 07 de novembro de 2018

Thesis Title: “Nonlinear Optics in Waveguides: Optical Fibers and Silicon Nano-Waveguides”.

Título da Tese: “Óptica Não Linear em Guias de Onda: Fibras Ópticas e Nano-Guias de Onda de Silicio”.

Prof. Dr. Lucas Heitzmann Gabrielli
Prof. Dr. Paulo Clóvis Dainese Junior
Prof. Dr. Marcelo Eduardo Vieira Segatto
Prof. Dr. Christiano José Santiago de Matos
Prof. Dr. Darli Augusto de Arruda Mello

A ata de defesa, com as respectivas assinaturas dos membros da Comissão Julgadora, encontra-se no SIGA (Sistema de Fluxo de Dissertação/Tese) e na Secretaria de PósGraduação da Faculdade de Engenharia Elétrica e de Computação.

This thesis represents years of tremendous effort (physically and mentally), in which discipline and motivation were a great component. I will always be deeply grateful with my family for being that infinite source of motivation, understanding my desires, and giving me all the support along these years. I would like to thank my parents for all the trust and commitment and my brother and sister for the unconditional support. Finally, I would like to thank my wife Paula for her tremendous effort, for always trusting and supporting me, and all the love and affection that have made these years much easier and filled with memorable moments.

Acknowledgements

This thesis represents a personal achievement and was possible due to great cooperative work with a great number of people that gave me inspiration, taught me and supported me in different ways. Here I would like to thank almost everyone that somehow contributed to the development of this thesis.

Firstly, I would like to thank my advisor Prof. Lucas H. Gabrielli for his friendship, support and guidance along these years; for giving me the opportunity of being part of his group and trusting in me and my research interests; for his frequent advices in the numerical modeling, experiments and analysis of results of silicon-photonics and optical fibers; for his invaluable feedback in the elaboration of this thesis; for his enthusiasm and continuous encouragements.

In would like to thank Prof. Hugo L. Fragnito for giving me the opportunity of coming to Brazil and being part of the optical communications laboratory (LCO) at the physics institute; for his friendship, commitment, support and guidance; for the invaluable and extensive trainings at the laboratory; for encouraging me to do challenging experiments; for making me realize the great value of an excellent experimental work; for the unenumerable napkins with valuable theoretical developments; for his trust and being an inspiring person in my life.

I would like to thank Prof. Paulo Dainese for giving me the opportunity of making possible to perform integrated-photonic experiments at the LCO; for his friendship, support and invaluable advices; for his efforts of making a nice environment at the LCO and his commitment with the fruitful group meetings; for his great advices in the experiments and his effort in the theoretical developments of generation and recombination of free-carriers in silicon nano-waveguides; for his trust and being a great example of leadership and hard-work.

I would like to thank Prof. Ivan Aldaya for making us realize that the dynamics of free-carriers was not completely understood in silicon nano-waveguides; for his friendship and fruitful lessons on simulations of pulse propagation, scientific writing, physics, optical communications, history, and so on; for spending a long time in the lab together to figure out how to clean our pump-and-probe experiments; for performing the signal processing of pump-and-probe experiments and giving great ideas in the way we presented our results.

I would like to thank Alexander Perez for introducing me to the experimental work at the LCO and his valuable contributions in the experiments on bent fibers; for his enthusiasm, unconditional friendship and great experiences.

I would like to thank Juan Andres Castañeda for introducing me to the experimental and theoretical work on high-order dispersion mapping by using incoherent pumped Four-Wave Mixing; for his unconditional friendship and numerous talks about physics, economics, life and so on.

I would like to thank Jhonattan Cordoba for receiving me in Brazil; for introducing me to the numerical calculations of fiber dispersion; for performing the numerical calculations of dispersion in bent fibers; for his unconditional friendship and countless coffee-time advices at the quantum-electronics department (DEQ).

I would like to thank Daniel Londoño for performing the numerical calculations of high-order dispersion-mapping experiments including fiber dispersion and pulses propagation; for his friendship and great talks about science and physics.

I would like to thank other friends and colleagues of the LCO fort their support and friendship: Omar, Erick, Paulo Jarschel, Julián, Maicon, Vagner, Francinvaldo, Prof. Diego Marconi, Arthur, Leticia and Lucas. I am sorry if I missed anyone but you know you were important.

I would like to thank DEQ staff: Rosi, Valeria, Julio, Eliane and, obviously, super Simone.

I would like to thank the institutions: FEEC-UNICAMP, IFGW-UNICAMP, FOTONICOM, CEPOF, CAPES, FAPESP, CNPQ.

Abstract

In this thesis we present studies of nonlinear optics in waveguides, particularly, optical fibers and silicon nano-waveguides.

In optical fibers we studied the capabilities of Four-Wave Mixing (FWM) pumped by an incoherent source in the characterization of the zero-dispersion wavelength (ZDW) and high-order dispersion. By means of this FWM-based method we were able to obtain dispersion-maps of a long fiber with a good spatial resolution. Our dispersion-mapping experiments reveal that high-order dispersion presents a higher fluctuation than that of the ZDW. In addition, by improving our experiments we were able to apply our measuring method in a short segment of fiber. This allowed us to study the bending-induced change on dispersion and explain our observations in terms of modifications of the mode confinement and fiber geometry. These studies, not reported before, are fundamental in the development of FWM-based parametric devices and were achieved thanks to an extensive experimental work, numerical modeling of fiber dispersion and nonlinear propagation, and a good understanding of the phase-matching condition of the used FWM process.

Given the possibility to characterize dispersion in short fibers, we numerically explored the application of our FWM-based measuring method in silicon nano-waveguides. We obtained promising results, although neglecting single and two-photon absorption and the effects induced by the generated free carriers. Therefore, we found that the understanding free-carriers effects and their dynamics in silicon nano-waveguides is of crucial importance, not only for the application of our method but also for several studies of nonlinear optical propagation phenomena and applications of all-control of light. Initially, by means of time-resolved pump-and-probe experiments we studied optical carrier generation mechanisms and identified, for the first time, the individual contribution of single and two-photon absorption at telecommunications wavelengths. In addition, our experiments also revealed a complex carrier recombination dynamics, which we explained in terms of trap-assisted recombination. This explanation was not given before in the context of optical nano-waveguides, and is founded by the good qualitative agreement obtained between an implemented theoretical model and the observed dynamics. Our main observations are of crucial importance for several studies of linear and nonlinear propagation phenomena and applications in silicon photonics.

Resumo

Nesta tese apresentamos estudos de óptica não linear em guias de onda, particularmente fibras ópticas e nano-guias de silício.

Em fibras ópticas, estudamos as capacidades da Mistura de Quatro Ondas (FWM) bombeada por uma fonte incoerente na caracterização do comprimento de onda de zero-dispersão (ZDW) e dispersão de alta ordem. Por meio deste método baseado em FWM, conseguimos obter mapas de dispersão de uma fibra longa com boa resolução espacial. Nossos experimentos de mapeamento de dispersão revelam que a dispersão de alta ordem apresenta uma maior flutuação do que aquela do ZDW. Além disso, ao aprimorar nossos experimentos, conseguimos aplicar nosso método de medição num segmento curto de fibra. Isso nos permitiu estudar a mudança induzida por flexão na dispersão e explicar nossas observações em termos de modificações do confinamento de modo e a geometria da fibra. Estes estudos, não apresentados antes, são fundamentais no desenvolvimento de dispositivos paramétricos baseados em FWM e foram alcançados graças a um extenso trabalho experimental, modelagem numérica de dispersão da fibra e propagação não-linear, e uma boa compreensão da condição de casamento de fase do processo de FWM utilizado.

Dada a possibilidade de caracterizar a dispersão em fibras curtas, exploramos numericamente a possibilidade de aplicar o nosso método de medição baseado em FWM em nano-guias de silício. Obtivemos resultados promissores, embora negligenciando efeitos induzidos por portadores livres. Portanto, em nano-guias de silício, estudamos os mecanismos ópticos de geração de portadores e identificamos, pela primeira vez, a contribuição individual da absorção de um e dois fótons nos comprimentos de onda das telecomunicações. Além disso, nossos experimentos de bombeio e prova resolvidos no tempo também revelam uma complexa dinâmica de recombinação dos portadores, que explicamos em termos de recombinação assistida por armadilhas. Esta explicação não foi dada antes no contexto de nano-guias de onda ópticos, e é fundamentada pela boa concordância qualitativa obtida entre um modelo teórico implementado e a dinâmica observada. Nossas observações principais são de importância crucial para vários estudos de fenômenos de propagação linear e não-linear e aplicações em fotônica de silício.

List of Figures

List of Tables

Publications

Journals

1. A. Gil-Molina*, I. Aldaya*, J. L. Pita, L. H. Gabrielli, H. L. Fragnito, and P. Dainese, "Optical free-carrier generation in silicon nano-waveguides at 1550 nm." **Applied Physics Letters**, 112.25, 2018.
2. I. Aldaya*, A. Gil-Molina*, J. L. Pita, L. H. Gabrielli, H. L. Fragnito, and P. Dainese, "Nonlinear carrier dynamics in silicon nano-waveguides." **Optica**, 4.10, pp. 1219–1227, 2017.
3. A. Gil-Molina, A. Perez-Ramirez, J. C. Ramirez, L. H. Gabrielli, and H. L. Fragnito, "Shift of zero-dispersion wavelength in bent optical fibers." **Optics express,** 26.6, pp. 6700–6714, 2018.
4. A. Gil-Molina, J. A Castaneda, D. F. Londono, L. H. Gabrielli, A. M. Cardenas, and H. L. Fragnito, "High-order dispersion mapping of an optical fiber by incoherent pulsed pumped Four- Wave mixing." **To be submitted** (2018).

Conferences

1. A. Gil-Molina, I. Aldaya, J. L. Pita, L. H. Gabrielli, H. L. Fragnito, and P. Dainese, "Characterization of linear and nonlinear carrier generation in silicon nano-waveguides at 1550 nm." In: Conference on Lasers and Electro-Optics (**CLEO**), San Jose, 2018.
2. I. Aldaya, A. Gil-Molina, J. L. Pita, L. H. Gabrielli, H. L. Fragnito, and P. Dainese, "Probing free-carrier recombination in silicon strip nano-waveguides." In: Conference on Lasers and Electro-Optics (**CLEO**), San Jose, 2018.

3. I. Aldaya, A. Gil-Molina, J. L. Pita, H. L. Fragnito, and P. Dainese, "Lifetime dependence on carrier density in silicon nanowires." In: The European Conference on Lasers and Electro-Optics (**CLEO/Europe**), Munich, 2017.
4. I. Aldaya, A. Gil-Molina, H. L. Fragnito, and P. Dainese, "Simple method to simultaneous characterize two-photon absorption coefficient and carrier lifetime in silicon waveguides." In: Latin America Optics and Photonics Conference (**LAOP**), Medellin, 2016.
5. I. Aldaya, A. Gil-Molina, H. L. Fragnito, and P. Dainese, "Time-domain interferometric characterization of nonlinear and thermal-induced phase-shift in silicon waveguides." In: Conference on Lasers and Electro-Optics (**CLEO**), San Jose, 2016.
6. A. Gil-Molina, I. Aldaya, and H. L. Fragnito, "Characterization of fast dispersion fluctuations in optical fibers using incoherently pumped Four-Wave Mixing." In: Latin America Optics and Photonics Conference (**LAOP**), Medellin, 2016.
7. A. Gil-Molina, and H. L. Fragnito, "Dispersion fluctuations in optical fibers" In: International Conference on Optical, Optoelectronic and Photonic Materials and Applications (**ICOOPMA**), Montreal, 2016 (Invited talk).
8. A. Gil-Molina, A. Perez-Ramirez, J. C. Ramirez, and H. L. Fragnito, "Shift of zero-dispersion wavelength and high-order dispersion due to bending in dispersion-shifted fibers." In: Latin America Optics and Photonics Conference (**LAOP**), Cancun, 2014.
9. A. Gil-Molina, A. Perez-Ramirez, and H. L. Fragnito, "Nonlinear fiber-optics with incoherent sources" In: Latin America Optics and Photonics Conference (**LAOP**), Cancun, 2014 (Invited tutorial).
10. J. C. Ramirez, A. Gil-Molina, A. Perez-Ramirez, H. E. Hernandez-Figueroa, and H. L. Fragnito, "Variation of the zero-dispersion wavelength with bending radius in dispersion shifted fibers" In: Latin America Optics and Photonics Conference (**LAOP**), Cancun, 2014.

Table of Contents

1. Introduction

Nonlinear optics studies the interaction of light and matter at high-optical intensities. The beginning of this field has been usually attributed to the first observation of second-harmonic generation (SHG) [1], right after the first laser demonstration [2]. Since then, continuous research efforts on nonlinear optics have allowed the development of several devices that are currently widely-used. For instance, electro-optic modulators based on the Pockels effect [3], Raman amplifiers [4, 5], optical parametric amplifiers (OPAs) [6, 7], and supercontinuum broadband light sources [8, 9]. The development of these devices has been eased by several factors, such as the use of high-power femtosecond pulsed lasers in OPAs, the use of highly-nonlinear materials [10], the long interaction lengths achieved in optical fibers for supercontinuum generation and Raman amplifiers, and novel designs of tight optical-confining waveguides such as photonic-crystal fibers [11, 12] and other high-index contrast waveguides [13, 14].

Although diverse nonlinear-optical phenomena have been explored in the development of different devices, those based on Four-Wave Mixing (FWM) have shown interesting results in optical fibers, such as fiber optical parametric amplifiers (FOPA) [15, 16, 17], optical frequency combs [18, 19], and supercontinuum sources (which can be seeded by FWM) [20, 21, 22]. The advancement of FWM-based devices has been motivated considering two fundamental reasons. First, being a third-order nonlinear process FWM may be explored in many materials. Therefore, besides experiments in optical fibers, FWM-based devices have been also demonstrated in integrated-waveguide structures [23, 24, 25]. Second, the spectral region at which FWM becomes highly efficient depends on the phase-matching condition. Thus, besides exploring materials with different dispersive characteristics, the dispersion of the waveguide can also be engineered in order to tune the FWM-efficiency over a desired spectral region [26, 27].

We have identified different research challenges that have to be overcome in order to facilitate FWM-based waveguide devices to become practical devices. Namely, to be more compact, require less pumping power, and operate over a broadband spectrum.

One of the main limitations of FWM-based waveguide devices (in terms of bandwidth, gain, or conversion efficiency) is the impact of longitudinal fluctuations of the chromatic (or group velocity) dispersion [28]. These fluctuations are mainly attributed to random variations in waveguide geometry that, in the case of optical fibers, result from drawing and preform fabrication processes [28, 29, 30]. An interesting example consists of the achievable parametric gain at the spectral region widely-used for optical communications. Therefore, in Figure 1.1 we show an experimental example of the measured parametric gain of a double-pump FOPA, achieved by using a total optical pumping power of ~0.5 W and 1 km of a highly-nonlinear fiber (HNLF) specially designed to present a robust dispersion against fabrications imperfections [31]. Note that the measured gain bandwidth is quite larger than that achieved by using a commercial c-band Erbium-doped fiber amplifier (EDFA) (i.e., from 1530 to 1565 nm). However, there is an evident difference of ~10 dB between the measured parametric gain and the one predicted by a theoretical approximation in a uniform fiber [17] (showed also in Figure 1.1 for an effective length $L_{eff} = 0.9$ km). Therefore, we believe that this disagreement could be attributed to the effect of longitudinal fluctuations of fiber dispersion, which can be explained by comparing the theoretical approximation assuming a shorter $L_{eff} = 0.7$ km (see the agreement with the measured gain in Figure 1.1).

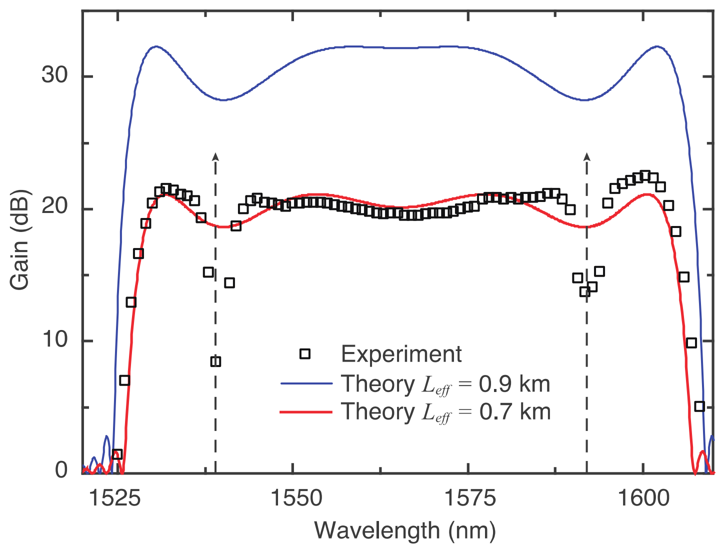

Figure 1.1: Measured and calculated parametric gain of a double-pump FOPA in 1 km of HNLF and using ~500 mW of total pumping power.

Although some studies have tried to evaluate the impact of dispersion fluctuations in the context of FOPAs [28, 32, 30, 33], their results have been limited to theoretical estimations for the length scales and amplitudes of these fluctuations. Therefore, several measuring methods have been proposed to exploit the sensitivity of phase-matched FWM to perform dispersion characterization [34 – 46]. However, most of these methods are limited in providing accurate information of high-order dispersion (HOD), which plays an important role in FWM-based applications and other studies that involve a broadband optical spectrum [26, 47 – 54]. In this thesis we have significantly improved the method originally proposed in [36], that is based on FWM between an incoherent pump and a laser, in order to experimentally study the characteristics of dispersion fluctuations in optical fibers, not only for the zero-dispersion wavelength but also for HOD. In addition, our experimental results along with our numerical calculations of fiber dispersion allowed us to provide a better understanding of the origin of changes of fiber dispersion such as bending and changes of fiber geometry. We also show the possibilities of applying our improved method for dispersion characterization in integrated-waveguide structures. The presented studies are of fundamental importance in the development of FWM-based fiber optical devices and could provide insights for dispersion engineering of integrated-waveguides.

Another main limitation in the development of FWM-based fiber devices is the weak nonlinearity of silica fibers, which has implied the use of high pumping-power levels and long lengths of fiber. Therefore, silicon nano-waveguides have become a promising platform for nonlinear optical devices, which has been evidenced by several experimental demonstrations [23, 55 – 58]. These demonstrations have been achieved with short waveguide lengths and using low pumping-power levels, given the large nonlinear coefficient of silicon nano-waveguides (which is about 5 orders of magnitude larger than that of standard optical fibers). However, at the 1550 nm spectral band, widely-used for optical communications, silicon presents a large two-photon absorption (TPA) coefficient that could lead to a significant generation of free carriers. Consequently, the generated free carriers modify the propagation characteristics of the silicon nano-waveguides via free-carrier absorption (FCA) and free-carrier dispersion (FCD). Although different approaches have been adopted to minimize FCA and/or FCD [55, 23, 56], some studies have shown that a better understanding of free-carrier effects and their dynamics (governed by generation and recombination mechanisms) can be exploited for studies of novel nonlinear optical phenomena [59 – 66] and the development of all-optical devices for control of light [67, 68]. In this thesis we have thoroughly characterized the optical generation mechanisms of free-carriers and their recombination dynamics in silicon nano-waveguides, by means of time-resolved pump-and-probe experiments. Our experimental results and theoretical developments allowed us to accurately characterize the contribution of single-photon and two-photon absorption in carrier generation. In addition, we have been able to clearly observe the evolution of the instantaneous carrier-lifetime, revealing a complex recombination dynamics that we have explained in terms of trap-assisted recombination. This explanation, to the best of our knowledge, has not been explored in silicon photonics or other semiconductor photonic platforms. The presented results provide a better understanding of the dynamics of free-carriers in silicon nano-waveguides, which is of crucial importance for studies of nonlinear optical phenomena and opens opportunities for the development of novel silicon-photonic devices.

1.1 Thesis Organization

In chapter 2 we describe the main characteristics of the improved dispersion characterization method based on FWM between an incoherent pump and a laser. We present the basic experimental configuration of the method, the spectral characteristics of the generated FWM power spectrum, a detailed description of the phase-matching condition and its relationship with the waveguide dispersion parameters, and some examples that show the capabilities for dispersion characterization of the method. In addition, we present the application of the method in three different studies of dispersion characterization: (i) high-order dispersion mapping of a long optical fiber, (ii) the shift of the zero-dispersion wavelength with bending in a short optical fiber, and (ii) the possibilities and limitation of characterizing high-order dispersion in silicon nano-waveguides by ignoring two-photon absorption and free-carrier induced effects (these will be thoroughly explored in chapter 3).

In chapter 3 we present a detailed experimental and theoretical description of the linear and nonlinear optical generation mechanisms of free-carriers and their recombination dynamics in silicon nano-waveguides at 1550 nm. In the first part, we describe the theoretical modeling of optical pulse propagation considering single and two-photon absorption, and the free-carrier dynamics. Consequently, we describe the implemented pump-and-probe experimental setup and the theoretical developments used to measure the waveguide single and two-photon absorption coefficients. Then, we present our main results of carrier generation. In the second part, we describe the theoretical model of carrier recombination via flaw states and carrier-trapping that is used to explain the observed recombination dynamics in silicon nano-waveguides. A comparison between the experimental and theoretical results is then presented. Finally, we show how the described dynamics could be exploited in all-optical switching applications.

In chapter 4 we summarize the main conclusions of the thesis including our main contributions and possible works that could be developed in the future, based on our main observations.

In addition, given that most studies presented in this thesis involve nonlinear propagation of optical pulses, in the following appendix we present a summary of the theory that is usually adopted for waveguides.

1.2 Appendix: Nonlinear Optical Pulse Propagation in Waveguides

In this section we will summarize the theoretical background that is essential to describe the propagation of optical pulses along an optical waveguide considering linear and nonlinear material responses.

By assuming that optical waveguides are made of a non-magnetic medium with no free-charges, a general form of the time-domain wave equation for the electric field ($\boldsymbol{E}$) can be derived from Maxwell's equations and is given by [69, 50, 70]:

$$\nabla \times \nabla \times \boldsymbol{E}(\boldsymbol{r},t) + \frac{1}{c^2}\frac{\partial^2 \boldsymbol{E}(\boldsymbol{r},t)}{\partial t^2} = -\mu_0 \frac{\partial^2 \boldsymbol{P}(\boldsymbol{r},t)}{\partial t^2}, \tag{1.1}$$

where $\boldsymbol{r}$ is the spatial-coordinate vector, the vacuum speed of light $c = 1/\sqrt{\mu_0 \varepsilon_0}$, with μ_0 and ε_0 being the vacuum electric permittivity and magnetic permeability, respectively. Note that in Equation (1.1) the electric polarization $\boldsymbol{P}$ acts as a source term and represents the medium response to the applied electric field. Therefore, considering how $\boldsymbol{P}$ depends on the strength of the applied field $\boldsymbol{E}$, it is appropriate to separate the induced polarization in two parts as:

$$\boldsymbol{P}(\boldsymbol{r}, t) = \boldsymbol{P_L}(\boldsymbol{r}, t) + \boldsymbol{P_{NL}}(\boldsymbol{r}, t), \tag{1.2}$$

where $\boldsymbol{P_L}$ depends linearly on $\boldsymbol{E}$ and $\boldsymbol{P_{NL}}$has a nonlinear dependence. The linear polarization $\boldsymbol{P_L}$ is related with $\boldsymbol{E}$ by**:**

$$\boldsymbol{P_L}(\boldsymbol{r}, t) = \varepsilon_0 \int_{-\infty}^{\infty} d\tau' R^{(1)}(\tau') \cdot \boldsymbol{E}(\boldsymbol{r}, t - \tau'), \tag{1.3}$$

where $R^{(1)}(\tau')$ is the linear polarization response function of the medium, which is a second-rank tensor and obeys the principle of time-invariance, and the causality and reality conditions [70]. In addition, Equation (1.3) assumes that the medium response is local according to the electric-dipole approximation. However, it is usually more convenient to describe the optical medium properties in the frequency domain, therefore, we define the Fourier and inverse-Fourier transform pair as:

$$\begin{aligned} f(\omega) &= \int_{-\infty}^{\infty} f(t) e^{i\omega t} dt, \\ f(t) &= \int_{-\infty}^{\infty} f(\omega) e^{-i\omega t} \frac{d\omega}{2\pi}. \end{aligned} \tag{1.4}$$

By using the inverse-Fourier transform in Equation (1.3), it is possible to express $\boldsymbol{P_L}$ in the frequency domain as [69]:

$$\begin{aligned} \widetilde{\boldsymbol{P}}_{\boldsymbol{L}}(\boldsymbol{r}, \omega) &= \varepsilon_0 \chi^{(1)}(\omega) \widetilde{\boldsymbol{E}}(\boldsymbol{r}, \omega), \\ \chi^{(1)}(\omega) &= \int_{-\infty}^{\infty} R(\tau') e^{i\omega\tau'} d\tau', \end{aligned} \tag{1.5}$$

where $\chi^{(1)}(\omega)$ is known as the linear susceptibility of the medium. In Equation (1.5) we have assumed that the medium is isotropic and, thus, the 9 elements $\chi_{i,j}^{(1)}(\omega)$ (for $i,j=x,y,z$) of the second-rank tensor $\chi^{(1)}(\omega)$ become an scalar. By means of the Fourier transform and using Equation (1.5) for $\widetilde{\boldsymbol{P}}_{\boldsymbol{L}}$, the wave equation may be also given in the frequency domain as:

$$\nabla\times\nabla\times\widetilde{\boldsymbol{E}}(\boldsymbol{r},\omega)=k_0^2\varepsilon(\omega)\widetilde{\boldsymbol{E}}(\boldsymbol{r},\omega)+\omega^2\mu_0\widetilde{\boldsymbol{P}}_{\boldsymbol{NL}}(\boldsymbol{r},\omega), \tag{1.6}$$

where $k_0=\omega/c$ and $\varepsilon(\omega)=1+\chi^{(1)}(\omega)$ is the complex dielectric constant of the medium. The real and imaginary parts of $\varepsilon(\omega)$ can be related, respectively, with the medium refractive index $n(\omega)$ and absorption coefficient $\alpha(\omega)$ by means of the following relations:

$$\begin{gathered}\varepsilon(\omega)=\left(n+i\frac{\alpha c}{2\omega}\right)^2,\\ n(\omega)=1+\frac{1}{2}Re\left[\chi^{(1)}(\omega)\right],\\ \alpha(\omega)=\frac{\omega}{nc}Im\left[\chi^{(1)}(\omega)\right].\end{gathered}\tag{1.7}$$

In addition, by using the identity $\nabla\times\nabla\times\widetilde{\boldsymbol{E}}=\nabla\left(\nabla\cdot\widetilde{\boldsymbol{E}}\right)-\nabla^2\widetilde{\boldsymbol{E}}$ and considering that $\nabla\cdot\widetilde{\boldsymbol{E}}=0$ (in the absence of free-charges from Maxwell's equations), Equation (1.6) becomes:

$$\nabla^2\widetilde{\boldsymbol{E}}+k_0^2\varepsilon(\omega)\widetilde{\boldsymbol{E}}=-\omega^2\mu_0\widetilde{\boldsymbol{P}}_{\boldsymbol{NL}}. \tag{1.8}$$

Regarding the nonlinear polarization, we can assume that $\widetilde{\boldsymbol{P}}_{\boldsymbol{NL}}$ is governed by third-order nonlinearities considering that silicon oxide and silicon (the materials used in this thesis) are centro-symmetric materials and then lack of second-order nonlinearities. Moreover, in order to solve Equation (1.8), further simplifications must be made:

(i) We will assume that the applied field is linearly polarized in the x direction (scalar approximation). Although this assumption is valid for polarization-maintaining fibers and other waveguides with large birefringence (e.g., silicon nano-waveguides), it is commonly adopted for nonlinear propagation studies in standard optical fibers [50].

(ii) We assume that the applied field is quasi-monochromatic, which is valid considering that the spectral width of the applied field $\Delta\omega$ is much smaller than

the optical carrier frequency ω_0 (the optical pulse widths used in this thesis are $>$ 80 ps).

(iii) We adopt the slowly varying envelope approximation (SVEA) and write the electric field and the linear and nonlinear parts of the induced polarization as:

$$\boldsymbol{E}(\boldsymbol{r},t) = \frac{1}{2}\hat{x}\left[E(\boldsymbol{r},t)e^{(-i\omega_0 t)} + c.c.\right],$$
$$\boldsymbol{P_L}(\boldsymbol{r},t) = \frac{1}{2}\hat{x}\left[P_L(\boldsymbol{r},t)e^{(-i\omega_0 t)} + c.c.\right], \tag{1.9}$$
$$\boldsymbol{P_{NL}}(\boldsymbol{r},t) = \frac{1}{2}\hat{x}\left[P_{NL}(\boldsymbol{r},t)e^{(-i\omega_0 t)} + c.c.\right].$$

This allows to separate the rapidly and slowly varying parts of $\boldsymbol{E}(\boldsymbol{r},t)$, $\boldsymbol{P_L}(\boldsymbol{r},t)$ and $\boldsymbol{P_{NL}}(\boldsymbol{r},t)$. By means of the previous approximations and the Fourier transform, it is possible to obtain a simple expression for the nonlinear part of the induced polarization (considering only the electronic contribution) in the frequency-domain given by:

$$\tilde{P}_{NL} = \varepsilon_0\varepsilon_{NL} = \varepsilon_0\frac{3}{4}\chi^{(3)}_{xxxx}\left|\tilde{E}\right|^2\tilde{E}, \tag{1.10}$$

where the factor $\frac{3}{4}$ is due to the fact that both the incident field and induced nonlinear polarization oscillate at the same frequency (ω_0). Rigorously, there should be also a third-harmonic term ($3\omega_0$) in Equation (1.10), although it is usually neglected since its phase-matching condition is hard to satisfy. The nonlinear contribution to the dielectric constant ε_{NL} is therefore related with intensity-dependent refractive index $\tilde{n}$ and absorption coefficient $\tilde{\alpha}$ defined as:

$$\tilde{n} = n + \bar{n}_2|E|^2, \quad \tilde{\alpha} = \alpha + \alpha_2|E|^2,$$
$$\bar{n}_2 = \frac{3}{8n}Re\left[\chi^{(3)}_{xxxx}\right], \tag{1.11}$$
$$\alpha_2 = \frac{3}{4}\frac{\omega}{cn}Im\left[\chi^{(3)}_{xxxx}\right],$$

where $\bar{n}_2$ and α_2 are the nonlinear refractive index and the two-photon absorption coefficient respectively. However, from an experimental perspective it is more convenient to relate these parameters with the optical intensity $I = \frac{1}{2}\varepsilon_0 cn|E|^2$, therefore Equation (1.11) may be also written as:

$$\tilde{n} = n + n_2 I, \quad \tilde{\alpha} = \alpha + \beta_{TPA} I,$$
$$n_2 = \frac{3}{4\varepsilon_0 cn^2} Re\left[\chi^{(3)}_{xxxx}\right], \tag{1.12}$$
$$\beta_{TPA} = \frac{3}{2}\frac{\omega}{\varepsilon_0 c^2 n^2} Im\left[\chi^{(3)}_{xxxx}\right],$$

where the nonlinear refractive index n_2 has units of m^2 W^{-1} and the two-photon absorption coefficient β_{TPA} has units of m W^{-1} (usually given as cm/GW).

By means of the SVEA in Equation (1.9), the wave equation can now be given for the Fourier transform of $E(\boldsymbol{r}, t)$ as:

$$\nabla^2 \tilde{E}(\boldsymbol{r}, \omega - \omega_0) + k_0^2 \varepsilon(\omega) \tilde{E}(\boldsymbol{r}, \omega - \omega_0) = 0, \tag{1.13}$$

where the dielectric constant has now been redefined as $\varepsilon(\omega) = 1 + \chi^{(1)}(\omega) + \varepsilon_{NL}$. Note that Equation (1.13) is in the form of the Helmholtz equation, which can be solved by means of the method of separation of variables. Therefore, assuming that the light propagates along the waveguide in the z direction and the waveguide cross-section in the xy plane, a solution of Equation (1.13) can be given by:

$$\tilde{E}(\boldsymbol{r}, \omega - \omega_0) = F(x, y)\tilde{A}(z, \omega - \omega_0) e^{(i\beta_0 z)}, \tag{1.14}$$

where $F(x, y)$ is modal distribution, which in the case of single-mode waveguides (as the ones used in this thesis) corresponds to the fundamental mode. The function $\tilde{A}(z, \omega - \omega_0)$ is the Fourier transform of the slowly varying envelope and β_0 is the propagation constant evaluated at the carrier frequency, i.e., $\beta_0 = \beta(\omega_0)$. Both Equations (1.13) and (1.14) lead to the following equations for $F(x, y)$ and $\tilde{A}(z, \omega)$:

$$\frac{\partial^2 F}{\partial x^2} + \frac{\partial^2 F}{\partial y^2} + \left[k_0^2 \varepsilon(\omega) - \tilde{\beta}^2\right] F = 0, \tag{1.15}$$

$$2i\beta_0 \frac{\partial \tilde{A}}{\partial z} + \left(\tilde{\beta}^2 - \beta_0^2\right)\tilde{A} = 0. \tag{1.16}$$

The second derivative $\partial^2 \tilde{A}/\partial z^2$ in Equation (1.16) has been neglected given that $\tilde{A}(z,\omega)$ is a slowly varying function of z. Note that the propagation constant $\tilde{\beta}$ can obtained by solving the eigenvalue Equation (1.15), although it becomes a complicated problem since the effect of linear losses and nonlinearity are taken into account in $\varepsilon(\omega)$. Therefore, Equation (1.15) can be solved by using first-order perturbation theory [50]. In this approach, the effect of linear losses and nonlinearity are neglected by assuming $\varepsilon(\omega) \approx n^2(\omega)$ and, therefore, the modal distribution $F(x,y)$ and the corresponding propagation constant β are obtained, assuming that the effect of nonlinearity does not modify the modal distribution $F(x,y)$. On the other hand, according to the first order perturbation theory the eigenvalue $\tilde{\beta}$ becomes:

$$\tilde{\beta}(\omega) = \beta(\omega) + \Delta\beta(\omega), \tag{1.17}$$

with:

$$\Delta\beta(\omega) = k_0 \frac{\iint_{-\infty}^{\infty} \Delta n |F(x,y)|^2 dxdy}{\iint_{-\infty}^{\infty} |F(x,y)|^2 dxdy}, \tag{1.18}$$

where Δn is a small perturbation to the refractive index that accounts for linear losses and nonlinearity, and is given by:

$$\Delta n = \bar{n}_2 |E|^2 + i\frac{\tilde{\alpha}}{2k_0}. \tag{1.19}$$

By using Equations (1.17), (1.18) and (1.19) in Equation (1.16), and following the considerations that are detailed in [50], it is possible to obtain an expression to describe the evolution of the envelope of an optical pulse $A(z,t)$ along the waveguide, which is given by:

$$\frac{\partial A}{\partial z} = \left[i \sum_{n=2} \frac{\beta_n}{n!} \left(i \frac{\partial A}{\partial t} \right)^n - \frac{\alpha}{2} + i\gamma |A|^2 \right] A, \tag{1.20}$$

where the parameters $\beta_n = d^n\beta/d\omega^n|_{\omega=\omega_0}$ correspond to a Taylor expansion of $\beta(\omega)$ around the carrier frequency ω_0. Considering that the pulse envelope moves at the group velocity $v_g = 1/\beta_1$, it is convenient to start the summation in Equation (1.20) from $n = 2$ in order to define a frame of reference moving with the pulse. In addition, the envelope $A(z,t)$ in Equation (1.20) has been normalized such that $|A|^2$ represents optical power and the nonlinear coefficient γ is given by:

$$\gamma = \frac{\omega_0 n_2}{c A_{eff}}, \tag{1.21}$$

where the effective area A_{eff} is given by:

$$A_{eff} = \frac{\left(\iint_{-\infty}^{\infty} |F(x,y)|^2 dxdy\right)^2}{\iint_{-\infty}^{\infty} |F(x,y)|^4 dxdy}. \tag{1.22}$$

The expressions given in Equations (1.20), (1.21) and (1.22) are commonly used for propagation studies of optical pulses in optical fibers as take into account the effect of linear losses, Kerr nonlinearity and dispersion. However, in the case of tight optical-confining waveguide structures (as the silicon-nano waveguides used this thesis), recent theoretical approaches have been proposed in order to consider the enhancement of nonlinearities due to the increased longitudinal component of the electric field [71, 72]. In particular we have found a good agreement with our experiments in silicon nano-waveguides by using the definition of the effective area that is given in terms of the z-component of the mode Poynting vector S_z, given by [71, 72]:

$$A_{eff} = \frac{\left(\iint_{-\infty}^{\infty} S_z^2 dxdy\right)^2}{\iint_{-\infty}^{\infty} S_z^2 dxdy}. \tag{1.23}$$

2. Dispersion Characterization by Using Four-Wave Mixing Pumped by an Incoherent Source

It is well-known that dispersive properties of waveguides are of fundamental importance in propagation studies of linear and nonlinear optical phenomena. For example, engineering the dispersion of optical waveguides is crucial for several nonlinear optical applications [26, 27, 73 – 79], especially for parametric devices such as amplifiers, wavelength converters and frequency combs generators. This is because parametric devices are based on phase-matched Four-Wave Mixing (FWM). Different studies have demonstrated that the efficiency of FWM is significantly reduced as a result of longitudinal dispersion fluctuations in optical fibers [28, 32, 30, 33]. Although most of these studies have solely taken into account changes of the zero-dispersion wavelength (λ_0), it is well-known that high-order dispersion (HOD) plays also an important role in the efficiency of parametric devices [26, 80 – 91]. In addition, HOD is also important for studies that involve a broadband optical spectrum such as of soliton physics and supercontinuum generation [26, 47 – 51], and ultra-high-capacity communications [52, 53, 54]. Therefore, the possibility of obtaining accurate information of dispersion parameters in optical waveguides (i.e., λ_0 and HOD) becomes relevant in the development of linear and nonlinear optical applications.

Widely used dispersion measurement techniques, usually implemented in commercial instruments, are based on interferometric or time-of-flight measuring methods [92, 93]. These methods perform measurements of the group velocity (i.e., $v_g = 1/\beta_1$) for different frequencies and then obtain the second and third-order dispersion (i.e., β_2 and β_3) by polynomial fitting or numerical differentiation. However, for higher-order in the dispersion parameters (i.e., β_4, β_5,…), these methods are usually limited in accuracy, often not being able to correctly determine the sign of β_4 [36].

In contrast, given the high-sensitivity of phase-matched FWM to minute changes of dispersion, different FWM-based characterization methods have demonstrated capabilities for measuring HOD [35, 36, 94]. Among these, we have explored the method that was first proposed in [36] and subsequently improved in [94], which is based on measuring the spectrum generated by FWM between an incoherent pump and a laser. The use of an incoherent source as a pump offers some advantages: (i) a single measurement allows to visually evaluate the uniformity of a waveguide. (ii) Considering that the incoherent source is unpolarized there is, in principle, no need of polarization alignment. (iii) Given the large bandwidth of the incoherent source, Stimulated Brillouin Scattering (SBS) is prevented.

In this chapter we present the improvements we have done to the method based on FWM pumped by an incoherent source and the application of the improved method in dispersion characterization of waveguides. These improvements consist of a deeper interpretation of the phase-matching condition and several modifications of the experimental setup to explore different capabilities of the method, such as dispersion-mapping and obtaining accurate dispersion characterization in fibers of few meters of length.

In the first part of this chapter (Section 2.1) we describe our measuring method. We explain the underlying FWM process and the main characteristics of the generated power spectrum. Then, we present the phase-matching condition of the FWM process, which is used to obtain the measured dispersion coefficients. Finally, by using different measurement examples in optical fibers we discuss the capabilities and limits of our measuring method.

In the second part of this chapter (Section 2.2) we present an example of measuring the longitudinal evolution of dispersion parameters in an optical fiber of few km of length. The so-called dispersion maps are obtained by changing the overlapping region along the fiber between two short optical pulses (i.e., the incoherent pump and the laser). We first describe the experimental setup used in the dispersion-mapping experiments. Subsequently, we present the main experimental results along with numerical simulations of the pulse propagation that present a good agreement. In addition, we present the results of the numerical calculation of fiber dispersion that are used to understand the contribution of changes in fiber geometry in the measured fluctuations of dispersion parameters along the fiber.

In the third part of this chapter (Section 2.3) we present another interesting example, in which we were able to measure a segment of fiber as short as 20 m and evaluate the shift of fiber dispersion with bending. We first present the used experimental setup, describing the main improvements performed to increase the power of the incoherent-pump and laser, and the signal to noise ratio of the generated FWM spectrum. These improvements allowed us to measure such a short length of fiber, to guarantee the uniformity of the tested fiber and to obtain a good sensitivity in the measured λ_0 (i.e., $\sim$40 pm). Finally, we present the results of the measured shift of dispersion with bending along with numerical calculations of a fiber profile that present a good agreement. Our numerical calculations also allowed us to explain the relationship between changes of fiber dispersion induced by bending and those induced by the modification of fiber geometry.

Finally, in the fourth part of this chapter (Section 2.4) we evaluate the application of our method in silicon nano-waveguides by means of theoretical calculations of the FWM generated spectrum and neglecting two-photon absorption and the free-carrier induced effects (these will be comprehensively treated in chapter 3). We first describe both material and waveguide dispersion in this kind of waveguides. Subsequently, we show numerical calculations of HOD parameters in these waveguides by using the finite element method (FEM) and numerical differentiation. Finally, we show the prospects of using our measuring method in nano-waveguides, in terms of the ease of implementation and limits of our method.

2.1 Measuring Method

Our measuring method is experimentally simple and can be implemented, in principle, with few instruments. The basic description of the measuring setup is illustrated in Figure 2.1. An incoherent-pump is coupled with a relatively weak tunable laser into the fiber under test (FUT) by means of a fiber coupler. The incoherent pump must be centered at a frequency ω_c, which is close to the zero-dispersion frequency $\omega_0 = 2\pi c/\lambda_0$, whereas the laser is tuned at a frequency ω_ℓ, which is far from ω_c. A power spectrum is generated in the FUT by means of

FWM between the incoherent pump and the laser. The generated FWM spectrum is then detected by using an optical spectrum analyzer (OSA). The shape of the generated FWM power spectrum exhibits a peak at $\omega_{FWM} = 2\omega_c - \omega_\ell$ and satisfies the following phase-matching condition:

$$\Delta\beta(\omega) = \beta(\omega) + \beta(\omega_\ell) - 2\beta(\omega_c) = 0 \text{ at } \omega = \omega_{FWM}. \qquad (2.1)$$

In Figure 2.1(a) we illustrate a sample of the FWM power spectrum generated along a uniform fiber. It is worth noting that the generated spectrum exhibits a well-defined single peak, which implies that the phase-matching condition is maintained along the fiber as a consequence of the fiber uniformity. However, most optical fibers present random non-uniformities as a result of their fabrication processes that lead to longitudinal dispersion fluctuations [29, 95, 28]. Therefore, when measuring a non-uniform fiber, one would expect a FWM power spectrum with several peaks [see Figure 2.1(b)], where each peak corresponds to fiber segments with different of dispersion parameters [36].

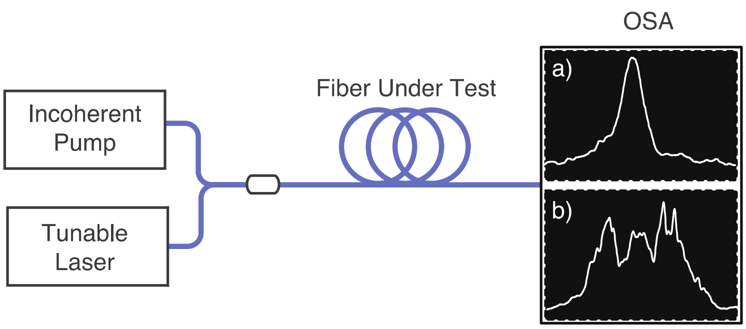

Figure 2.1: Basic setup and samples of the measured spectra for an (a) uniform fiber and a (b) non-uniform fiber.

Given the sensitivity of phase-matched FWM to changes of fiber dispersion (in general, changes of dispersion in an optical waveguide), it is possible to retrieve information about the dispersion from the measured FWM power spectrum. In the following subsections we will discuss how the shape of the generated power spectrum and the phase-matching condition of the FWM process influence the capabilities of our method to characterize the dispersive properties of an optical waveguide.

2.1.1 Power spectrum generated by Four-Wave Mixing between and incoherent pump and a weak laser

In this section we summarize the main steps involved in the derivation of the power spectrum generated by FWM between an incoherent pump and a laser, however, more details can be found in [36, 96].

A schematic of the spectral distribution of the incoherent pump, laser, and generated FWM power spectrum is illustrated in Figure 2.2. The temporally-incoherent pump (ideally flat-top) with spectral width $\Delta\omega_p$ is centered near ω_0. The laser, on the other hand, is located far from ω_0 at ω_ℓ. In addition, the incoherent-pump should be narrower than the frequency separation between pump and laser (i.e., $\Delta\omega_p \ll |\omega_p - \omega_\ell|$). The interaction between the incoherent pump and the laser in the optical waveguide, generates a new wave through FWM at $\omega = \omega_1 + \omega_2 - \omega_\ell$, where ω_1 and ω_2 are two Fourier components of the incoherent-pump. Furthermore, by centering the incoherent-pump at ω_c, more Fourier component pairs (ω_1, ω_2) that are symmetrically distributed around ω_c satisfy the phase-matching condition of Equation (2.1) and, therefore, the power of the FWM power spectrum peak (located at ω_{FWM}) is maximized.

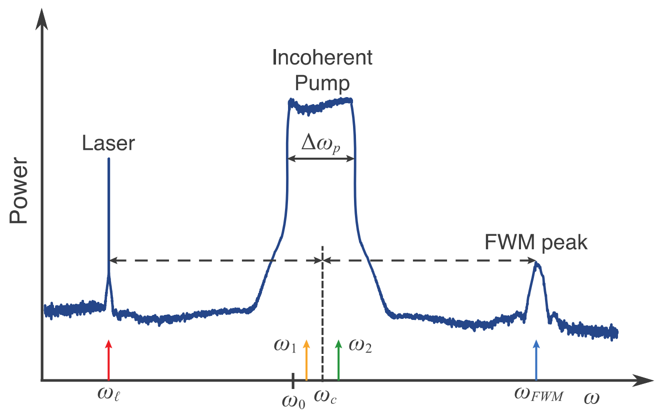

Figure 2.2: Spectral schematic of the FWM process.

In order to derive an expression for the power spectral density of the field generated by FWM, we may start from the nonlinear polarization that takes into account only the FWM process $\omega = \omega_1 + \omega_2 - \omega_\ell$, which can be given by [36, 96]:

$$\tilde{P}_{NL}(\omega) = 2\frac{3\varepsilon_0 2\pi \tilde{E}_\ell^*}{4(2\pi)^2}\chi_{xxxxx}^{(3)}\int_0^\infty d\omega_1 \tilde{E}_p(\omega_1)\tilde{E}_p(\omega + \omega_\ell - \omega_1). \tag{2.2}$$

This expression has been obtained taking to account different considerations: *i*) The laser and incoherent pump fields are given (in the frequency-domain) as $2\pi\tilde{E}_\ell\delta(\omega-\omega_\ell)$ and $\tilde{E}_p(\omega)$, respectively. *ii*) Both the laser and the incoherent pump have relatively low power, so effects of self-phase and cross-phase modulation are neglected. *iii*) Due to the symmetry of the FWM process, ω_2 is expressed in terms of ω_1 as $\omega_2 = \omega + \omega_\ell - \omega_1$. *iv*) Here, the scalar and SVEA approximations and the definition of the Fourier transform pair (presented in Appendix 1.2) are also assumed.

The expression that describes the propagation of the field generated by FWM along the propagation in a loss-less optical waveguide in the z direction, can be given by [36, 96]:

$$\frac{\partial \tilde{E}_{FWM}(z,\omega)}{\partial z} = -\frac{i\omega c\mu_0}{2n}\tilde{P}_{NL}(\omega)e^{-i\beta(\omega)z}, \tag{2.3}$$

where we have considered that (for $z > 0$) the FWM, pump and laser fields are given as $\tilde{E}_{FWM}(z,\omega) = \tilde{A}_{FWM}(\omega)e^{i\beta(\omega)z}$, $\tilde{E}_p(z,\omega) = \tilde{A}_p(\omega)e^{i\beta(\omega)z}$ and $\tilde{E}_\ell(z) = \tilde{A}_\ell e^{i\beta(\omega_\ell)z}$. By integrating Equation (2.3), considering that at the input of the waveguide $\tilde{E}_{FWM}(0,\omega) = 0$, assuming that the dispersion is uniform along the waveguide (i.e., β does not change with z), and using Equation (2.2), it is possible to obtain an expression for the FWM field at the output of the waveguide of length L, which is given by [36, 96]:

$$\begin{aligned}\tilde{E}_{FWM}(L,\omega) = -\frac{i\omega}{2nc}\frac{3L\tilde{E}_\ell^*}{4}\chi_{xxxx}^{(3)}\int_0^\infty & d\omega_1 \tilde{E}_p(\omega_1) \\ \times \tilde{E}_p(\omega + \omega_\ell - \omega_1) & e^{\frac{i\Delta\beta L}{2}}\operatorname{sinc}\left(\frac{\Delta\beta L}{2}\right),\end{aligned} \tag{2.4}$$

where $\Delta\beta(\omega) = \beta(\omega) + \beta(\omega_\ell) - \beta(\omega_1) - \beta(\omega + \omega_\ell - \omega_1)$ and $\operatorname{sinc}(x)$ is defined as $\sin(x)/x$.

Given that the FWM field is generated by an incoherent source, it could be also considered as incoherent [97]. Therefore, in order to derive an expression for the FWM power spectral density, the stochastic properties of an incoherent source must be taken into account in the calculation of the ensemble average $\langle|\tilde{E}_{FWM}(\omega)|^2\rangle$. That is, properties of wide-sense stationary and circular Gaussian random processes in the time domain. Thus, it is possible to obtain an expression of the FWM power spectral density by using Equation (2.4), which is given by [36, 96]:

$$\begin{aligned} S_{FWM}(\omega) = 2\gamma^2 L^2 P_\ell^2 \int_0^\infty d\omega_1 S_p(\omega_1) \\ \times S_p(\omega + \omega_\ell - \omega_1)\mathrm{sinc}^2\left(\frac{\Delta\beta L}{2}\right), \end{aligned} \tag{2.5}$$

where γ is the nonlinear coefficient given by Equation (1.21), S_p is the power spectral density of the incoherent-pump and P_ℓ is the laser power. In addition, Equation (2.5) can be further simplified if we assume that the incoherent-pump is flat-top with constant power spectral density over $\Delta\omega_p$ and that the spectral width of the incoherent-pump is narrow such that the wavevector mismatch can be approximated as $\Delta\beta = \beta(\omega) + \beta(\omega_\ell) - 2\beta(\omega_c)$. Thus, by considering the mentioned assumptions, the spectral density of the field generated by FWM may be also given as [36, 96]:

$$S(\omega) \cong 2\gamma^2 S_p^2 \Delta\omega_p L^2 P_\ell \mathrm{sinc}^2\left[\frac{\Delta\beta(\omega)L}{2}\right]. \tag{2.6}$$

In Figure 2.3 we illustrate the power spectral density of the generated FWM normalized to its maximum value [i.e., $S(\omega)/S(\omega_{FWM})$ calculated by means of Equation (2.5)]. Note that the FWM spectrum is not symmetric around its peak, which is a consequence of the asymmetry of the wavevector mismatch $(\Delta\beta)$ with $\Omega = \omega - \omega_{\mathrm{FWM}}$ (i.e. caused by dispersion). This asymmetry is clearly evidenced by the frequency separation between the minima of the generated FWM spectrum from each side of the FWM peak, that according of the $\mathrm{sinc}(x)$ should appear at $x = \Delta\beta(\Omega)L/2 = n\pi$ as illustrated in the inset of Figure 2.3.

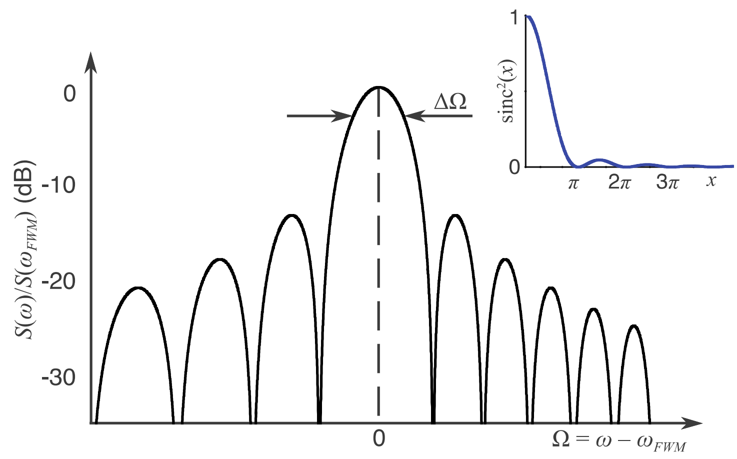

Figure 2.3: Calculated normalized FWM power spectral density (Inset: sinc^2 function in linear scale).

By identifying the main characteristics of the generated FWM power spectrum, that is, its peak frequency (ω_{FWM}) and the frequencies at which presents different minima [i.e., $\Delta\beta(\Omega)L/2 = n\pi$], one could anticipate that it is possible to retrieve information about the dispersion parameters of the waveguide. This is achieved by means of a detailed analysis upon the phase matching condition of the FWM process, as will be presented in the next subsection.

2.1.2 Phase-matching condition of the FWM process

Considering the waves involved in the FWM process, that is, the generated FWM, the laser, and two Fourier components within the incoherent pump, the phase-matching condition is given by:

$$\Delta\beta = \beta(\omega_{FWM}) + \beta(\omega_\ell) - \beta(\omega_1) - \beta(\omega_2) = 0. \tag{2.7}$$

Making a Taylor expansion up to the fourth-order around ω_c in Equation (2.7) it is easy to see that $\Delta\beta_n = 0$ for $n = 1, 3$ considering that $\omega_{FWM} - \omega_c = \omega_c - \omega_\ell$ and $\omega_2 - \omega_c = \omega_c - \omega_1$) we get:

$$\begin{aligned} \Delta\beta = &\frac{1}{2!}\beta_{2c}[2(\omega_c - \omega_\ell)^2 - 2(\omega_c - \omega_1)^2] \\ &+ \frac{1}{4!}\beta_{4c}[2(\omega_c - \omega_\ell)^4 - 2(\omega_c - \omega_1)^4] = 0, \end{aligned} \tag{2.8}$$

where the dispersion parameters $\beta_{nc} = d^n\beta/d\omega^n$ are evaluated at $\omega_c = (\omega_{FWM} + \omega_\ell)/2$. Moreover, recalling that the bandwidth of the incoherent-pump is narrower than the separation between pump and laser (i.e., $|\omega_c - \omega_\ell| \gg |\omega_1 - \omega_c|$), Equation (2.8) may be simplified as:

$$\frac{\beta_{4c}}{12}(\omega_c - \omega_\ell)^2 = -\beta_{2c}. \tag{2.9}$$

However, it is more convenient to express Equation (2.9) in terms of the commonly used β_n dispersion parameters evaluated at ω_0, that is $\beta_{2c} = \beta_3(\omega_c - \omega_0) + (\beta_4/2)(\omega_c - \omega_0)^2$ and $\beta_{4c} = \beta_4$. Therefore, it is possible to recast Equation (2.9) as:

$$7\omega_{c0}^2 + (12\Omega_{34} - 2\omega_{\ell 0})\omega_{c0} + \omega_{\ell 0}^2 = 0, \tag{2.10}$$

where $\omega_{c0} = \omega_c - \omega_0$, $\omega_{\ell 0} = \omega_\ell - \omega_0$ and $\Omega_{34} = \beta_3/\beta_4$. Notice that Equation (2.10) is a quadratic equation on ω_{c0} and, therefore, it can be easily solved in order to obtain an expression for ω_{FWM} as a function of ω_ℓ of the form:

$$\omega_{FWM} = f(\omega_\ell, \omega_0, \Omega_{34}). \tag{2.11}$$

Thus, by measuring ω_{FWM} for different ω_ℓ and fitting the measured values with Equation (2.11), the values of ω_0 and Ω_{34} can be obtained as fitting parameters. An example of this measurement will be presented in the following subsection.

Another interesting aspect of the generated FWM spectrum is the minima around the peak that are predicted by theory in a uniform fiber (see Figure 2.3 and its inset). These minima had not been clearly observed in previous experiments due to fiber non-uniformity and limited signal-to-noise ratio (SNR) of [36, 98], however, we have been able to observe these spectral minima in a short uniform dispersion-shifted fiber (DSF) in our recent work [94] (specific details of this study will be presented in Section 2.3). Therefore, it is also useful to obtain an expression for $\Delta\beta$ around the FWM peak in terms of $\Omega = \omega - \omega_{FWM}$ and fiber dispersion parameters.

If we fix one of the incoherent pump frequencies at ω_c, the expression for the wavevector mismatch of the FWM process can be given by [94]:

$$\Delta\beta = \beta(\omega) + \beta(\omega_\ell) - \beta(\omega_c) - \beta(\omega + \omega_\ell - \omega_c), \tag{2.12}$$

where $\omega = \omega_{FWM} + \Omega$. Performing a Taylor expansion around ω_c, Equation (2.12) can now be given as:

$$\Delta\beta = \sum_{n=2} \frac{\beta_{nc}}{n!}\left[(\omega_{c\ell} + \Omega)^n + (-\omega_{c\ell})^n - \Omega^n\right], \tag{2.13}$$

where $\omega_{c\ell} = \omega_c - \omega_\ell$. In addition, Equation (2.13) can be also expanded as a Taylor series around $\omega = \omega_{FWM}$ (or $\Omega = 0$) as:

$$\Delta\beta = \Delta\beta_{\Omega=0} + \Omega\left(\frac{d\Delta\beta}{d\Omega}\right)_{\Omega=0} + \frac{\Omega^2}{2!}\left(\frac{d^2\Delta\beta}{d\Omega^2}\right)_{\Omega=0} + \frac{\Omega^3}{3!}\left(\frac{d^3\Delta\beta}{d\Omega^3}\right)_{\Omega=0} + \cdots \tag{2.14}$$

Notice that the first term Equation (2.14) vanish as it corresponds to the phase-matching condition. Therefore, by using Equations (2.13) and (2.14), $\Delta\beta$ around ω_{FWM} can be given as a function of Ω in terms of the β_n dispersion parameters by the following expressions:

$$\begin{gathered}\Delta\beta = \Omega\sum_{n=2}\frac{\beta_{nc}\omega_{c\ell}^{(n-1)}}{(n-1)!} + \frac{\Omega}{2!}\sum_{n=3}\frac{\beta_{nc}\omega_{c\ell}^{(n-2)}}{(n-2)!} + \frac{\Omega}{3!}\sum_{n=4}\frac{\beta_{nc}\omega_{c\ell}^{(n-3)}}{(n-3)!} + \cdots \\ \beta_{nc} = \sum_{m=n}\frac{\beta_m}{m!}{\omega_{c0}}^m.\end{gathered} \tag{2.15}$$

Taking into account the fact that the minima of the generated FWM spectrum should correspond to $\Delta\beta(\Omega)L/2 = k\pi$ (where k is a natural number), one could, in principle, perform a fitting of the measured Ω frequencies by using Equation (2.15) and estimate the β_n dispersion parameters. However, the accuracy and the highest measurable n^{th}-order dispersion by using this approach would be limited by the amount of measurable Ω frequencies. An example of this measurement will be presented in the following subsection.

2.1.3 Capabilities for dispersion characterization

In Figure 2.4 we show the measured FWM power spectra for different values of λ_ℓ. These spectra were measured in 20 m of DSF and the incoherent-pump was centered close to 1550 nm. Notice that the width of the FWM peak becomes narrower as the laser is tuned away from the incoherent-pump. By using expressions of Equation (2.15) and considering a first-order approximation on Ω and up to the third-order dispersion, it is possible to derive an expression for the width of the FWM peak $\Delta\Omega$ given by [94]:

$$\Delta\Omega \approx \frac{16\pi}{L\beta_3(\omega_{FWM} - \omega_\ell)^2}, \tag{2.16}$$

Moreover, given the short length of fiber (i.e., 20 m) a broader $\Delta\Omega$ is obtained compared with the FWM spectrum generated in fibers of km of length [36], therefore, additional experimental precautions should be taken to accurately measure ω_{FWM} as described in Section 2.3.

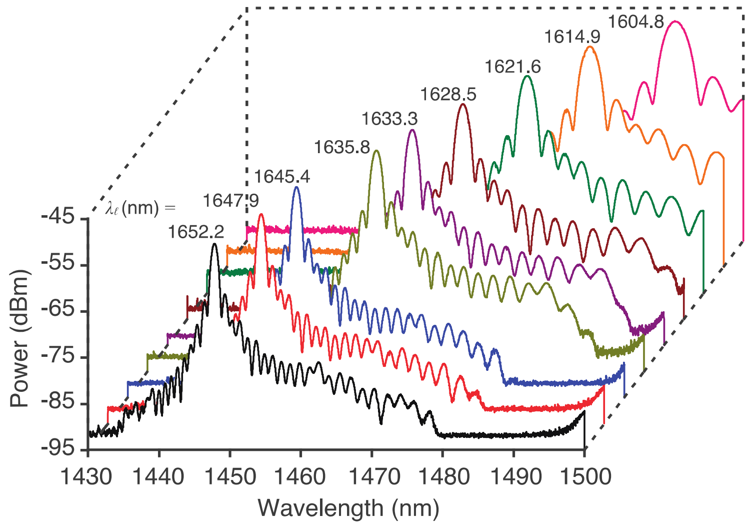

Figure 2.4: Measured FWM power spectra as a function of the laser wavelength. Resolution bandwidth of 100 pm.

As mentioned in the previous subsection, by tuning λ_ℓ and measuring λ_{FWM}, Equation (2.11) can be used as a fitting expression and, then, λ_0 and Ω_{34} (or β_3/β_4) can be obtained as fitting parameters. An example of measured values of λ_{FWM} are plotted as a function of λ_ℓ in Figure 2.5(a) along with the calculation of Equation (2.11) with the fitted $\lambda_0 = 1546.52 \pm 0.02$ nm and $\Omega_{34} = -213 \pm 3$ ps^{-1}. The presented standard deviations of the fitted parameters ($\sigma_{\lambda 0}$ and $\sigma_{\Omega 34}$) where obtained by ensuring that ~68% of the residuals i.e., $\lambda_{FWM} - f(\lambda_\ell, \lambda_0, \Omega_{34})$, lay within the calculated $f(\lambda_\ell, \lambda_0, \Omega_{34}) - f(\lambda_\ell, \lambda_0 \pm \sigma_{\lambda 0}, \Omega_{34})$ and $f(\lambda_\ell, \lambda_0, \Omega_{34}) - f(\lambda_\ell, \lambda_0, \Omega_{34} \pm \sigma_{\Omega 34})$ as illustrated in Figure 2.5(b).

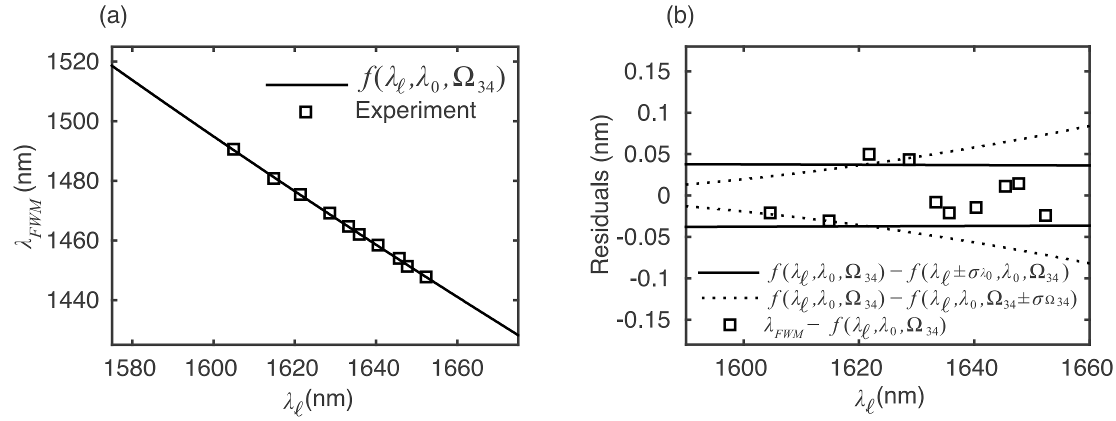

Figure 2.5: (a) Measurement of λ_{FWM} as a function λ_ℓ along with the calculation of $f(\lambda_\ell, \lambda_0, \Omega_{34})$. (b) Estimation of $\sigma_{\lambda 0}$ and $\sigma_{\Omega 34}$.

Another measurement example considers the similarity of the measured FWM spectrum with the one predicted by theory in a uniform fiber (see Figure 2.3 and Figure 2.4). In this case we have chosen the generated FWM power spectrum for the laser tuned at $\lambda_\ell = 1652.2$ nm, which is plotted as a function of Ω in Figure 2.6(a). Considering that at the spectral minima in a uniform fiber $\Delta\beta(\Omega)L/2/\pi = k$, by measuring the Ω frequencies for the minima of Figure 2.6(a) and using Equation (2.15) for $\Delta\beta(\Omega)$, one could estimate the fiber high-order dispersion parameters (i.e., β_n for $n \geq 3$). In Figure 2.6(b) we present the measured $\Delta\beta(\Omega)L/2/\pi = k$ as a function of Ω along with the calculation of Equation (2.15) considering a third-order approximation on Ω and up to the fifth-order dispersion. The fitted dispersion parameters for the calculation of Figure 2.6(b) were $\beta_3 = 0.112 \pm 0.002$ ps^3/km, $\beta_4 = (-5.3 \pm 0.1) \times 10^{-4}$ ps^4/km and $\beta_5 = (7 \pm 4) \times 10^{-6}$ ps^5/km. The convergence of the fitting routine was aided by considering the previously measured $\lambda_0 = 1546.52$ nm and $\Omega_{34} = -213$ ps^{-1} as fixed parameter and, therefore, only β_3 and β_5 were left as fitting parameters. This was justified by the fact that variations within $\pm\sigma_{\lambda 0}$ and $\pm\sigma_{\Omega 34}$ did not modify the fitted β_3 and β_5. The standard deviations of the fitted parameters $\sigma_{\beta 3}$ and $\sigma_{\beta 5}$ were obtained in a similar way as for $\sigma_{\lambda 0}$ and $\sigma_{\Omega 34}$, whereas $\sigma_{\beta 4}$ was obtained by means the relative standard uncertainties of Ω_{34} and β_3 as:

$$\sigma_{\beta 4} = \sqrt{\left(\frac{\sigma_{\Omega 34}}{|\Omega_{34}|}\right)^2 + \left(\frac{\sigma_{\beta 3}}{|\beta_3|}\right)^2}\,|\beta_4| \tag{2.17}$$

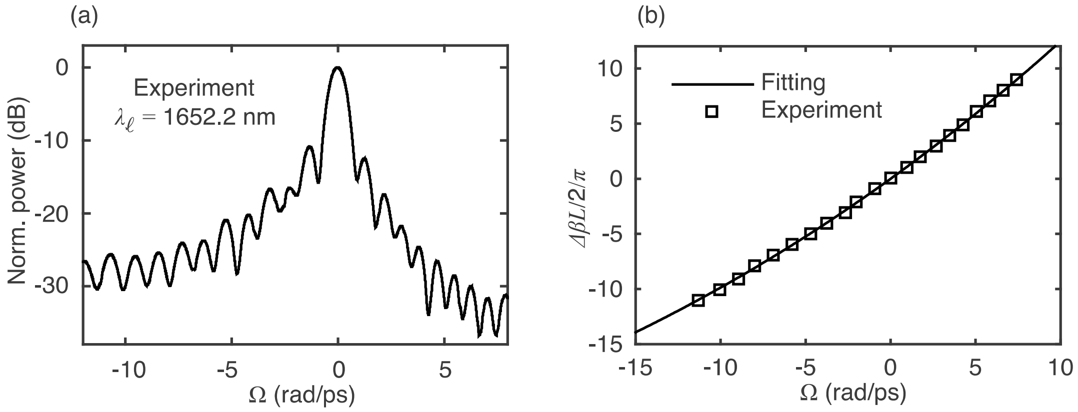

Figure 2.6: (a) Normalized power of the FWM generated spectrum with $\lambda_\ell = 1652.2$ nm as a function of Ω. (b) Measurement of $\Delta\beta L/2/\pi$ as a function Ω along with the calculation using the fitted parameters.

The presented examples show the capabilities of our measuring method in characterizing fiber dispersion, not only zero-dispersion but also high-order dispersion. The first example shows the possibility of measuring λ_0 and β_3/β_4, which will be applicable as long as one could experimentally identify the maximum of the generated FWM spectrum between the incoherent-pump and laser. This would be mostly limited by the applied power and length of the fiber under test as indicated in Equation (2.6). The second example, on the other hand, shows how the high-order dispersion parameters β_3, β_4 and β_5 can be independently measured (however, previous knowledge of λ_0 and β_3/β_4 is required). Although, this approach could be only applicable in fibers (or other optical waveguides) with high-uniformity, to the best of our knowledge, this is the first measurement of the fifth-order dispersion in an optical fiber, which corresponds to a very small quantity and represents a challenging measurement.

2.1.4 Discussion

In this section we have described the main aspects of our dispersion characterization method based on measuring the power spectrum generated by FWM between an incoherent-pump and a laser. We have shown the main characteristics of the FWM power spectrum that is predicted for a uniform fiber and the relationship between these characteristics and the phase-matching condition of the FWM process.

First, by means of the phase-matching condition ($\Delta\beta = 0$) we have derived an expression that relates the wavelength of the FWM power spectrum peak (λ_{FWM}) with that of the laser (λ_ℓ) and dispersion parameters such as of λ_0 and β_3/β_4. This allows to estimate the fiber dispersion parameters by tuning the laser at different λ_ℓ, measuring the values of λ_{FWM} and performing a fitting upon the measured data. The measured values and their estimated standard deviations show the capabilities of our measuring method for accurate estimation of λ_0 and β_3/β_4 in optical fibers.

Second, we have obtained a general expression for the wavevector mismatch around the peak of the FWM power spectrum in terms of fiber dispersion parameters. By exploiting the spectral minima that correspond to the sinc^2 spectral shape predicted in a uniform fiber and using the derived expressions, we have been able to measure for the first time the value of β_5 in an optical fiber. Although this approach is only applicable in fibers with high-uniformity, our measurement demonstrates the capabilities of our method in measuring such a small quantity.

We have chosen DSFs as our fibers under test given two fundamental reasons. First, their λ_0 is located around the 1550 nm spectral band and, therefore, become suitable four our experiments, considering that most of the instrumentation operate at this band (widely used for optical communications). Second, DSFs have a significantly more uniform dispersion than other fibers with λ_0 near 1550 nm, such as highly-nonlinear fibers (HNLFs) and photonic-crystal fibers (PCFs). However, the application of our method has been also demonstrated in fibers with significant nonuniformity [36].

In the next sections we will show the applications of our measuring method in particular experimental examples such as high-order dispersion mapping in a long fiber and the study of the effect of bending in fiber dispersion. In addition, by means of a theoretical example we will show the prospects of applying our method in silicon nano-waveguides.

2.2 High-order Dispersion Mapping

Even though optical fibers are the most uniform optical waveguides, evidenced by their extremely-low propagation losses (i.e., ~0.14 dB/km [99]), random longitudinal fluctuations of fiber dispersion arise from imperfections that result from their fabrication processes (i.e., drawing and preform formation) [29, 95, 28]. Therefore, several dispersion characterization methods have been proposed to obtain information of the longitudinal distribution of dispersion parameters along the fiber by non-destructive means [37 – 46]. These methods are so-called dispersion-mapping techniques and can be classified in different types as follows:

(i) Methods that use CW lasers and measure the FWM parametric gain [40] or the conversion efficiency spectrum [38, 39] at the output of the fiber. Then, numerical methods are used to obtain $\lambda_0(z)$ by fitting the measured spectra. One important limitation of these methods is that the interference between FWM fields of different fiber segments can lead to misleading spectra and, therefore, cause errors in the retrieved $\lambda_0(z)$.

(ii) Methods that measure the power spectrum generated by FWM between two pulses that overlap only over a segment of fiber [41, 42]. The pump wavelength is tuned around λ_0 and the signal is located at a wavelength far from λ_0. Considering that both pulses have a different group velocity, the overlapping region is tuned by varying the initial delay difference between pulses. The spatial resolution of this methods has been attributed to the overlapping region between pulses (i.e., $\sim$700 m was obtained in [41] for a DSF and using pulses of $\sim$100 ps duration). Although the spatial resolution can be improved by using shorter pulses, the spectral broadening of the generated FWM spectrum could be also a limiting factor if the pulse duration is considerably reduced [41, 42].

(iii) Methods based on an optical time-domain reflectometry (OTDR) configuration, in which the power of a wave that is amplified [43] or generated [44] by FWM is measured by means of Rayleigh scattering. In [43], the map of λ_0 is reconstructed by tuning a pump laser around λ_0 (i.e., from the normal to the anomalous dispersion regime) and observing the signal backscattered power. When the pump

matches λ_0, there is an abrupt power increase. In [44], two lasers are used and the OTDR configuration measures the backscattered power of one of the generated FWM frequencies. This power oscillates with an spatial period given by $2\pi/\Delta\beta(z)$, from which $D(z)$ is retrieved. Unfortunately, these methods have shown limited spatial resolution ($\sim$1 km) attributed to the OTDR sensitivity requirements [43, 44].

(iv) Methods that also measure the power oscillations of a wave generated by FWM between two lasers. However, in contrast to the methods of group (iii), a counterpropagating pump pulse is used to provide local gain to the FWM power via SBS. Therefore, instead of measuring the backscattered power using an OTDR configuration, the power oscillations are detected in transmission [45, 46]. In [45], the two CW lasers were used as pumps in the FWM process and a measurement of $D(z)$ was obtained with an spatial resolution of $\sim$20 m for an SMF and $\sim$150 m for a DSF. In [46], the FWM and SBS pumps were pulsed, thus, a remarkable meter-scale resolution was achieved in the measured $\lambda_0(z)$. This was due to the reduced overlapping region between the counter-colliding pulses.

All mentioned dispersion-mapping techniques neglect the effect of HOD or assume a constant value for HOD parameters to retrieve either $\lambda_0(z)$ or $D(z)$. However, given the importance of HOD for several nonlinear optical phenomena, in this section we apply our measuring method to obtain dispersion maps of an optical fiber, not only for λ_0, but for the ratio between third and fourth-order dispersion (β_3/β_4).

We first describe the experimental setup used to implement our method as a dispersion-mapping technique. This was achieved by using short pulses for the incoherent pump and laser of $\sim$40 ps and controlling the initial delay difference between both pulses. Subsequently, we show our measured dispersion maps for a DSF of 7 km with an spatial resolution of $\sim$120 m, that in contrast to the assumption of the authors of [41, 42], corresponds to a shorter length than the overlapping region. In addition, we show our results obtained by numerical calculations of the pulse propagation that are used to explain the limits on the spatial resolution of our dispersion-mapping technique.

2.2.1 Experimental setup for dispersion-mapping

Our dispersion-mapping experimental setup is described in Figure 2.7. The setup can be subdivided in the derivation of the incoherent-pump and laser pulses, and the detection stage.

For the pulsed incoherent-pump, a first EDFA (EDFA1, *Keopsys Pulsed Erbium Fiber Amplifier*) was used as an ASE source. The ASE was pulsed by a (MZM1, *iXblue MXER-LN-20*), driven by a pulse train of ~25 ps pulse width at a 155 MHz repetition rate, generated by a pulse pattern generator (PPG1, *Alnair Labs EPG-200*). The pulsed ASE was then amplified by another EDFA (EDFA2, *Keopsys Pulsed Erbium Fiber Amplifier*) from ~1 mW up to ~10 W (the peak power was measured with the optical input of an oscilloscope with a 28 GHz bandwidth internal photodetector, *Infiniium DCA-J Agilent 86100C*). A segment of 38 m of highly-nonlinear fiber (HNLF with $\gamma \approx 6\ \mathrm{W}^{-1}\ \mathrm{km}^{-1}$ and $\lambda_0 \approx 1554$ nm) was used to expand the spectrum of the high-power ASE pulses, this was due to the bandwidth limitation of our EDFAs (from 1549 to 1567 nm) and the need of centering the incoherent-pump near the $\lambda_0 \approx$ 1550.8 nm of the FUT (previously measured with a commercial instrument, *2008 Chromatic Dispersion Measuring System, by Photon Kinetics*). Finally, an optical band-pass filter (BPF, *Yenista WSM-160*) was used to spectrally slice the generated supercontinuum.

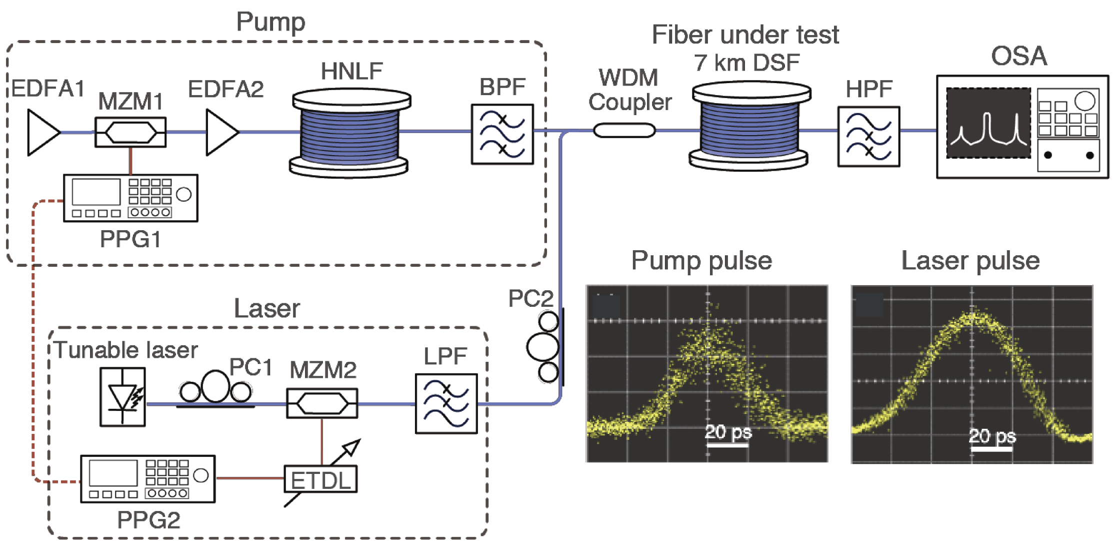

Figure 2.7: Dispersion-mapping experimental setup

For the pulsed laser, an initial tunable laser was modulated by a second MZM (MZM2, with the same bandwidth and extinction ratio specifications as MZM1), driven by a pulse train of

~35 ps pulse width at a 155 MHz repetition rate, generated by PPG2 (*Agilent 81142A*). The polarization controller (PC1) was used to align the laser state-of-polarization and maximize the amplitude modulation of MZM2. An optical low-pass filter (LPF, *AC Photonics*) was used to minimize the laser noise at the wavelength region expected for the generation of the FWM power spectrum, that is between 1490 – 1470 nm when tuning the laser between 1610 – 1630 nm. An electrical time delay line (ETDL, actually an RF phase shifter *Narda 3752*) was used to delay difference between the pump and laser pulses. In this way, the overlapping region between the pump and laser pulses in the FUT can be varied, considering that PPG1 was triggered by PPG2.

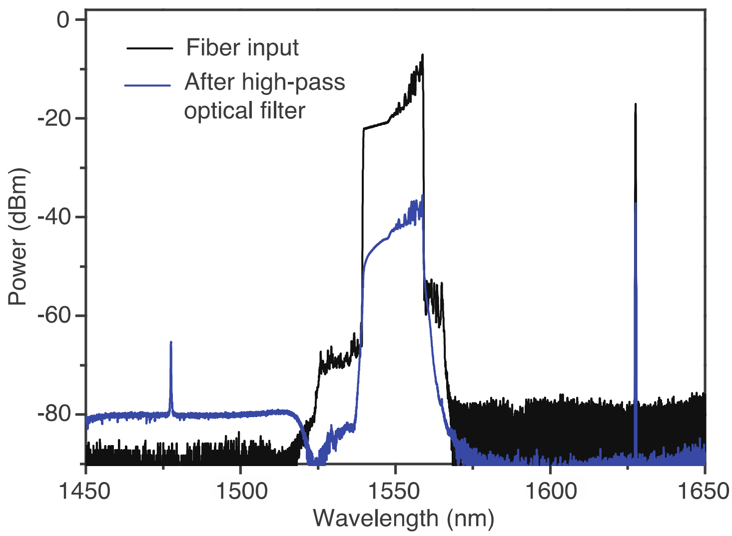

Figure 2.8: Sample spectrum

The pump and laser pulses were coupled into the FUT (7 km of DSF Corning, with $\gamma \approx 2.3$ W^{-1} km^{-1} [34]) via a Wavelength Division Multiplexer (WDM, *AC Photonics*) coupler. At the input of the FUT, the pump and laser pulses had ~200 mW and ~2 mW of peak power, and 39 and 43 ps pulse duration, respectively (see the pulse traces measured with a wide-bandwidth oscilloscope in Figure 2.7). In addition, the input spectrum is illustrated in Figure 2.8, where the incoherent-pump had a bandwidth of ~17 nm and the laser was located at $\lambda_\ell \approx 1627.6$ nm. After the FUT, in order to prevent stray light in the OSA (*Yokogawa AQ6319*) due to the pump and laser, we used a high-pass filter (HPF, with a cutoff wavelength ~1510 nm). The optical spectrum at the output of the HPF is also illustrated in Figure 2.8, where the signal-to-noise ratio (SNR) of the generated FWM spectrum is ~15 dB.

We measured the FWM power spectrum for different laser wavelengths (i.e., $\lambda_\ell =$ 1610.54, 1616.54, 1622.56, 1627.56, and 1632.54 nm). In addition, for each laser wavelength, we varied the delay between pulses at 58 different values, which corresponds to an spatial resolution of $\Delta L \approx 120$ m. Therefore, by measuring ω_{FWM} for the five different values of ω_ℓ we obtain the measured λ_0 and β_3/β_4 for each one of the 58 segments of the FUT.

In order to improve the accuracy of our measurements, we made the following verifications: (i) we isolated the fiber from excessive temperature variations inside a container and monitored the temperature inside. We assured a $\Delta T \lesssim 1$°C and, thus, minimized the temperature-induced shift of dispersion, considering that $d\lambda_0/dT \approx 0.03$ nm/°C in DSFs [100]. (ii) We verified that there was no FWM generation when the pulses overlapped outside the FUT to define the initial and final segments of the fiber. This can be assumed, since for the power levels used in our experiments the FWM efficiency is negligible due to the large chromatic dispersion in the connecting fibers used in or experiments (made of SMF-28 with $D \approx 17$ ps nm^{-1} km^{-1} at 1550 nm). (iii) We verified that ω_{FWM} did not shift when varying either the pumping power or the laser state-of-polarization via PC2. This allow us to verify that the phase-matching condition was power-independent and disregard any effect of fiber birefringence, respectively.

2.2.2 Results of dispersion mapping

Our measured dispersion maps for λ_0 and β_3/β_4 are presented in Figure 2.9(a) and Figure 2.9(b) respectively. Our measurements show that λ_0 and β_3/β_4 vary along the fiber, respectively, with means $\langle\lambda_0\rangle \approx 1550.5$ nm and $\langle\beta_3/\beta_4\rangle \approx -220$ ps^{-1} and standard deviations $\sigma(\lambda_0) \approx 0.1$ nm and $\sigma(\beta_3/\beta_4) \approx 10$ ps^{-1}. The standard deviation for each fiber segment (shadow areas in Figure 2.9) was calculated as explained in section 2.1. Our dispersion maps show also a correlation between λ_0 and β_3/β_4 along the fiber. A high dispersion fluctuation can be identified from 0 to 3.5 km and from 5.5 to 7 km. In contrast, the region between 3.5 and 5.5 km presents a more uniform dispersion. Therefore, our method could, in principle, be used to select a segment of uniform fiber to build a parametric device with high-efficiency.

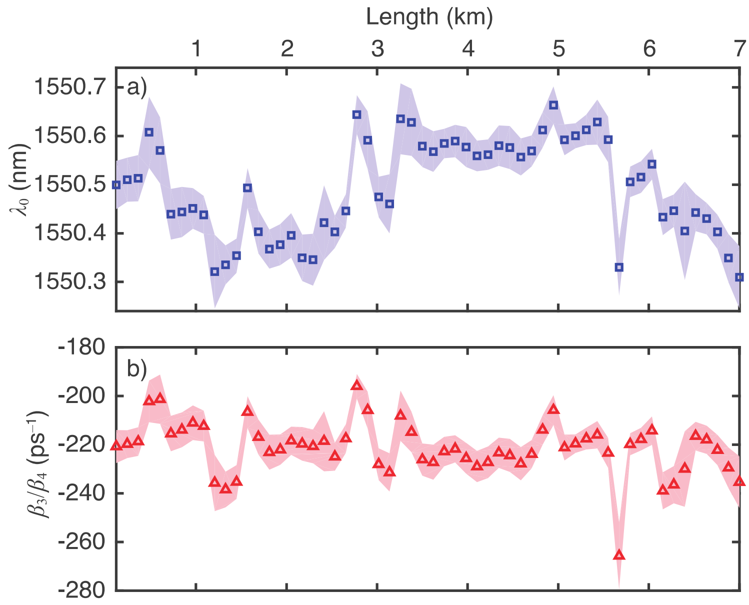

Figure 2.9: Dispersion maps for: (a) the zero-dispersion wavelength (λ_0) and (b) the ratio between third and fourth-order dispersion (β_3/β_4). Spatial resolution of 120 m.

A clear example of the effect of fiber dispersion fluctuations in $\Delta\beta(z)$ is the measured longitudinal evolution of FWM power spectrum. Thus, in Figure 2.10(a) we illustrate the normalized FWM power spectrum when using $\lambda_\ell = 1632.54$ nm for the different segments of the fiber. Note that the FWM spectrum shifts over a wavelength region of ~0.6 nm, thus, if the effect of HOD is neglected one could attribute this variation to an overestimated fluctuation of $\sigma\lambda_0 \approx 0.3$ nm.

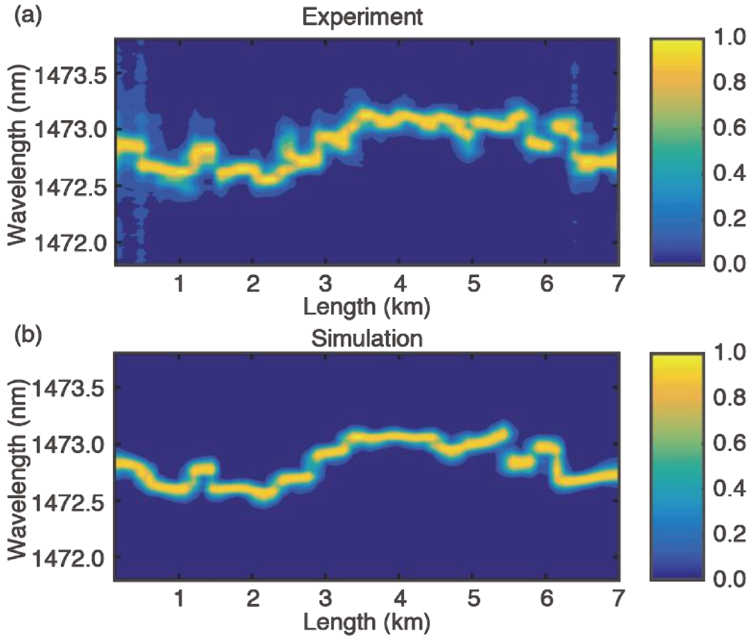

Figure 2.10: Evolution of the normalized FWM power spectrum along the fiber. (a) Experiments and (b) simulations using the generalized NLSE. Spatial resolution of 120 m. Calculations were performed by the Ph.D student Daniel F. Londoño.

We have also included in Figure 2.10(b) the numerical calculation of the FWM power spectrum for the same λ_ℓ used in measurements of Figure 2.10(a). For this calculation we have assumed 58 concatenated fibers with a longitudinal distribution of λ_0 given by Figure 2.9(a). In addition, by using the mean value $\langle\beta_3\rangle \approx$ 0.123 ps^3/km (previously measured with a commercial chromatic dispersion measuring system) and $\langle\beta_3/\beta_4\rangle \approx$ –220 ps^{-1} from our measured dispersion map, we can obtain a mean value for $\langle\beta_4\rangle \approx$ –5.6 × 10^{-4} ps^4/km. From our calculation of fiber dispersion (explained later) and experiments in similar fibers, we have observed that β_3 is more susceptible to changes in fiber geometry than β_4. Therefore, for the calculation of Figure 2.10(b) we have assumed a constant $\langle\beta_4\rangle$ over the 58 concatenated fibers and a variation of $\beta_3(z)$, obtained by using the dispersion map for β_3/β_4 [Figure 2.9(b)] and $\langle\beta_4\rangle \approx$ –5.6 × 10^{-4} ps^4/km. The calculation of the FWM power spectrum was performed by using a similar approach as the experiments. That is, obtaining the FWM power spectrum for each one of the 58 fibers by changing the initial delay between pump and laser pulses, and by using the same spectral and power conditions of the pulses used in our experiments. The pulse propagation was calculated by solving the generalized scalar Nonlinear Schrödinger Equation

(NLSE) by means of the Split-step Fourier Method as described in [101]. Note from Figure 2.10(a) and Figure 2.10(b) that our calculations are in good agreement with our experiments.

In order to judge possible causes of the measured dispersion fluctuations in the tested optical fiber, we have performed numerical calculations of fiber dispersion. For this numerical study we have modeled a fiber refractive index profile (RIP) similar to the measured RIP of the FUT [see Figure 2.11(a)]. The modeled RIP was obtained by sweeping the core inner radius and dopant concentration (i.e., the base and the height of the inner triangular core) until a nearly good agreement with the measured $\langle\lambda_0\rangle$ and $\langle\beta_3/\beta_4\rangle$ was achieved. For the calculations we used a numerical model of a multi-layered step-index profile, similar to the one used in [102]. From this model, we obtain the propagation constant $\beta(\omega)$ for a range of ω (equivalent to wavelength range from 1330 to 1860 nm) and then, we apply finite-difference numerical differentiation to calculate $d\beta^n(\omega)/d\omega^n$. For the core dopant we assumed different concentrations of germanium and the refractive indices were obtained by means of the Sellmeier model for GeO_2-SiO_2 glasses presented in [103]. For the cladding we assumed boron as dopant and obtained the refractive index from [104].

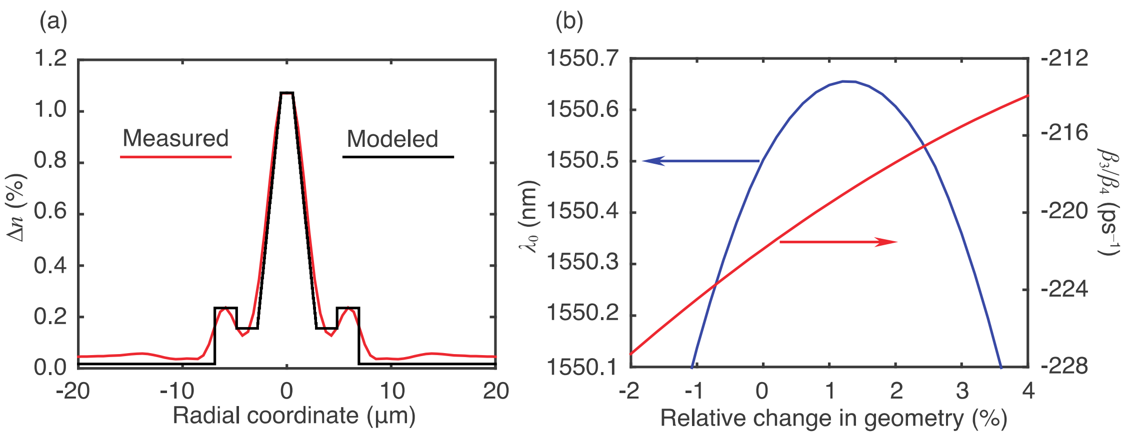

Figure 2.11: (a) Measured and modeled fiber refractive index profile. (b) Variation of λ_0 and β_3/β_4 as a funciton of relative changes in fiber geometry. Calculations performed by the Ph.D student Daniel F. Londoño.

By observing the measured RIP of the FUT in Figure 2.11(a) one may anticipate different types of modifications as a consequence of preform fabrication and drawing processes. However, one of the most expected modifications would correspond to a uniform deformation over the entire geometry. Therefore, we have evaluated how λ_0 and β_3/β_4 change as a function of a relative change in geometry, that is varying the fiber core radius while the entire geometry changes proportionally. The results of this evaluation are presented in Figure 2.11(b). Note that the range of variations of λ_0 observed in the dispersion map of Figure 2.9(a) (i.e., from 1550.3 to 1550.7 nm) is well-explained by relative changes in geometry within $\pm$ 1% (i.e. a change in the core radius of $\pm$ 28 nm). In the case of high-order dispersion, for a relative change of $\pm$ 1% the calculated variation of β_3/β_4 is around $\pm$ 2.5 ps^{-1}, which corresponds to a smaller variation than the observed in the dispersion map of Figure 2.9(b). We believe that this difference could be attributed to our limited accuracy in measuring β_3/β_4 (i.e., approximately 7 ps^{-1}) and/or to other possible RIP modifications different than the uniform deformation considered in our study. However, our simulations are in agreement with our experiments in two ways. First, the variations of λ_0 are comparatively smaller than those for β_3/β_4 (i.e., variations in λ_0 of the order of 0.01% compared with variations in β_3/β_4 between 1 and 5%). Second, the calculated variations of λ_0 and β_3/β_4 within $\pm$ 1% of relative change in geometry of Figure 2.11(b) could, in principle, explain the observed correlation between the dispersion maps of Figure 2.9(a) and Figure 2.9(b).

2.2.3 Discussion

In this section we have demonstrated a non-destructive spatially-resolved measurement of the zero-dispersion wavelength and, for the first time to the best of our knowledge, of high-order dispersion in an optical fiber. This was achieved by implementing a dispersion-mapping version of our measuring method based on FWM between an incoherent-pump and a laser. By using pulses as short as $\sim$40 ps (FWHM duration) and tuning the overlapping region between pulses along the fiber, we have obtained dispersion maps with an spatial resolution of $\Delta L \approx$ 120 m in a DSF. The measured dispersion maps show a correlation between the observed fluctuation for λ_0 and that of β_3/β_4, and also that λ_0 presents a comparatively smaller fluctuation than that of β_3/β_4 (i.e., variations of the order of 0.01% in λ_0 and 5% in β_3/β_4). By performing numerical calculations of an approximated fiber refractive index profile, these observations could be, in part, explained by fluctuations of fiber geometry (around $\pm$ 1%) as a result of preform fabrication and drawing processes. In addition, numerical calculations of pulse propagation are in good agreement with our experiments, displaying the same evolution of the measured FWM spectrum along the fiber when assuming a longitudinal dispersion distribution given by our dispersion maps.

Other important characteristic of dispersion-mapping techniques is the minimum length-scale at which changes on fiber dispersion could be detected. Our measurements performed with $\Delta L \approx 120$ m evidence clear shifts in the measured dispersion maps and FWM power spectrum of Figure 2.9 and Figure 2.10 respectively. Surprisingly, this ΔL is smaller than the overlap region between the used pulses (i.e., $\sim$380 m from our numerical calculations for full with at half maximum). This is in contrast to previous experiments using FWM between overlapping pulses, group (ii) methods [41, 42], in which the authors have assumed that the spatial resolution is limited by the overlap region between pulses. In our experiments, ΔL was limited by the delay step used, which was manually modified by the RF phase-shifter used as a TDL. Therefore, if experiments were performed with a finer delay step and an automatic acquisition of the FWM spectra, in principle, a better spatial resolution could be achievable. However, one question that arises is what is the smallest achievable spatial resolution of our dispersion-mapping technique? However, there is no simple explanation for the limit on the spatial resolution of our method, as it depends on several parameters such as pulse duration, rising and falling times, laser wavelength, dispersion parameters, etc.

Given the good accuracy in measuring dispersion parameters (i.e., $\sim$40 pm in in λ_0 and $\sim$7 ps^{-1} in β_3/β_4), our dispersion-mapping technique becomes suitable to be applied in fibers that exhibit more uniform dispersion than common HNLFs, for instance, DSFs and novel fibers that have been specially designed and/or fabricated to be robust against geometry fluctuations [95, 31, 105, 102]. In addition, considering that either using more separated wavelengths (for the laser and incoherent pump) or evaluating more-dispersive waveguides (e.g. high-index contrast waveguides) our method could, in principle, have a smaller spatial resolution due to the higher group delay difference between pulses. Therefore, our dispersion-mapping technique could be useful in the development of parametric devices, not only in optical fibers, but also in other integrated-waveguide structures.

2.3 Shift of Zero Dispersion Wavelength with Bending in Optical Fibers

In order to develop compact fiber optical parametric devices, optical fibers must be bent to reduce space, sometimes over tight bending radii [106, 107]. Therefore, understanding how bending modifies the dispersion characteristics of an optical fiber becomes relevant, considering the high-sensitivity of phase-matched FWM to minute changes of dispersion. For instance, a variation of 0.1 nm in λ_0($\sim$1550 nm) can lead to a significant reduction in the parametric gain [85].

Considering that bending has a significant effect in the propagation properties of optical fibers, many studies have focused on bending-induced losses. However, the bending-induced changes in fiber dispersion (particularly the shift of λ_0, $\Delta\lambda_0$) have been comparatively less studied [108, 109]. This could be attributed to the limitation of accurately measuring $\Delta\lambda_0$ as a function of the bending radius (R_b) taking into account different factors: (i) the tested fiber must be bent over a single-layer with a constant R_b to avoid the effect of microbending, which becomes more practical for shorter lengths of fiber. (ii) Considering that $\Delta\lambda_0$ is nonlinear with R_b, the employed measuring method must be sensitive enough to measure small changes of λ_0. (iii) Given the longitudinal nonuniformities of optical fibers that lead to fluctuations of λ_0 [28, 30], it would be preferable to assure that the tested fiber is uniform enough, so the measured shift corresponds to a uniform λ_0 along the fiber.

Therefore, given the challenges in accurately measuring $\Delta\lambda_0$ with bending in an optical fiber, we believe that this is a good opportunity to demonstrate the capabilities of our measuring method. By using high-power pulsed sources (i.e., $\sim$3 W and $\sim$200 mW of peak power for the incoherent-pump and laser, respectively), we were able to measure $\Delta\lambda_0(R_b)$ in a DSF (Corning) as short as 20 m. Although, we had to overcome additional experimental challenges to be able to assure the uniformity of the tested fiber and measure $\Delta\lambda_0$ as small as $\Delta\lambda_0 \approx$ 40 pm, as we will describe in the next section.

We have also performed calculations of the dependence of λ_0 with bending by means of a numerical model of the DSF. Our numerical calculations, based on conformal mapping [110, 111, 112] and the finite-element method (FEM), are in good agreement with our experimental results. In addition, our numerical calculations allowed us to explain the observed $\Delta\lambda_0$ in terms of the mode profile deformation and changes in fiber geometry. This explanation along with the main results of our study could, in principle, be useful in the development compact fiber optical parametric devices and other bent-waveguide structures [113, 114].

2.3.1 Experimental setup for measuring the dispersion shift in bent fibers

The general description of the experimental setup is presented in Figure 2.12(a). The incoherent pump [see Figure 2.12(b) and description below] had $\sim$3 W peak power and $\sim$32 nm of bandwidth (centered around 1550 nm). The tunable laser [see Figure 2.12(c) and description below] had $\sim$200 mW peak power and it was tuned in the range of 1600 −1650 nm.

We selected a pulse duration of $\sim$20 ns and a repetition rate of 100 kHz for the incoherent pump and tunable laser (i.e., –27 dB duty cycle). The selected pulse duration corresponds to the response limit of the used acousto-optic modulators (*Gooch&Housego T-M200*). We did not used a pulse width longer than this limit to prevent SBS inside the EDFA used in the tunable laser. The repetition rate, on the other hand, was selected considering the trade-off between the SNR of the measured spectrum and the peak power obtained from the EDFAs. That is, for a higher repetition rate a larger SNR is expected, whereas for a lower repetition rate a higher peak power can be extracted from the EDFAs.

Even though high-peak power levels were required, considering the short fiber length and the low nonlinear coefficient of the DSF (i.e. $\gamma \approx$ 2.3 W^{-1} km^{-1} [34]), we assured that our measurements were performed below the parametric gain regime ($\gamma PL \gtrsim 1$). This allows to keep the phase matching condition to be power-independent and, therefore, the peak of the FWM power spectrum does not change with the applied power. We verified this in our experiments by varying the power of the incoherent pump and laser and ensuring that ω_{FWM} did not change.

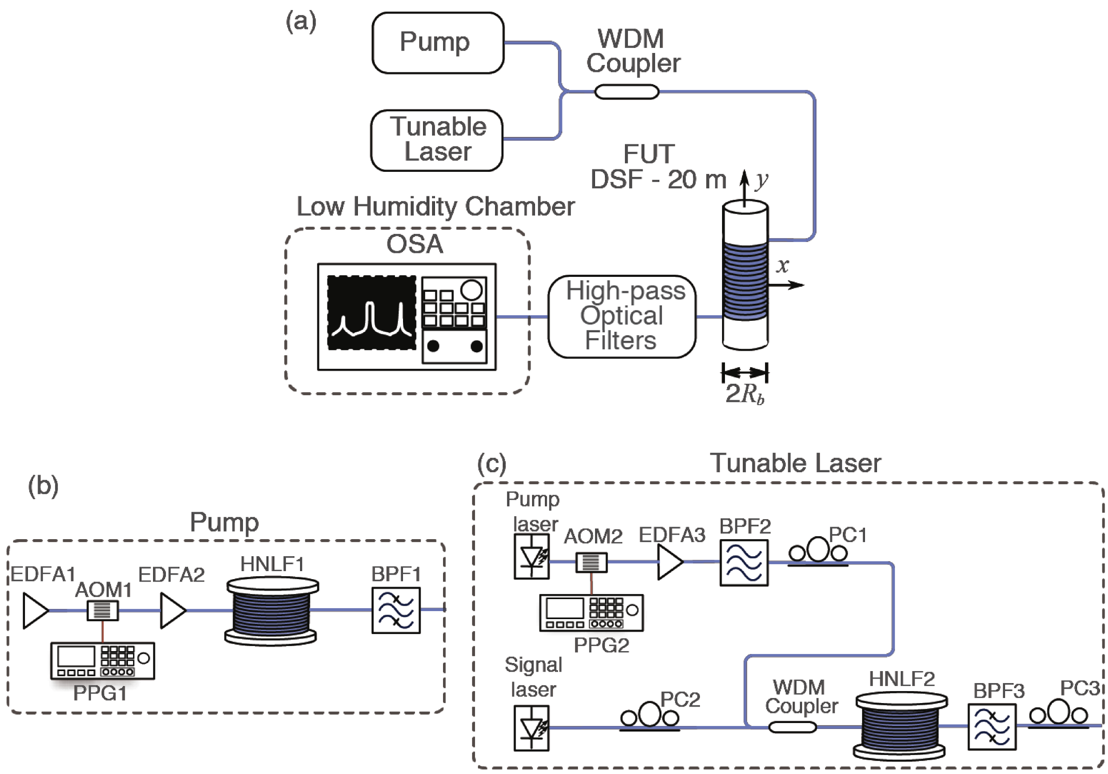

Figure 2.12: Experimental setup. (a) General description. (b) Detailed pump setup. (c) Detailed tunable laser setup.

The detailed description of the incoherent pump and tunable laser is given as follows:

<u>*Incoherent pump*</u>: An EDFA (EDFA1, *IPG Photonics C-band amplifier*) was used as an amplified spontaneous emission (ASE) source. The acousto-optic modulator (AOM1 with $>$ 40 dB of extinction ratio) was used to modulate the ASE, obtaining incoherent optical pulses of $\sim$10 mW peak power (measured with a 1 GHz bandwidth photodetector, *EOT ET-3010*). Another EDFA (EDFA2, *Keopsys Pulsed Erbium Fiber Amplifier*) was used to amplify the peak power of the pulsed ASE up to $\sim$100 W. The gain bandwidth of EDFA2 is limited between 1546 and 1564 nm, thus, it was not possible to center the obtained ASE spectrum close to $\lambda_0 \approx 1546$ nm of the FUT. Therefore, we broadened the ASE spectrum passing the high-power pulses through 2 m of highly non-linear fiber (HNLF1 with $\gamma \approx 14$ W^{-1} km^{-1} and $\lambda_0 \approx 1560$ nm). Finally, a band-pass filter (BPF1, *Yenista WSM-160*) was used to spectrally slice the generated supercontinuum.

<u>*Tunable laser*</u>: We constructed the tunable laser by means of FWM-based wavelength conversion, given the spectral and power limitation of the tunable lasers available in our laboratory. A pump laser near 1550 nm was modulated by AOM2 and amplified by EDFA3 (*Keopsys Pulsed Erbium Fiber Amplifier*). The amplified pulsed train was filtered by BPF2 (*OZ Optics Manually Adjustable Tunable Filter*) to suppress out-of-band ASE, obtaining pump pulses of $\sim$10 W peak power. The pump and a CW signal were coupled into HNLF2 (with 100 m, $\gamma \approx 6$ W^{-1} km^{-1} and $\lambda_0 \approx$ 1554 nm) by means of a WDM coupler (*AC Photonics*) to perform wavelength conversion. The polarization controllers (PC1 and PC2) were used to align the polarizations of the pump and signal, thus, maximizing the conversion efficiency. By tuning the signal from 1464 nm to 1510 nm, we generate and idler around 1600 – 1650 nm. We selected the generated idler by means of BPF3 (*Yenista XTM-50*), obtaining a pulse peak power of ~ 200 mW.

Both the incoherent pump and tunable laser were coupled into the FUT (i.e., 20 m of DSF-Corning) via a WDM coupler (*AC Photonics*). A sample of the optical spectrum at the output of the FUT is presented in Figure 2.13. Notice that the generated FWM spectrum is at most 15 dB higher than the background noise of the OSA. Therefore, we used a series of three high-pass optical filters (*AC Photonics*) to suppress the pump and laser and then minimize the so-called stray light inside the OSA (*Yokogawa AQ6319*). In this way, we were able to observe details of the FWM spectrum below – 60 dBm with an spectral resolution of 100 pm [see the inset of Figure 2.13]. We want to point out that the observed spectral details of the generated FWM spectrum correspond to the sinc^2 function predicted by theory and, to the best of our knowledge, this observation was not reported before in the literature. Thus, we were able to assure that the FUT has a uniform dispersion along its length.

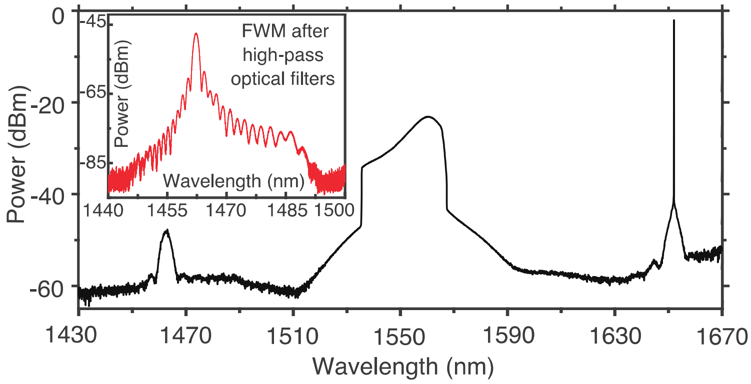

Figure 2.13: Optical spectrum at the output of the fiber (Inset: optical spectrum after high-pass optical filters). Resolution bandwidth of 100 pm.

Other experimental challenge that we needed to overcome, in order to accurately measure the peak frequency of the FWM spectrum (ω_{FWM}), was the presence of spectral dips due to absorption of water vapor inside the OSA. In Figure 2.14(a) we show a sample of the measured FWM power spectrum under typical humidity conditions inside the laboratory (i.e. relative humidity of 31%). Note that the evidenced absorption lines distort the FWM power spectrum and lead to an inaccurate estimation of ω_{FWM}, which is obtained by a fitting routine. Therefore, we have placed OSA inside a constructed low-humidity chamber as illustrated in Figure 2.14(b). The constructed chamber was sealed and filled with 4 kg of silica gel and nitrogen gas. In Figure 2.14(a) we present also two power spectra of an ASE source that show the reduction of the absorption lines when dropping the relative humidity from 44% down to 7% inside the chamber.

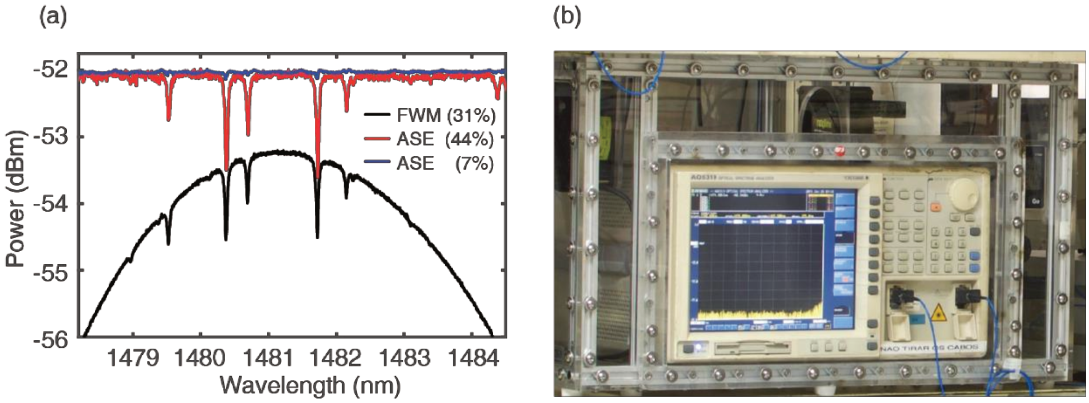

Figure 2.14: (a) Sample spectra of water vapor absorption lines and its effect in the FWM power spectrum (Resoltion bandwidth of 10 pm). (b) Low humidity chamber construted to place the OSA inside a low relative humidity environment.

2.3.2 Results of the shift of zero dispersion wavelength with bending

Our measurements were performed by coiling the FUT over glass cylinders of different radii. The smooth surface of the cylinders and the possibility to bend the fiber over a single layer with a constant R_b, allowed us to avoid the influence of micro-bending in our measurements. In Figure 2.15 we show the measured FWM power spectrum with the fiber bent at different bending radii (i.e., R_b = 4.0, 2.0, 1.5, 1.2 and 1.0 cm) and keeping the laser at the same $\lambda_\ell \approx$ 1640.4 nm. Note that there is a clear shift of the FWM power spectrum to longer wavelengths, which evidences that λ_0 is also shifted in the same direction.

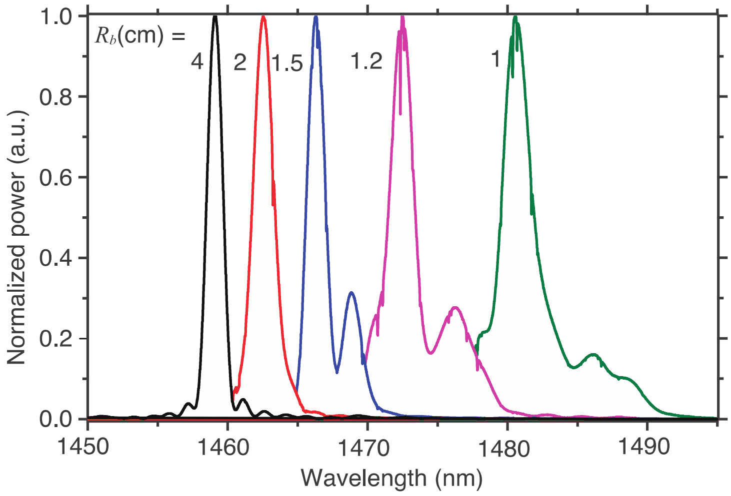

Figure 2.15: Generated FWM power spectra with the same $\lambda_\ell \approx 1640.4$ nm and different bending radii. Resoltion bandwidth of 10 pm.

We want to point out that $\Delta\lambda_0(R_b)$ is related but not proportional to the shift observed in Figure 2.15. Therefore, in order to accurately measure $\lambda_0(R_b)$ (which is presented in Figure 2.16) we performed several measurements of ω_{FWM} by tuning λ_ℓ over different wavelengths for each bending radius. In addition, considering that bending induces a change on fiber birefringence [110, 115] which from our calculations increases from $\Delta n = |n_x - n_y| \approx 10^{-9}$ for $R_b = 10$ cm to $\approx 10^{-7}$ for $R_b = 1$ cm, the FWM is deformed as R_b is reduced (see also Figure 2.15). In our experiments, we identified that this deformation depends only on the laser state of polarization (SOP), which is expected considering that the incoherent pump is unpolarized. According to our calculations, we assumed that there is larger $\Delta\lambda_0(R_b)$ for the x polarization of the laser field [with the cylinder aligned to y as shown in Figure 2.12(a)]. Therefore, we were able to measure a larger $\Delta\lambda_0$ for all values of R_b (circles in Figure 2.16) by controlling the SOP of the laser with a polarization controller [PC3 in Figure 2.12(c)]. In contrast, for the y polarization of the laser field that correspond to a minor shift on λ_0, we were only able to measure $\lambda_0(R_b)$ for $R_b \approx 3.0$ and 4.0 cm (triangles in Figure 2.16). This was due to the deformation caused by the bending-induced birefringence, which did not allowed accurate measurements of λ_0 for the y polarization. In addition, we present in Figure 2.16 our calculations of λ_0 as a function of R_b for x and y polarizations, obtained from our numerical model of the FUT.

As explained in Section 2.1, by employing our measuring method we were also able to measure high-order dispersion. Our measurements reveal that the ratio between third and fourth-order is approximately $\beta_3/\beta_4 \approx -213$ ps^{-1} and keeps unchanged from $R_b = 10.0$ to 4.0 cm. In addition, by using the width of the FWM spectrum we independently measured $\beta_3 \approx 0.114$ ps^3/km and by using the measured β_3/β_4, we found $\beta_4 \approx -5.3 \times 10^{-4}$ ps^3/km. Our numerical calculations are also in agreement with the measured values of high-order dispersion, at least for $R_b = 10.0$ cm, and from $R_b = 10.0$ to 4.0 cm our calculation show that these quantities vary slightly (i.e., less than 2%). For tight bending radii ($R_b < 4$ cm), on the other hand, we were not able to measure high-order dispersion considering the deformation of the FWM due to the bending-induced birefringence and that our method is more robust for measuring λ_0 than high-order dispersion.

Given the good agreement between our numerical model and our measurements, we also evaluated the total fiber loss of the fiber as a function of R_b. This calculation is also presented in in Figure 2.16 (right axis) along with the measured value for $R_b = 1$ cm (star). For larger R_b, we could not perform loss measurements since the loss was within the error of the used power meter (i.e., 0.4 dB). One important observation from Figure 2.16 is that bending-induced loss is noticeable for very tight values of R_b, whereas $\Delta\lambda_0$ is measurable from R_b as large as 8 cm.

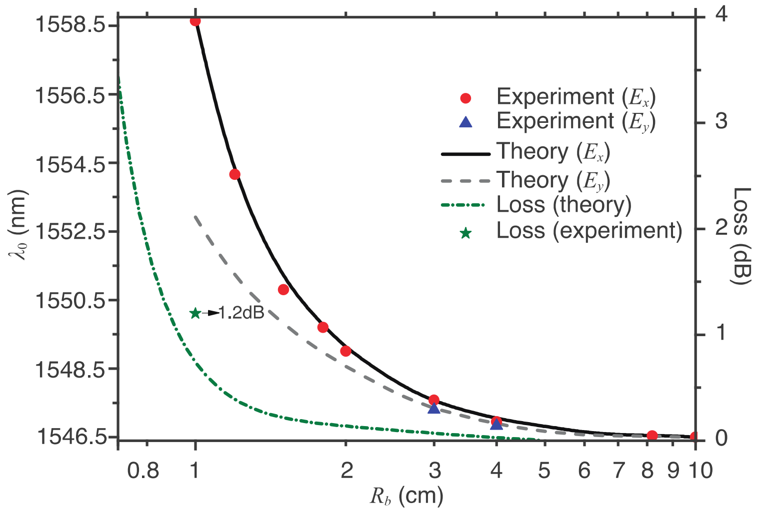

Figure 2.16: Measured and calculated zero-dispersion wavelength (left axis). Calculated total fiber loss as a function of the bending radius (right axis). The star symbol corresponds to the measured value of fiber total loss. Calculations were performed by Dr. Jhonattan C. Ramirez.

For the numerical model of the FUT we used an approximate fiber profile for the DSF that consisted in a step-index core with a raised-index ring. The raised-index ring is usually implemented in DSFs considering that reduces bending losses and allows low splicing loss with an SMF [116, 117]. The modeled fiber profile (actually, the conformal mapped profile for $R_b = 10$ cm) is illustrated in Figure 2.17(a) along with design parameters such as the refractive indices of the core, ring and cladding (i.e., n_{core}, n_{ring} and n_{cladd}); and the radii of the core, and the inner and outer side of the ring (i.e., r_c, r_i and r_o). In order to take into account the effect of bending in our model, we have employed a widely-used method known as conformal mapping [110, 111, 112, 118]. This method allows to perform the modal analysis of the fiber in a transformed coordinate system, where the bent fiber with the original fiber profile $n_b(x)$ is transformed into an straight fiber with a modified refractive index profile given by [110, 112]:

$$n_t(u) = n_b(x) exp\left(\frac{u}{R_b}\right), \tag{2.18}$$

where $u = R_b \ln(x/R_b)$ is the horizontal component of the transformation coordinate system. In addition, we also consider the photo-elastic effect to account for the bending-induced changes of $n_b(x)$ due to compressive and tensile stresses in the inner and outer side of the fiber respectively. Thus, $n_b(x)$ is defined as [110, 115]:

$$n_b(x) = n_s(x)\left\{1 - \frac{n_s(x)^2 x}{2R_b}[P_{12} - \nu(P_{11} + P_{12})]\right\}, \tag{2.19}$$

where $n_s(x)$ is the fiber profile without stress, $\nu = 0.2$ is the Poisson's ratio, and $P_{11} = 0.121$ and $P_{11} = 0.270$ are the SiO_2 photo-elastic tensor components. We have assumed a pure SiO_2 cladding for n_{cladd} and refractive index differences $\Delta n_{core} \approx 0.5\%$ and $\Delta n_{ring} \approx 0.05\%$ for the core and raised-index ring respectively. All refractive indices were obtained from the model proposed in [103] for GeO_2-SiO_2 glasses (Table 2.1 summarizes the fiber profile parameters used in our calculations). The conformal mapped refractive index profiles were then used to calculate $\lambda_0(R_b)$. This calculation was based on a 2D modal analysis performed by means of the finite-element method, employing the commercial simulation software COMSOL Multiphysics. The calculation of λ_0, for each R_b, consisted of estimating the propagation constant $\beta(\omega)$ for a wide range of frequencies (i.e. equivalent to a wavelength range between 1000 and 1800 nm). Subsequently, the derivatives $d^n\beta(\omega)/d\omega^n$ were estimated by using finite-diference differentiation [119]. The calculated values of λ_0 are then determined by evaluating the zero-crossing point of the group velocity dispersion ($\beta_2 = d^2\beta(\omega)/d\omega^2$, GVD).

Simulation parameter	Value
Core radius (r_c)	2.1 μm
Inner ring radius (r_i)	4.6 μm
Outer ring radius (r_o)	6.6 μm
Cladding refractive index (n_{cladd})	1.444
Core refractive index difference (Δn_{core})	~0.5%
Ring refractive index difference (Δn_{ring})	~0.05%

Table 2.1: Summary of geometrical and refractive index parameters used for the numerical model of the FUT.

We present the fiber refractive index profiles obtained by means of conformal mapping in Figure 2.17(a) and Figure 2.17(b) for $R_b = 10$ and 0.5 cm respectively. The mode normalized intensities obtained via FEM numerical calculations are also presented in Figure 2.17(c) and Figure 2.17 (d) for $R_b = 10$ and 0.5 cm respectively. Note that the profile for $R_b = 10$ cm represents well the case of an straight fiber (i.e., $R_b = \infty$) as there is no evident deformation in either the conformal mapped profile or the mode intensity distribution. In contrast, for the case of $R_b = 0.5$ cm the conformal mapped profile is significantly tilted, and the mode intensity distribution displays a significant asymmetry. Even though considerable energy has moved away from the bending axis [i.e., to the right in Figure 2.17 (d)], most of the intensity is still inside the core and, thus, the mode becomes more confined inside the fiber. This can be further evidenced by means of the reduction of the shadowed area from Figure 2.17(a) to Figure 2.17(b), considering that this area corresponds to the region of higher intensity for each case (i.e., above 50% of the peak intensity).

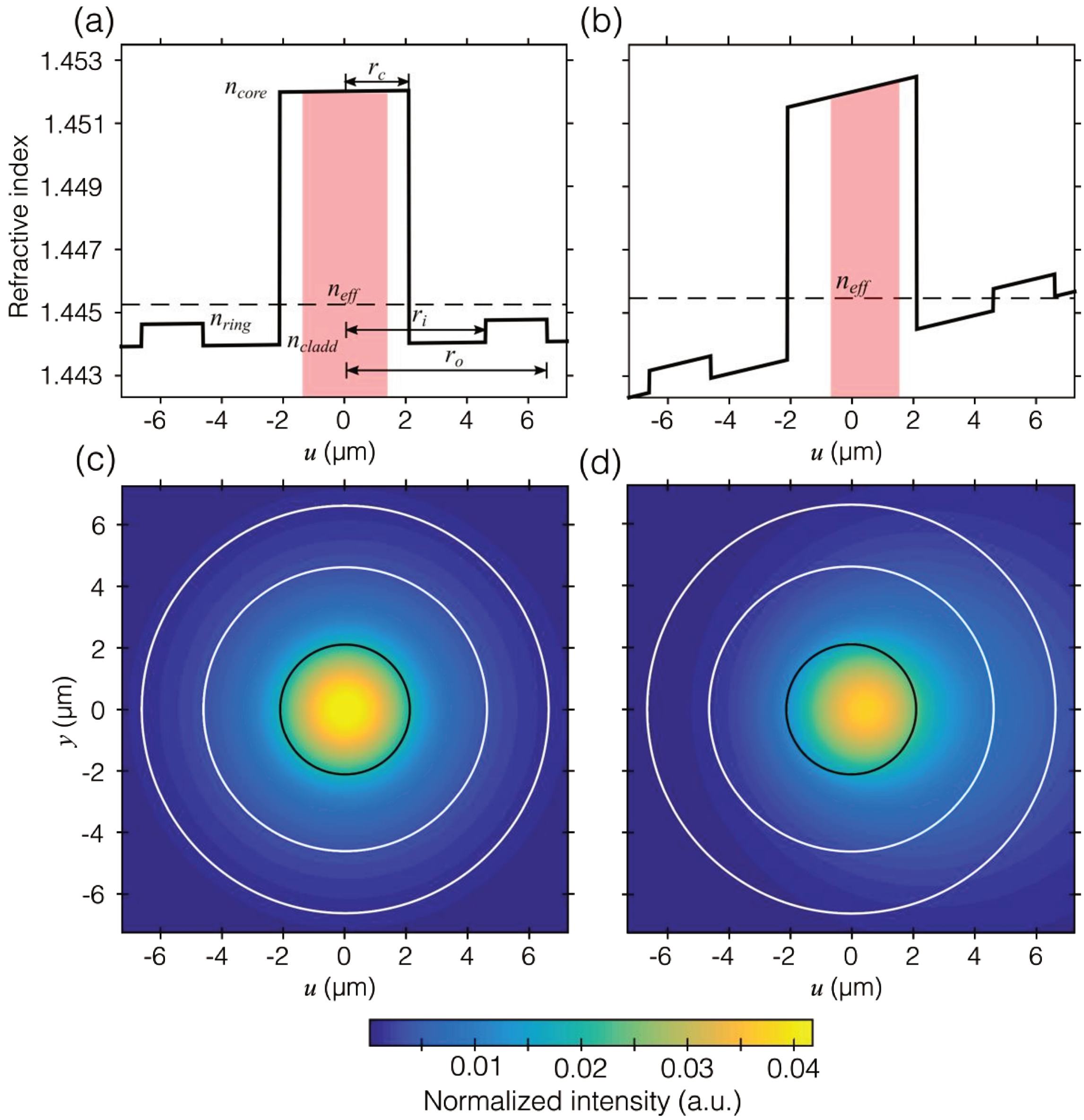

Figure 2.17: Conformal transformation of the fiber refractive index profile for (a) 10 and (b) 0.5 cm bending radii. Normalized intensity for (c) 10 and (d) 0.5 cm bending radii. Calculations performed by Dr. Jhonattan C. Ramirez.

The observation of a positive $\Delta\lambda_0$ with bending in Figure 2.16 (i.e., by reducing R_b, λ_0 is shifted longer wavelengths) and the increase in the mode confinement illustrated in Figure 2.17, make us believe that there is relationship between the change of dispersion induced by bending and that induced by changes of fiber geometry. Therefore, we have calculated how λ_0 is shifted when varying r_c in our DSF model summarized in Table 2.1 (the parameters r_i and r_o were varied proportionally). For this calculation, presented in Figure 2.18, we have assumed $R_b = \infty$. The profile of point B (i.e., $r_c = 2.1$ μm) matches $\lambda_0(R_b = \infty) = 1546.48$ nm. Note that by reducing r_c from this point, λ_0 is also shifted to longer wavelengths (over the range of our measurements presented in Figure 2.16). Therefore, this observation agrees qualitatively with the $\Delta\lambda_0$ achieved by reducing the bending radius. In addition, the profile of point A ($r_c = 1.7$ μm) also matches $\lambda_0(R_b = \infty) = 1546.48$ nm and by reducing r_c from this point, λ_0 is shifted to shorter wavelengths. Surprisingly, by simulating the effect of bending in the profile of point A, λ_0 is also shifted to shorter wavelengths. This is another interesting observation, since other studies that have analyzed the effect of bending on λ_0 in optical fibers [108, 109] and integrated waveguides [113] have only predicted that λ_0 can be shifted to longer wavelengths.

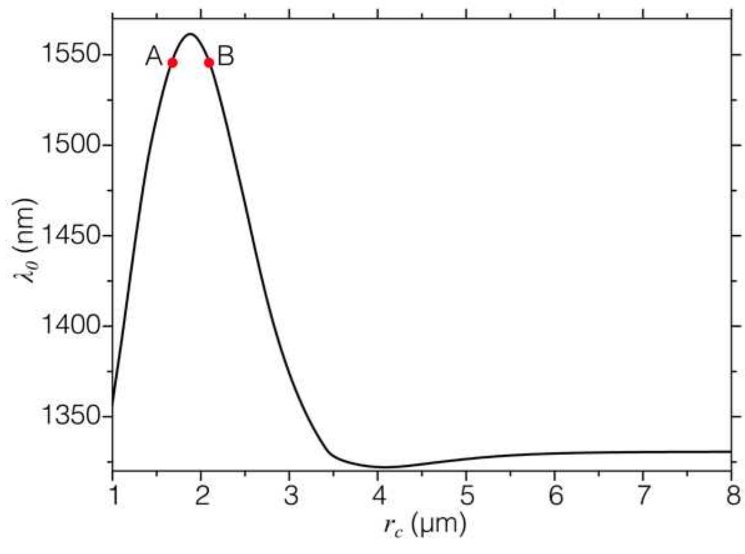

Figure 2.18: Zero dispersion wavelength as a function of the core radius. Other geometrical parameters were varied proportionally. Calculations performed by Dr. Jhonattan C. Ramirez.

2.3.3 Discussion

In this section we have experimentally and theoretically studied the effect of bending in the dispersive properties of an optical fiber, particularly, the bending-induced shift of λ_0 in a DSF. Even though the shift of λ_0 with bending was theoretically predicted for a single mode fiber in [108, 109], its accurate characterization has been limited due to the lack of methods capable of measuring short lengths of uniform fibers wound with a constant bending radius and a good accuracy on λ_0 [109]. Therefore, we have described the experimental challenges that we had to overcome in order to apply our FWM-based measuring method and be able to obtain a good control of the bending radius, guarantee the fiber uniformity, and achieve a good sensitivity in measuring changes of λ_0. That is, being able to measure a fiber as short as 20 m wound over cylinders with smooth surfaces, observing spectral characteristics of the FWM that correspond to the sinc^2 function predicted by theory in a uniform fiber(see Section 2.1), and measuring $\Delta\lambda_0$ as small as 40 pm (which corresponds to a variation of R_b from 10 to 8 cm).

Our results reveal that λ_0 is shifted up to 12 nm for an $R_b = 1$ cm, which represents a larger shift compared to that achieved from changes in other environmental variables such as temperature, pressure or strain [100]. This observation implies that for experiments in which maintaining a constant dispersion along the fibers is essential (for example, those based on phase-matched FWM), special care must be taken in the fiber bending radius. This becomes even more critical since, as observed in our results, bending-induced losses become noticeable only for tight bending radii (i.e., $R_b = 1$ cm), whereas the bending-induced $\Delta\lambda_0$ can be detectable even for a large bending radius (i.e., $R_b = 8$ cm).

Even though the mode deformation induced by bending (observed in our calculations) has been studied for single-mode [118] and multimode [110, 120, 111] optical fibers, it has not been related with changes of fiber dispersion. However, in the context of silicon waveguides, a theoretical study in [113] has calculated that λ_0 increases to longer wavelengths as the bending radius is reduced and has attributed this shift to two different effects: (i) the increase of anomalous dispersion due to the so-called "mode squeezing" and (ii) the increase of normal dispersion given by the amount of energy that surpasses the cladding. In contrast, the results obtained in our study show that λ_0 can be shifted to either shorter or longer wavelengths, depending on fiber geometry and mode confinement, and that there is a relationship between the observed shift of λ_0 induced by bending and that obtained by varying fiber geometry. Therefore, our results give insights for dispersion engineering of devices based on FWM and other nonlinear effects. For instance, bending could be used for tuning λ_0 to obtain parametric efficiency over an spectral region of interest [121]; for equalizing λ_0 along the fiber length and compensate fluctuations that arise from fabrication processes [122]; or for gradually varying $\lambda_0(z)$ and maintain the phase-matching along lossy waveguides [123]. All these approaches could be applied in optical fibers and also in other integrated bent-waveguide structures.

2.4 High-order Dispersion in Silicon Nano-Waveguides

Silicon on insulator (SOI) waveguides have become the main platform for integrated photonics, as a result of two essential reasons. First, the high compatibility with CMOS fabrication processes. Second, the tight optical-confinement due to the high refractive index contrast between silicon and silicon oxide. In particular, we refer to nano-waveguides as those having dimensions that allow single-mode operation and low propagation losses, being useful for several applications [124, 125, 13]. Given the large silicon nonlinear refractive index (i.e., $n_2 = 4.5 \times 10^{-18}$ m^2 W^{-1} [13, 126]) along with the tight optical-confinement, experimental demonstrations of nonlinear optical effects have been performed with relatively lower pumping power and shorter waveguide propagation lengths compared with realizations in optical fibers [23, 27, 55, 90, 127 – 137]. For instance, optical parametric amplification [23, 127, 130], wavelength-conversion [55, 27, 90, 128, 129], generation of frequency combs [135, 136, 137] and supercontinuum generation [131 – 134]. In most of these works, the dispersion of the nano-waveguides has been engineered in order to obtain specific characteristics, convenient for the enhancement of a particular nonlinear effect. Such dispersion engineering approaches consist in modifying the waveguide cross-section dimensions or cladding materials. However, it is well-known that the dispersive characteristics of silicon nano-waveguides are dominated by the tight-optical confinement rather than material dispersion, which leads to a larger dispersion compared to that of optical fibers (about three orders of magnitude) [74]. This applies not only for chromatic dispersion, but also for high-order dispersion as we will show later in this section.

Although some studies have characterized chromatic dispersion in silicon nano-waveguides by interferometric techniques [138, 75, 74], their measurements do not allow to obtain accurate information of HOD. Moreover, in experiments of FWM-based wavelength-conversion [90] and parametric amplification [130], in which fourth-order dispersion plays an important role, the simulated HOD parameters do not match the experimental observations. These disagreements have been attributed to the impossibility of simulating the actual geometry of the fabricated waveguides. Therefore, given the importance of dispersion parameters in nonlinear propagation phenomena, understanding the dispersive characteristics of silicon nano-waveguides and the development of characterization methods capable of accurately measuring HOD are fundamental for nonlinear optical applications in silicon photonics.

In this section, by means of numerical examples, we show the dispersion characteristics of silicon nano-waveguides and the possibilities of applying our dispersion characterization method based on FWM pumped by an incoherent-source. Moreover, in our calculations we neglect the effects of single-photon and two-photon absorption, and changes on the waveguide propagation losses and dispersion that could arise from the generation of free carriers. However, given the influence of these absorption mechanisms and subsequent free-carrier induced effects in the optical propagation characteristics of silicon-nano waveguides, in chapter 3 we have comprehensively studied and characterized dynamics of optically-generated free carriers.

2.4.1 Dispersion of the material and the nano-waveguide

In Figure 2.19(a) we show the calculated material dispersion curves for silicon (Si) and other silicon-based materials commonly used in integrated photonics such as silicon oxide (SiO_2) and silicon nitride (Si_3N_4). For these calculations we have obtained the refractive indices by means of Sellmeier models [103, 139, 140] and used the definition of the dispersion coefficient given by [141]:

$$D = -\frac{\lambda}{c}\frac{d^2n}{d\lambda^2}. \tag{2.20}$$

The second-order derivative ($d^2n/d\lambda^2$) was numerically calculated using finite-difference differentiation [119]. Note from Figure 2.19(a) that silicon material dispersion is normal ($D < 0$), whereas, for silicon nano-waveguides [illustrated in Figure 2.19(b)] becomes large and anomalous ($D > 0$) between 1300 and 1550 nm. This abrupt change on dispersion can be attributed to the tight optical-confinement in the nano-waveguide.

For the waveguide of cross-section 220 nm × 416 nm ($h \times w$) and SiO_2 cladding we found that $\lambda_0 \approx$ 1550 nm, desirable for optical parametric amplification at this spectral band, which is widely-used optical communications [23]. In addition, we have calculated the dispersion for waveguides with cross-sections of 220 nm × (416 $\pm$ 10) nm in order to illustrate the sensitivity of dispersion to changes in waveguide geometry. Comparing the dispersion curves of Figure 2.19(b) one can note that the second λ_0 (around 1550 nm) is more sensitive to variations of waveguide geometry compared with the first λ_0 (around 1300 nm). Moreover, it is worth noting that both the slope (at λ_0) and the curvature of the dispersion are also strongly affected by changes in waveguide geometry, which evidences the sensitivity of high-order dispersion.

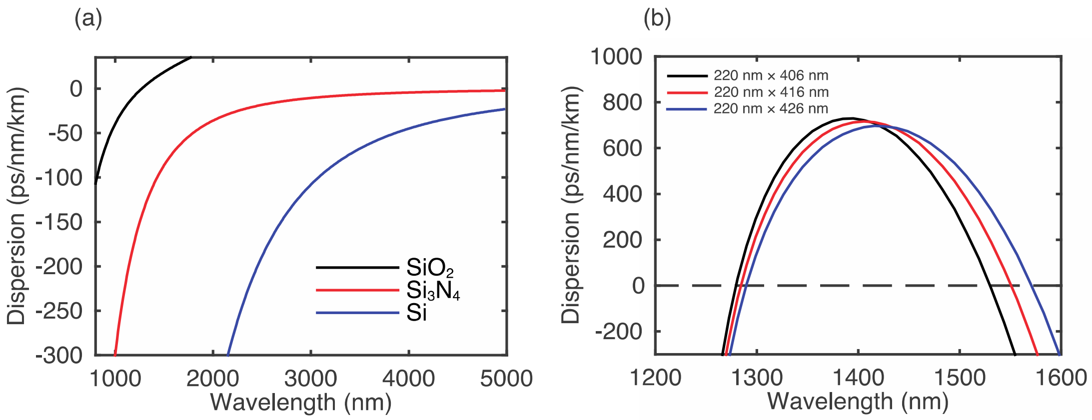

Figure 2.19: (a) Calculated dispersion of silicon-based materials commonly used in integrated photonics (SiO_2, Si_3N_4 and Si). (b) Calculated dispersion for silicon nano-waveguides with silica cladding and different cross-sections.

The dispersion curves presented in Figure 2.19(b) correspond to the quasi-TE fundamental mode and were obtained by evaluating $\beta(\omega)$ over a wide-range of frequencies (i.e., between 1000 and 2000 nm) and performing finite-difference differentiation. The propagation constant $\beta(\omega)$ was obtained via modal-analysis using the finite-element method and the waveguide dispersion coefficient was calculated as:

$$D = -\frac{2\pi c}{\lambda^2}\frac{d^2\beta(\omega)}{d\omega^2}. \tag{2.21}$$

For the waveguide with cross-section 220 nm × 416 nm we have also evaluated the β_n dispersion parameters up to the sixth-order for the two values of λ_0. The calculated waveguide dispersion parameters, summarized in Table 2.2, are at least two orders of magnitude larger than those of optical fibers, which is evidenced by the strong wavelength-dependency of the dispersion curves presented in Figure 2.19(b).

λ_0(nm)	β_3(ps^3/km)	β_4(ps^3/km)	β_5(ps^3/km)	β_6(ps^3/km)
1285.1	13.1	0.21	6.2×10^{-3}	2×10^{-4}
1550.5	−17.1	0.27	-2.9×10^{-3}	-2.4×10^{-5}

Table 2.2: Calculated dispersion parameters for the silicon nano-waveguide with cross-section 220 nm × 416 nm and silica cladding.

In the following subsection we will theoretically evaluate the possibility of applying our dispersion characterization method, which is based in measuring the power spectrum generated by FWM between an incoherent-pump and a laser, in the silicon nano-waveguide with cross-section 220 nm × 416 nm and silica cladding.

2.4.2 Prospects of high-order dispersion characterization in silicon nano-waveguides

Given the sensitivity of HOD to changes of nano-waveguide geometry and the limitations of common dispersion characterization techniques in obtaining accurate values of HOD, by using theoretical example, we want to show the possibilities and limitations of applying our dispersion characterization method in a silicon nano-waveguide.

From an experimental perspective there are two main aspects to be considered:

(i) The peak power of the generated FWM spectrum must be detectable by an OSA.

(ii) The spectral width of the FWM peak must be narrow-enough to accurately measure λ_{FWM}.

Regarding the power of the generated FWM, assuming the use of an OSA with a resolution bandwidth $\delta\omega$ and recalling the expression of Equation (2.6) for the power spectral density of the FWM field generated in an uniform-waveguide, the peak power at ω_{FWM} may be given as [96]:

$$P(\omega_{FWM}) \cong 2\left(\gamma P_p L\right)^2 P_\ell \left(\frac{\delta\omega}{\Delta\omega_p}\right). \tag{2.22}$$

Although this expression corresponds to a lossless waveguide, a simple and convenient way to take into account the effect of propagation losses consists in considering the waveguide effective length (L_{eff}) instead of the propagation length (L). Therefore, the propagation losses of silicon nano-waveguides (typically 1.4 dB/cm [142, 143]) impose a limit of few cm in L_{eff}. However, the high-nonlinearity of silicon nano-waveguides compensates the limited L_{eff}. By using the theoretical approach for the nonlinear coefficient in tight optical-confining waveguides presented in [71, 72], we have calculated $\gamma \approx 2 \times 10^5$ W^{-1} km^{-1}, that is 5 orders of magnitude larger than that of DSFs. Consequently, it is possible to apply our method in silicon nano-waveguides as long as few cm with similar power levels as those used in our experiments in optical fibers.

Regarding the width of the generated FWM spectrum, that according to the approximation of Equation (2.16) is inversely proportional to $L\beta_3(\omega_{FWM} - \omega_\ell)^2$, the effect of the short-waveguide length is compensated by the large value of β_3. Therefore, it is also possible to apply our method in silicon nano-waveguides by tuning the laser and measuring the FWM power spectrum over similar wavelengths as those used in our experimental examples in optical fibers.

In Figure 2.20(a) we present calculated FWM power spectra generated in the silicon nano-waveguide of cross-section 220 nm × 416 nm and silica cladding. For this calculation we have used Equation (2.5) and assumed power levels for the pump and laser of 100 and 10 mW respectively. In addition, for the calculation of $\Delta\beta(\omega)$ we have used the second $\lambda_0 = 1550.5$ nm and the β_n dispersion parameters up to the sixth-order presented in Table 2.2. We assumed an incoherent-pump of 40 nm bandwidth located near 1530 nm. Note from Figure 2.20(a) that, considering a resolution bandwidth of 100 pm, the peak power levels of the generated FWM spectra are around −20 dBm, which could be easily detectable by most commercial OSAs. In addition, the spectral width of the generated FWM is no larger than 10 nm within the evaluated wavelengths, which allows accurate measurements of λ_{FWM} as we have shown in Section 2.1.

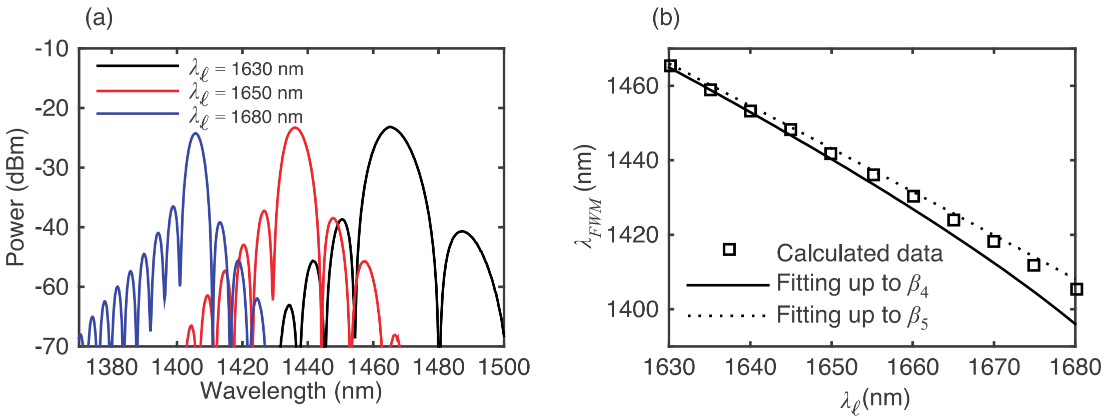

Figure 2.20: (a) Calculated FWM power spectra in the silicon nano-waveguide for different λ_ℓ, we have assumed a resolution bandwidth of 100 pm. (b) Calculated λ_{FWM} as a funciton of λ_ℓ along with the fitted expressions that take into account up to β_4 and β_5.

The calculated values of λ_{FWM} as a function of λ_ℓ are presented in Figure 2.20(b). In addition, we have included the evaluation of the fitting expression of Equation (2.11) which was derived considering the effect of β_4 in the phase-matching condition of the FWM process. It is worth noting that the evaluated expression does not match the calculated values of λ_{FWM} and this disagreement can be attributed to the influence of higher-order dispersion parameters. Therefore, we have also derived an expression, similar to Equation (2.11), although taking into account up to β_5 in the phase-matching condition of Equation (2.10). We have also included the evaluation of the derived expression in Figure 2.20(b) and show that considering β_5 we obtain a better agreement with the values of λ_{FWM} as a function of λ_ℓ. This is a consequence of the increased HOD parameters in silicon nano-waveguides and clearly evidences the importance of accurate HOD characterization for the development of nonlinear silicon-photonics applications.

2.4.3 Discussion

In this section we have shown, by means of a theoretical example, the possibilities of applying our dispersion characterization method in silicon nano-waveguides.

We have shown the dispersion characteristics of most common silicon-based materials used in integrated-photonics (SiO_2, Si_3N_4 and Si). By comparing silicon material dispersion with that of a silicon nano-waveguide with silica cladding, we have observed that the large anomalous dispersion that appears at telecommunications wavelengths for the nano-waveguide could be attributed to the tight-optical confinement. In addition, we found that the calculated HOD parameters in the nano-waveguide are at least two orders of magnitude larger than those of optical fibers, which is evidenced by the large wavelength-dependency of the dispersion curve (i.e., presenting two λ_0 within the range of 1200 to 1600 nm).

We have calculated the FWM power spectrum expected in a uniform silicon nano-waveguide with silica cladding and a cross-section of 220 nm $\times$ 416 nm. Although the propagation losses of the waveguide impose a limit of few cm on the effective length of the waveguide under test, the high nonlinear coefficient of the nano-waveguide (i.e., 5 orders of magnitude larger than that of DSFs) allows to apply our method with a reasonable pumping power (around 100 mW). In addition, the large values of HOD in the nano-waveguide also prevent the generation of a broad FWM spectrum that is expected for a short waveguide length.

We have not obtained a good agreement when comparing the calculated λ_{FWM} as a function of λ_ℓ with the fitting expression derived in Section 2.1. Considering that this fitting expression was derived taking into account up to the fourth-order dispersion in the phase-matching condition, we believe that higher-order dispersion terms have a significant influence in the FWM process. Therefore, we have derived an expression that considers up to the fifth-order dispersion in the phase-matching condition and good agreement with the calculated values of λ_{FWM} as a function of λ_{ℓ}.

Considering the presented examples, our dispersion characterization method seems to be potential tool for accurate HOD characterization in silicon nano-waveguides, which is fundamental for nonlinear optical propagation phenomena and applications in silicon photonics.

2.5 Conclusions

In conclusion, we have presented a diversity of experimental and theoretical examples of dispersion characterization (λ_0 and HOD) in optical waveguides by using our measuring method based on FWM pumped by an incoherent-source.

In long fibers we have experimentally demonstrated a dispersion-mapping version of our FWM-based measuring method, which is based in tuning the overlapping region between short optical pulses along the fiber. Previous dispersion-mapping experiments have ignored the effect of HOD. However, besides λ_0 we have been able to demonstrate high-order dispersion mapping in a DSF. Our dispersion maps along with numerical calculations of fiber dispersion reveal, for the first time, that λ_0 presents a comparatively smaller fluctuation than that of HOD in DSFs. In addition, in contrast to previous experiments based on FWM of short optical pulses, our dispersion maps reveal that the spatial resolution can be shorter than the overlapping region between pulses. This opens possibilities for exploring our method in shorter waveguides, for instance, in integrated-waveguide structures.

In short fibers we have presented the capabilities of our method for obtaining accurate measurements of λ_0 and HOD (up to the fifth-order dispersion), and assuring the uniformity of the tested optical fiber. This has allowed us to study the change of fiber dispersion properties induced by bending, which had been limited due to the lack of accurate dispersion characterization methods. Therefore, we have been able to detect small and large variations on λ_0 caused by bending the fiber with large and tight bending radii, respectively. In addition, our results along with numerical calculations of fiber dispersion allowed us to explain the observed shift in terms of changes of the mode confinement that could be, analogously, related with changes in fiber geometry. Our observations give insights of using bending for dispersion-engineering of nonlinear optical devices in optical fibers and other bent-waveguide structures.

In silicon nano-waveguides we have theoretically evaluated the possibilities of applying our dispersion-characterization method. Although the effective length of silicon nano-waveguides is limited to few cm, we have shown that the generated FWM power spectrum could be easily detected while using moderate pumping-power levels, which is explained by the nano-waveguide high nonlinear coefficient. In addition, we have shown that the dispersion of silicon nano-waveguides, dominated by the tight-optical confinement, is characterized by HOD parameters with larger magnitudes compared with those of optical fibers. Even though the large HOD leads to a reasonable spectral width of the generated FWM, the calculated results cannot be explained by considering up to the fourth-order dispersion in the phase-matching condition. Therefore, we have considered up to the fifth-order dispersion in the phase-matching condition of the FWM process and obtained a good agreement with our calculations. Although, a more complete study that includes single and two-photon absorption and the effects induced by the generated free carriers must be taken into account (effects that will be thoroughly studied in chapter 3), our presented calculations allow to consider our FWM-based method as a useful tool for HOD characterization in silicon nano-waveguides and other integrated waveguides.

3. Linear and Nonlinear Generation and Dynamics of Free Carriers in Silicon Nano-Waveguides at 1550 nm

Given the tight optical confinement and high nonlinearity of silicon nano-waveguides, nonlinear optical effects such as Four-Wave Mixing (FWM) [23, 55], Stimulated Raman Scattering (SRS) [56] and Stimulated Brillouin Scattering (SBS) [57, 58] have been demonstrated near the 1550 nm spectral band (commonly used in optical communications). However, it has been recognized that the efficiency of these nonlinear effects is mainly limited due to Free-Carrier Absorption (FCA) [144, 23, 13], considering the high carrier densities generated by two-photon absorption (TPA) in silicon nano-waveguides [142]. Therefore, most demonstrations have been feasible by means of using either low CW pump power [55], short optical pulses (with durations ranging from hundreds of femtoseconds to few picoseconds) [23], or the implementation of a reverse biased *p*-*i*-*n* junction across the waveguide [56].

Other nonlinear optical effects studies in silicon nano-waveguides, instead of minimizing the effect of FCA, have included FCA and/or the induced Free-Carrier Disperison (FCD) in the analysis of signal propagation, showing that free-carrier effects and their dynamics play and important role in novel nonlinear phenomena and applications [59 – 66, 145, 146]. For instance, studies of soliton physics and supercontinuum generation [66, 60], Self-Phase Modulation (SPM) [59], FWM-based phase-sensitive amplification [64], and nonlinear phenomena in plasmonic waveguides [65].

In addition, the consideration of free-carrier effects dynamics is crucial for time-resolved studies of nonlinear optical propagation in silicon micro-cavities [145, 146]. One common scenario in micro-cavities is the presence of opposite shifts of the resonance frequencies due to FCD (blue-shift) and self-heating (red-shift). The latter effect arises from the phonon-assisted recombination of generated carriers in silicon that leads to an increase in temperature and, consequently, to a change in the refractive index via the thermo-optic effect

[147]. The combination of nonlinear, free-carrier, and thermal effects leads, for example, to self-oscillation [145, 146]. Moreover, the dynamics of free-carriers plays also an important role in the development of novel all-optical devices based in silicon nano-waveguides and cavities that allow to control the flow of light in integrated photonic circuits, such as modulators [67] and diodes [68].

The dynamics of free-carrier involve the mechanisms that generate excess of electron-hole pairs and those by which they recombine. On the one hand, free carriers are generated when the absorption of photons with higher energy than the bandgap, promotes an electron from the valence band to the conduction band and creates a hole in the valence band. Given the silicon bandgap of $\sim$1.12 eV, the generation of free carriers through single-photon absorption (SPA) for wavelengths above 1100 nm is usually ignored. Thus, optical carrier generation in silicon nano-waveguides at 1550 nm has been mainly attributed to two-photon absorption (TPA). However, free-carrier generation through SPA may also occur via intra-bandgap states at photon energies lower than the band gap. These intra-bandgap states may be a consequence of impurities, bulk defects, or surface states at the Si/SiO_2 interface [148, 149, 150]. As it will be presented later in this chapter, even though SPA corresponds to a minimum amount in the total linear propagation loss of nano-waveguides (i.e., about 7% in our tested waveguide), the generated carrier density due to SPA is considerable for low and medium power regimes (i.e., below 300 mW) [142].

On the other hand, after generation, excess carriers may recombine via different processes: (i) radiative recombination, (ii) Auger recombination, or (iii) via flaw states that act as recombination centers between the bandgap. Considering that Silicon is an indirect-bandgap semiconductor, radiative recombination is usually neglected. Auger recombination can also be ignored since it becomes significant only for very high carrier densities (above 10^{18} cm^{-3} [151, 152]). Consequently, the dominant carrier recombination mechanism in silicon nano-waveguides is via flaw states that, besides recombination centers, could act also as carrier traps. In the case of nano-waveguides, there is a significant carrier-trapping and, as we will show in this chapter, corresponds to the underlying mechanism of the complex recombination dynamics observed in nano-waveguides [143].

In this chapter we present a detailed experimental and theoretical study on the dynamics of free-carriers generated by optical means in silicon strip (i.e., full-etched) nano-waveguides at the 1550 nm spectral band.

In the first part of this chapter (Section 3.1) we study the optical generation of free carriers considering SPA and TPA. We present a numerical modeling, based on a one-dimensional finite difference approximation, that describes the propagation of a short optical pulse along the waveguide and the simultaneous generation and recombination of free carriers. We also present the details of the pump and probe experimental setup, used to obtain time-resolved information of the carrier density averaged along the waveguide and the instantaneous carrier lifetime. In addition, we present a theoretical derivation of an expression for the generated average carrier density under low pumping power conditions. This expression was used to measure the SPA and TPA coefficients of our waveguide under test, by means of pump-and-probe experiments. Finally, we present our experimental and theoretical results of the generated carrier density that are in a good agreement with the measured absorption coefficients.

In the second part of this chapter (Section 3.2) we study the recombination of free carriers in silicon nano-waveguides. In this study we also perform pump-and-probe experiments and observe a nonlinear recombination dynamics. We first apply the carrier recombination and carrier trapping via flaw states to the particular case of nano-waveguides and explain the theoretical model used to evaluate the temporal decay dynamics of excess carriers in the presence of flaws. Afterwards, we compare our experimental observations with the theoretical results that present a qualitative good agreement and, therefore, explain the observed dynamics in terms of carrier-trapping. Finally, we present the possibilities to exploit the observed dynamics in all-optical switching applications.

3.1 Optical Linear and Nonlinear Absorption and Free-Carrier Generation in Silicon Nano-Waveguides

Although over the spectral band of 1550 nm SPA is usually ignored in the case of bulk silicon, different studies in nano-waveguides have demonstrated that SPA becomes non-negligible [148, 149, 150]. For instance, some of these studies have demonstrated the use of SPA in the development of novel devices such as waveguide detectors [149] and power monitors [150]. In addition, the study in [148] has identified that SPA arises from surface-states in large surface-to-volume ratio nano-waveguides. However, even if the effect of SPA has been characterized by measurements of photocurrent [149], capacitance [150], or optical attenuation [148] as a function of the CW input power, none of these studies has directly characterized the SPA coefficient as a result of two principal limitations:

(i) In order to estimate the SPA coefficient, a carrier lifetime must be assumed. However, the carrier lifetime in nano-waveguides is highly dependent on the temporal evolution of the carrier density due to carrier-trapping [143] and, therefore, it is not straightforward to assume a single carrier lifetime for CW pumping conditions.

(ii) A value for the TPA coefficient must also be assumed in order to identify the individual contributions of SPA and TPA in the generated carrier density. Even though the measured TPA coefficient has been reported for bulk silicon at 1550 nm (i.e., 0.4 – 1.2 cm/GW [153, 154, 155]), TPA may also be enhanced in optical tight confinement waveguides. In the case of strip nano-waveguides, widely used guiding structures due to its single-mode operation and low bending losses [124], the TPA enhancement has only been observed for mid-infrared wavelengths (i.e., above 1775 nm) [156]. Thus, the TPA coefficient must also be accurately characterized in order to measure the SPA coefficient for a particular of waveguide.

In this section we present how to measure simultaneously the instantaneous carrier lifetime, SPA and TPA coefficients. Our measuring method consists in time-resolved pump-and-probe experiments and the use of a derived analytical expression for the generated carrier density as a function of the pump power. In addition, we show how the measured SPA and TPA coefficients represent well the carrier generation and pump propagation as a function of the input pump power, observed in our experiments and simulated by numerical calculations.

3.1.1 Modeling of pulse propagation and carrier dynamics

The dynamics of free carriers is governed by generation and recombination processes that may be described by the following continuity equation:

$$\frac{\partial N(z,t)}{\partial t} = G(z,t) - \frac{N(z,t)}{\tau_c}, \tag{3.1}$$

where $N(z,t)$ is the carrier density, $G(z,t)$ is the carrier generation rate, $N(z,t)/\tau_c$ is the recombination rate and τ_c is the carrier lifetime. Considering that free carriers are generated optically via SPA and TPA and disregarding other carrier generation mechanisms, $G(z,t)$ may be given by:

$$G(z,t) = \frac{\alpha_{SPA}}{\hbar\omega} I(z,t) + \frac{\beta_{TPA}}{2\hbar\omega} I^2(z,t), \tag{3.2}$$

where α_{SPA} and β_{TPA} are the SPA and TPA coefficients, $\hbar\omega$ is the photon energy and $I(z,t)$ is the pump pulse intensity. In addition, the propagation of the pump pulse along the waveguide in the z direction is given by [64]:

$$\frac{\partial I(z,t)}{\partial z} = -[\alpha + S\sigma_r \eta N(z,t) + \beta_{TPA} I(z,t)] I(z,t), \tag{3.3}$$

where α is the linear attenuation coefficient that considers scattering as well as SPA losses (i.e. $\alpha = \alpha' + \alpha_{SPA}$). The second term accounts for free-carrier absorption (FCA) where σ_r is the FCA cross-section for bulk-silicon and S is the slow-light factor that considers the reduction of the group velocity in the waveguide compared with that of bulk silicon [62, 157]. The factor η takes into account the overlap between the optical mode and the silicon core assuming that the carriers are uniformly distributed throughout the core due to the fast diffusion time, which is approximately 10 ps for our waveguide under test [143]. For other nano-waveguide structures, for example rib waveguides, the diffusion of carriers over a larger area would cause a reduction of the carrier density that overlaps the optical mode.

On the other hand, considering the use of a probe signal that is much weaker than the pump (i.e., in our work has been kept at least two orders of magnitude weaker), the propagation for the probe signal intensity $I_s(z,t)$ can also be described as [62]:

$$\frac{\partial I_s(z,t)}{\partial z} = -[\alpha + S\sigma_r \eta N(z,t) + 2\beta_{TPA} I(z,t)] I_s(z,t), \tag{3.4}$$

Here we have assumed that the pump causes significant attenuation on the probe via non-degenerate TPA but not the other way around.

In order to solve the propagation of an optical pump pulse along the waveguide, we integrate Equation (3.3) and obtain a similar expression as the one presented in [62], given by:

$$I(z,t) = I(0,t)e^{-\alpha z} e^{-S\sigma_\alpha \int_0^z N(z',t)dz'} e^{-\beta_{TPA} \int_0^z I(z',t)dz'}, \tag{3.5}$$

where the different exponential terms consider linear attenuation, FCA and TPA. In addition, in order to solve the simultaneous optical generation of free-carriers due to SPA and TPA, and their recombination, we assume that Equation (3.1) has a solution of the form $N = N' e^{-t/\tau_c}$ and obtain the following expression (also similar to the one presented in [62]):

$$N(z,t) = e^{-\frac{t}{\tau_c}} \int_{-\infty}^{t} G(z,t') e^{\frac{t'}{\tau_c}} dt'. \tag{3.6}$$

In this assumption carriers recombine with a single τ_c, which is valid for a short time after the pump pulse (i.e. few hundred ps for these particular waveguides [143]). However, as we will show in section 3.2, for later stages of recombination τ_c shows a significant dependency on carrier density as a consequence of carrier trapping by flaws.

Solving numerically Equations (3.5) and (3.6) by means of a one-dimensional finite difference approximation, we are able to model the propagation of the pump pulse while evaluating the attenuation caused by linear losses, TPA and FCA, as well as the quantification of the carrier density generated by the pump. An example of our modeling is illustrated in Figure 3.1 for a Gaussian pulse of full-width at half maximum duration of τ_{FWHM} = 80 ps of and 100 mW of peak power. The left axis of Figure 3.1 shows the pulse at the input of the waveguide, whereas the right axis shows the generated carrier density for a silicon nano-waveguide of 2.4 mm of length. We have presented the generated carrier density for the first and last segments of the waveguide (i.e. z = 0.01 and 2.4 mm), as well as the longitudinally averaged carrier density. There are two important observations from Figure 3.1. First, it is worth noting that the longitudinal average of the generated carrier density does not depart significantly from the initial and final carrier densities for this short waveguide. This is an important observation, since our pump-and-probe experiments, performed over waveguides of few mm of length, just allows us to measure the longitudinal average of the carrier density. Second, note also that approximately 100 ps after the peak of the pump pulse, most carriers have been generated and, at the same time, no significant recombination has taken place. This is also an important remark, since it is used in our proposed approach to measure α_{SPA} and β_{TPA}.

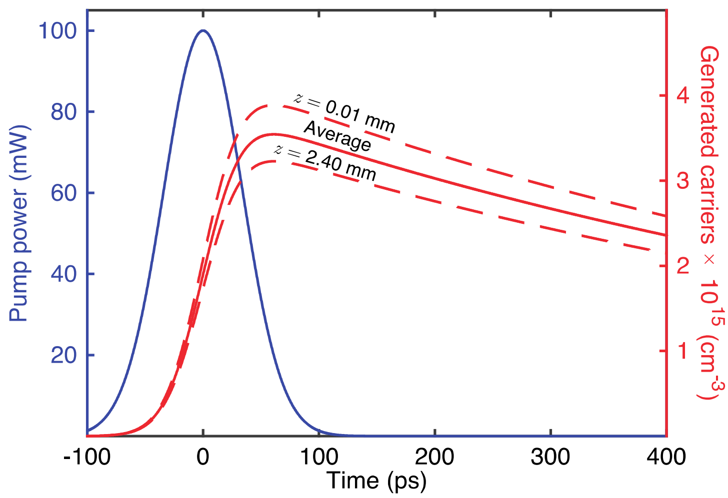

Figure 3.1: Numerical modeling of pulse propagation and carrier generation in silicon nano-waveguides. Pump pulses at the input of the waveguide (left axis) and generated carrier density (right axis).

Another interesting numerical study consists in the evaluation of the pump power depletion due to FCA. This analysis is of particular importance, since it is highly-dependent on the pulse duration, and may be explained by observing Figure 3.1 and noting that it takes some time until a significant carrier-density is achieved. Therefore, the pulse width can be changed to either reduce FCA pump-depletion or achieve higher carrier densities. In Figure 3.2 we show the calculated pulse peak power at the output of the waveguide as a function of that at the input. We have performed calculations for the same pulse of Figure 3.1 (i.e. τ_{FWHM} = 80 ps) and compared the case that considers all attenuation mechanisms (i.e., linear losses, TPA and FCA), with the one that ignores FCA pump depletion. We have also included the calculation of pulses of τ_{FWHM} = 40 and 10 ps, in both cases considering FCA pump depletion. Note that as the pulse width is reduced, there is an evident reduction of the effect of pump depletion due to FCA. It is important to point out that we have not evaluated even shorter pulses due to the fact that our model neglects the effect of dispersion, considering that the dispersion length ($L_D = \tau_{FWHM}^2/|\beta_2|$, about 100 m for a pulse of τ_{FWHM} = 10 ps in our tested waveguides) is longer than the length of the waveguide [64, 62].

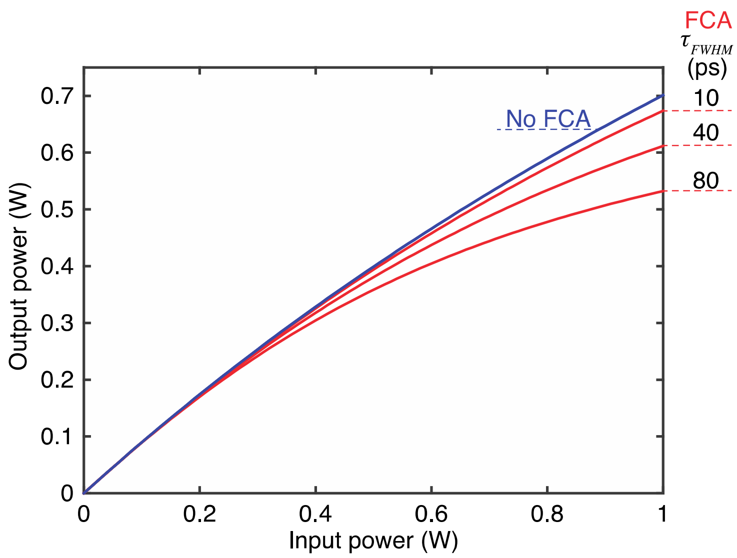

Figure 3.2: Numerical modeling of the output peak power vs. input peak power with and without considering FCA.

The fact that the effect of pump depletion due to FCA is negligible for ultrashort pulses (i.e., from hundreds of fs to few ps pulse duration) is useful, for example, in measuring β_{TPA} in waveguides, since a simple analytical expression for the pump intensity is derived in this regime, and β_{TPA} can be obtained by fitting the pump transmittance as a function of the input peak power [138, 158, 156]. However, in the absence of ultrashort pulse sources one must use a precise model that considers carrier generation and, thus, FCA-induced pump depletion.

In addition, by using pulses with tens of picoseconds duration and taking into account the generation of free carriers, allows one to obtain accurate measurements of important parameters for a particular waveguide such as α_{SPA}, β_{TPA} and τ_c as it is shown in this chapter.

Table 3.1 summarizes all simulation parameters used for the modeling used in Figure 3.1 and Figure 3.2.

Simulation parameter	Value
Waveguide length (L)	2.4 mm
Effective Area (A_{eff})	0.11 μm^2
Carrier lifetime (τ_c)	800 ps
Linear attenuation coefficient (α)	1.4 dB/cm
Single photon absorption coefficient (α_{SPA})	1.9 m^{-1}
Two photon absorption coefficient (β_{TPA})	1.5 cm/GW
Slow light enhancement factor (S)	1.19
Free-carrier absorption cross section (σ_r)	1.45×10^{-17} cm^2
Overlap between optical mode and core (η)	0.77
Pump wavelength (λ)	1547 nm

Table 3.1: Summary of parameters used for the numerical calculation of pulse propagation and carrier generation.

3.1.2 Pump and probe experimental setup

The pump and probe experimental setup that we have configured and used to perform the measurements presented in this chapter is described in Figure 3.3. This setup is subdivided in different stages such as the pump pulse, CW probe, waveguide under test, and detection.

For the pump pulse, a CW laser tuned at 1547 nm was modulated by an electro-optic Mach-Zehnder modulator (MZM, *iXblue MXER-LN-20*) with extinction ratio > 30 dB and 20 GHz bandwidth. The modulator was driven by an RF electrical pulse train of 500 kHz repetition rate (i.e. 2 μs period) and τ_{FWHM} = 80 ps (the pulse width could be actually varied from 80 ps up to the pulse train period). The RF pulse train was obtained from a pulse pattern generator (PPG1, *Agilent 81142A*), and passed through an RF amplifier in order to obtain enough RF voltage and maximize the extinction ratio of the optical pulses. The optical pulse train of approximately 3 mW peak power was amplified by an EDFA (*Keopsys Pulsed Erbium Fiber Amplifier*), obtaining ~40 W of peak power (> 40 dB gain). Although the low repetition rate was selected to minimize carrier accumulation effects between pulses, we have taken two additional experimental precautions. First, an optical bandpass filter (BPF1, *OZ Optics Manually Adjustable Tunable Filters*) was used after the EDFA to suppress out-of-band ASE. Second, an acousto-optic modulator (AOM, *Gooch&Housego T-M200*) of > 50 dB extinction ratio was used to minimize any residual CW optical power between pulses. The AOM was driven by an RF pulse train of 20 ns width, generated by a second pulse pattern generator (PPG2, *Agilent 81160A*). PPG2 was triggered by PPG1 (represented by the discontinuous line in Figure 3.3), thus both had the same repetition rate. A variable optical attenuator (VOA1, *JDSU mVOA-A2*) was used to control the pump power, allowing to maintain the same operating conditions of the EDFA over all measurements. A polarization controller (PC1) was used to minimize optical losses of the waveguide under test, assuring the coupling of the quasi-TE fundamental mode in the strip silicon nano-waveguide. Finally, a fiber coupler was used to derive 1% of the power to monitor the pump pulse shape and peak power by means of an external 20 GHz photodetector (*Picometrix DG-15xr*) and an electrical input (Ch2) of a wide-bandwidth oscilloscope (*Infiniium DCA-J Agilent 86100C*).

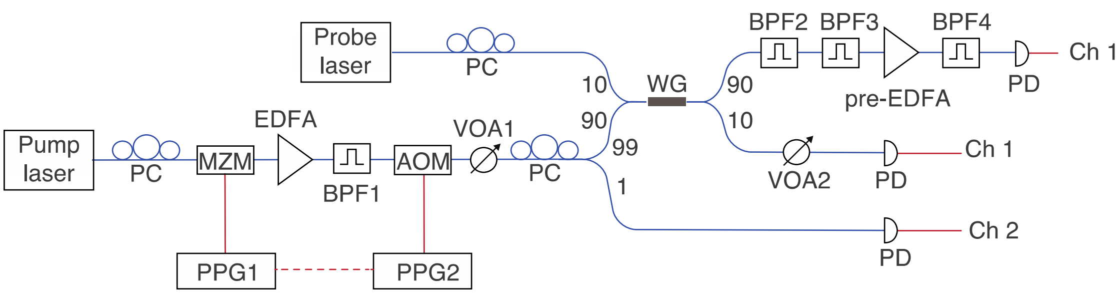

Figure 3.3: Pump and probe experimental setup.

The probe was derived from a second CW laser tuned at 1549 nm, and a polarization controller (PC2) was also used to warrant the coupling of the quasi-TE fundamental mode in the waveguide under test. In addition, we kept the power of the probe around 50 μW (power coupled into the waveguide) to minimize the effect of carriers generated by the probe. A fiber coupler was used to combine 90% of the pump and 10% of the probe before the waveguide under test. The optical spectrum of both combined signals is shown in Figure 3.4(a). The selection of the wavelengths of the pump and the probe was based on two reasons. First, the spectral response of the grating couplers used for coupling light in and out the waveguide under test exhibit maximum transmittance around these wavelengths. Second, the separation of 2 nm was enough to separate both pump and probe before detection, by means of optical filtering.

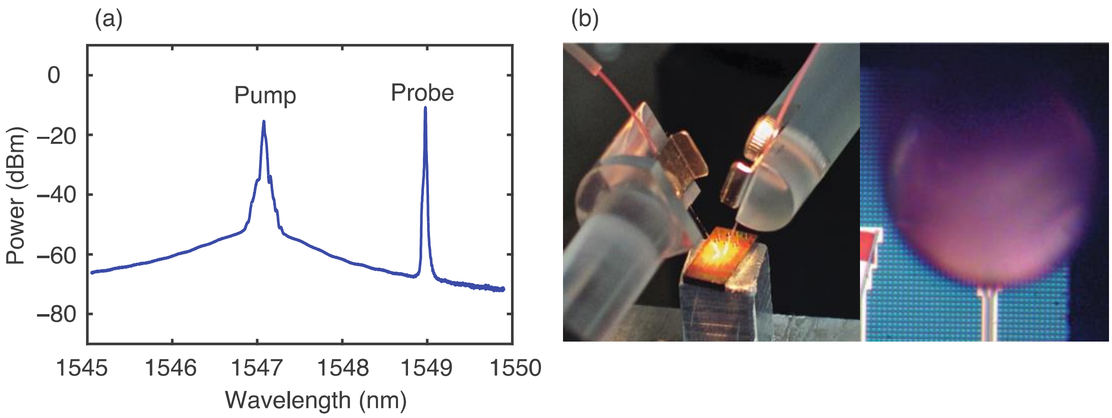

Figure 3.4: (a) Optical power spectrum before the waveguide under test (resolution bandwidth of 10 pm). (b) Light coupling in and out the waveguide through grating couplers.

The waveguide under test was a silicon strip nano-waveguide of 220 nm × 450 nm cross-section and 2.4 mm of length. The waveguide had silicon oxide cladding and was fabricated at a CMOS foundry (IMEC/Europractice) by means of optical lithography and inductively-coupled plasma reactive ion etching (ICP-RIE). As it was mentioned, the light was coupled from a cleaved fiber to the waveguide by means of grating couplers as shown in Figure 3.4(b). We used two additional waveguides of different lengths (i.e. 5.9 and 30 mm) to measure coupling and propagation losses by linear regression, and obtained a propagation loss of 1.4 dB/cm and 3.7 dB for the coupling loss between the grating and the cleaved fiber.

For the detection stage, a 10-90 fiber coupler was used at the output of the waveguide under test. 10% of the power was derived to measure the power and shape of the pump pulses, by means of an optical input (Ch1) of the wide-bandwidth oscilloscope, which has a built-in photodetector of 28 GHz bandwidth. A variable optical attenuator (VOA2, *Anritsu MN9610B*) was used to prevent saturation of the photodetector in the case of high pumping power. The additional 90% of the power was used for the detection of the probe. Two optical bandpass filters (BPF2 and BPF3, *Yenista XTM-50* and *Santec OTF-950* respectively) with > 40 dB out-of-band rejection were used to suppress the pump. Due to the high insertion losses of BPF2 and BPF3 (around 5 dB each), a low noise pre-EDFA (*IPG Photonics*) was used to amplify the probe. Finally, an additional bandpass filter (BPF4, *Yenista WSM-160*) was used to reduce out-of-band ASE resulting from pre-EDFA, thus increasing the signal to noise ratio (SNR) of the probe before detection as it is shown in Figure 3.5(a). Ch1 was switched to measure both the probe power and the output pulses.

Our interest is to identify the effect of the carriers generated by SPA and TPA via the FCA evidenced by the probe. Thus, by calculating the ratio between the detected probe power in the absence of the pump (pump off) and the probe power in the presence of the pump (pump on), we were able to obtain the normalized transmittance $T(t)$. Therefore, the normalized transmittance accounts for non-degenerate TPA and FCA and excludes linear losses. Several samples of the normalized transmittance were averaged to the reduce the high-frequency noise of the wideband of the photodetector. The number of averaged traces depended on the pump power, for instance, 75 traces were captured for the pump peak power of 10 mW, whereas only 5 traces were needed for the pump peak power of 1 W. We have also verified that the pump power did not vary significantly while capturing the traces. Figure 3.5(b) shows the normalized transmittance for different pump pulse peak power (P_0) coupled at the input of the waveguide (i.e. P_0= 100, 360 and 670 mW).

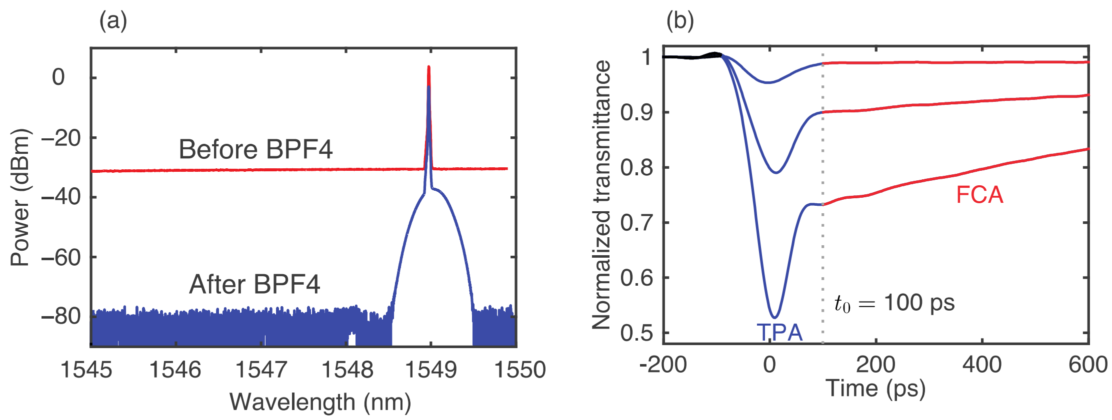

Figure 3.5: (a) Optical power spectrum before and after BPF4 (resolution bandwidth of 10 pm). (b) Normalized transmittance of the probe for different input power levels, $P_0 = 100$, 360 and 670 mW.

Note that two regions may be identified from Figure 3.5(b), an initial region dominated by non-degenerate TPA that shows an initial rapid decay of the normalized transmittance, and a following region dominated by FCA that shows a slow increase in the normalize transmittance as a result of carrier recombination. As we have shown in our numerical examples in previous sections, at a time t_0= 100 ps after the peak of the pump pulse, the generated carrier density has achieved its maximum and no significant amount of carriers have recombined, considering the measured instantaneous carrier lifetime at the beginning of the recombination is τ_c= 800 ps [143].

By neglecting the third term in Equation (3.4) and integrating along the waveguide of length L (i.e., from $z = 0$ to $z = L$), it is possible to derive the following expression for the normalized transmittance:

$$T(t) = \frac{I_s(L,t)}{I_s(0,t)\mathrm{e}^{(-\alpha L)}} = e^{[-S\sigma_r \eta L \bar{N}(t)]}, \tag{3.7}$$

where the longitudinally averaged carrier density has been defined as $\bar{N}(t) \equiv L^{-1}\int_0^L N(z,t)dz$ in [159]. Thus, it is quite straightforward to obtain an expression for the measured average carrier density $\bar{N}$ at t_0 given by [142]:

$$\bar{N}(t_0) = -\frac{\ln[T(t_0)]}{S\sigma_r \eta L}. \tag{3.8}$$

We have used the same set of parameters considered in our numerical calculations of σ_r = 1.45 × 10^−17^ cm² as reported for bulk silicon at 1550 nm [61, 160]. We have calculated a value of S = 1.19 and η = 0.77 for our waveguide under test. In Figure 3.6 we present the measured average carrier density as a function of input power, P_0.

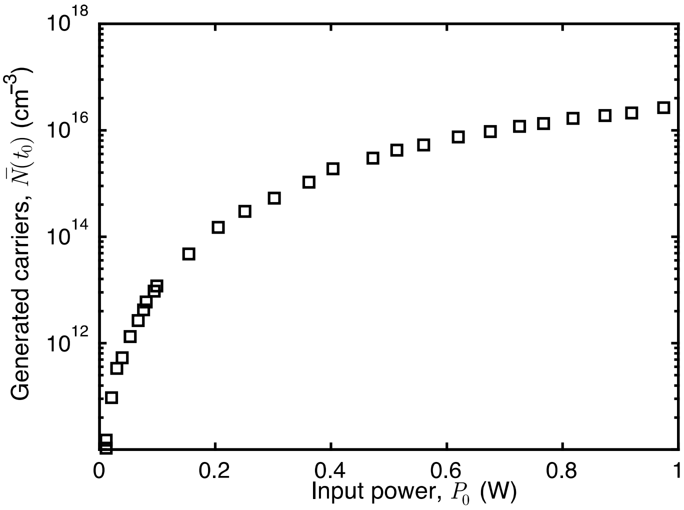

Figure 3.6: measured average carrier density $\bar{N}(t_0)$ as a function of the pump pulse peak power P_0.

Note from Figure 3.6 that the carrier density increases rapidly for low pump power (i.e. below 200 mW) as a result of carrier generation via SPA and TPA in the waveguide. In contrast, for higher pump power there is an evident reduction in the rate at which carrier density grows, which could be attributed to the fact that the pump is being depleted due to FCA at high carrier densities. Therefore, if FCA pump depletion could be neglected for low pump power, it would be easier to derive an analytical expression for the average carrier density as a function of the pump power, in terms of the linear and nonlinear absorption coefficients α_{SPA} and β_{TPA}. In the next section we will show such derivation, as well as the use of the resultant expressions in the measurement of α_{SPA} and β_{TPA} for our waveguide under test.

3.1.3 Measurement of the linear and nonlinear absorption coefficients in silicon nano-waveguides

For relatively low power levels, the FCA term in Equation (3.3) may be neglected. Thus, the propagation of the pump intensity propagation along the waveguide is now given by:

$$\frac{\partial I(z,t)}{\partial z} = -[\alpha + \beta_{TPA} I(z,t)] I(z,t). \tag{3.9}$$

Then, by integrating Equation (3.9), an analytical expression can be obtained for the pump intensity [64, 62, 59]:

$$I(z,t) = \frac{I(0,t) e^{-\alpha z}}{1 + \beta_{TPA} I(0,t) L_{eff}}, \tag{3.10}$$

where $I(0,t)$ is the pump intensity at the input of the waveguide and $L_{eff} = (1 - e^{-\alpha z})/\alpha$ is the effective length.

Considering that our measurements correspond to the longitudinal average of the carrier density and using Equations (3.2) and (3.6) we arrive to an expression of the form:

$$\bar{N} = e^{-\frac{t}{\tau_c}} \int_{-\infty}^{t} \left[\frac{\alpha_{SPA}}{\hbar\omega} \bar{I}(t') + \frac{\beta_{TPA}}{2\hbar\omega} \overline{I^2}(t') \right] e^{\frac{t'}{\tau_c}} \, dt', \tag{3.11}$$

where $\bar{I}(t) = L^{-1} \int_0^L I(z,t) dz$ and $\overline{I^2}(t) = L^{-1} \int_0^L I^2(z,t) dz$ are the spatial average of the pump intensity and squared intensity, respectively. By using the analytical expression for the pump intensity of Equation (3.10), that is obtained ignoring FCA pump depletion, $\bar{I}(t)$ and $\overline{I^2}(t)$ can also be solved analytically leading to:

$$\begin{gathered} \bar{I}(t) = I(0,t) \frac{L_{eff}}{L} \left[1 - \frac{\beta_{TPA} I(0,t) L_{eff}}{2} \right], \\ \overline{I^2}(t) = I^2(0,t) \frac{L_{eff,2}}{L}, \end{gathered} \tag{3.12}$$

where $L_{eff,2} = (1 - e^{-2\alpha z})/(2\alpha)$ stands for the effective length of the squared intensity. In the derivation of Equation (3.12) we have just assumed terms up to the second order in the pump intensity $I(z,t)$, we will show later that this is valid for relatively low pump power (i.e. below 100 mW).

The extra time integral in Equation (3.11) can be also solved analytically assuming a Gaussian pulse excitation at the input of the waveguide under test, which is defined as:

$$I(0,t) = I_0 e^{-\frac{t^2}{2\sigma^2}}, \tag{3.13}$$

where I_0 is the peak intensity of the pump pulse and σ is related to the pulse duration as $t_{FWHM} = 2\sigma\sqrt{2\ln(2)}$. As discussed earlier in this chapter, considering that the carrier density is measured at $t = t_0$, the evaluation of the implicit time convolutions for $I(0,t)$ and $I^2(0,t)$ that result from replacing Equations (3.12) and (3.13) in Equation (3.11), allows to represent the pump intensity and squared intensity as the products $I_0\tau_1$ and $I_0^2\tau_2$, where the time constants $\tau_n[n = 1,2]$ may be evaluated by using following approximation:

$$\tau_n = \frac{1}{2}\int_{-\infty}^{t_0} e^{-\frac{nt^2}{2\sigma^2}} e^{\frac{t}{\tau_c}} dt \approx \int_{-\infty}^{0} e^{-\frac{nt^2}{2\sigma^2}} e^{\frac{t}{\tau_c}} dt. \tag{3.14}$$

Finally, considering Equations (3.11) – (3.14) we present an expression for $\overline{N}(t_0)$ as a function of P_0 given by:

$$\begin{gathered} \frac{\overline{N}(t_0)}{P_0} = a + bP_0, \\ a = \frac{2\alpha_{SPA}\tau_1}{\hbar\omega A_{eff}}\frac{L_{eff}}{L}e^{-\frac{t_0}{\tau_c}}, \\ b = \frac{\beta_{TPA}\tau_2}{\hbar\omega A_{eff}^2}\left(\frac{L_{eff,2}}{L} - \frac{\alpha_{SPA}L_{eff}^2}{L}\right)e^{-\frac{t_0}{\tau_c}}. \end{gathered} \tag{3.15}$$

We have intentionally presented Equation (3.15) as a linear expression for two reasons. First, both SPA and TPA coefficients may be retrieved from a simple linear fitting of the measured data. Second, the presence of SPA in a particular waveguide is clearly evidenced if the results of the fitting present a non-zero intercept. In Figure 3.7 we present the measured carrier density to peak power ratio, $\overline{N}(t_0)/P_0$, as a function of the input power for our waveguide under test for relatively low power (i.e. P_0 = 10 to 100 mW). Note that our measurements show a clearly linear dependence of $\overline{N}(t_0)/P_0$ with P_0, and also present a non-zero intercept. This means that our analytical approach is valid for such power range and that our waveguide under test presents SPA. However, for higher P_0 we observed that our measurements depart from the linear dependence, which represents that FCA pump depletion must be considered for higher P_0. By performing a linear fitting of our measurements and using the relations of the fitted coefficients a and b with SPA and TPA coefficients given in Equation (3.15), we have obtained the measured coefficients α_{SPA} = 1.9 $\pm$ 0.1 m^{-1} and β_{TPA} = 1.5 $\pm$ 0.1 cm/GW for our waveguide under test.

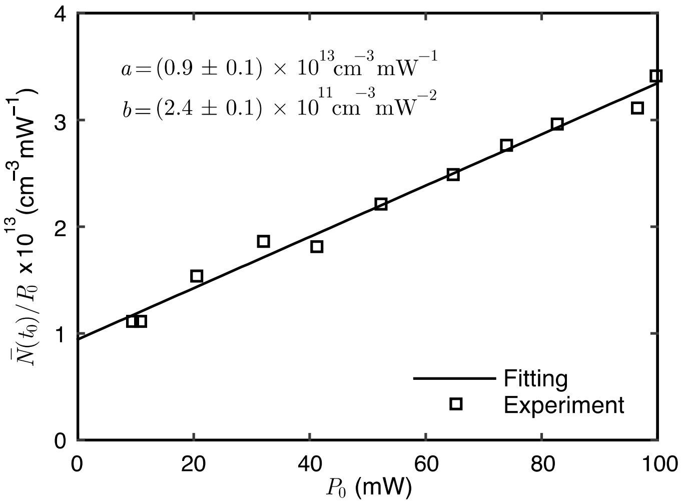

Figure 3.7: Carrier density to input pulse peak power ratio for peak power levels up to 100 mW. The straight line represents the linear performed linear fitting to retrieve the absorption coefficients of our waveguide under test.

3.1.4 Comparison of experiments with simulations

We compare in Figure 3.8 our measurements of the averaged carrier density for a wide range of power (i.e., 10 mW to 1 W) with the simulated results obtained from our numerical model, that considers FCA pump depletion. The results of Figure 3.8 have been presented in logarithmic scale for both axes in order to ease the visualization of the low-power and high-power regimes. The good agreement of the simulation with our experiments is a good evidence of the validity of our measured absorption coefficients, α_{SPA} = 1.9 $\pm$ 0.1 m^{-1} (equivalent to linear loss of ~0.1 dB/cm) and β_{TPA} = 1.5 $\pm$ 0.1 cm/GW, as these values have been used in our calculations as well as the measured τ_c= 800 ps [143]. In addition, our numerical model allows us to identify the individual contribution of each carrier generation mechanism. Thus, we have recognized three different regions delimited by vertical lines in

Figure 3.8. The region below ~5 mW is evidently dominated by SPA, whereas the region above ~300 mW is dominated by TPA. For the region in between, one may note that both carrier generation mechanisms have significant contributions and, therefore, should be considered.

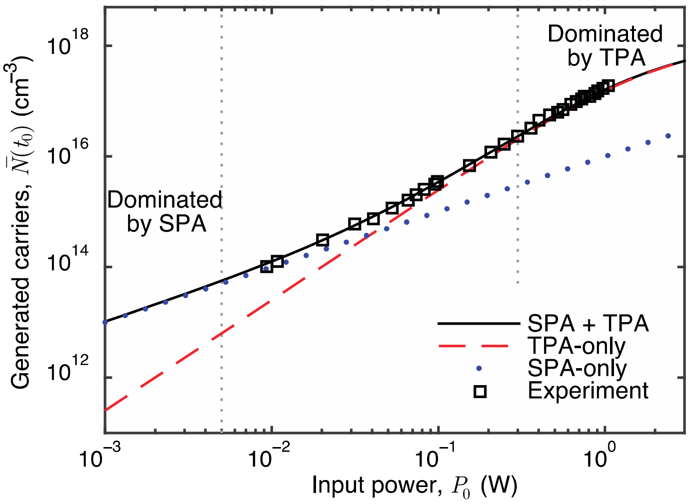

Figure 3.8: Comparison between the measured and simulated carrier density as a function of the input peak power. Individual contributions of the generation of free carriers via SPA only and TPA only.

One important observations from our results is that the measured β_{TPA} coefficient for the waveguide under test is higher than the measured value for bulk silicon at 1550, which has been reported by different groups, and their measurements (including the reported uncertainties) are within the range of 0.4 – 1.2 cm/GW [153, 154, 155]. Therefore, in order to validate the measured β_{TPA} for our waveguide under test, we have performed additional measurements of the pump pulse peak power at the output of the waveguide (before the grating coupler) as a function of that at the input (coupled into the waveguide). These measurements are presented in Figure 3.9 in conjunction with simulated results also obtained from our numerical model. We have also performed measurements in both coupling directions (forward and backward) to verify the balance in the coupling losses, which is validated given the good agreement between the data in both coupling directions. Note also that the good agreement of our simulations with our measured data also validates the measured absorption coefficients.

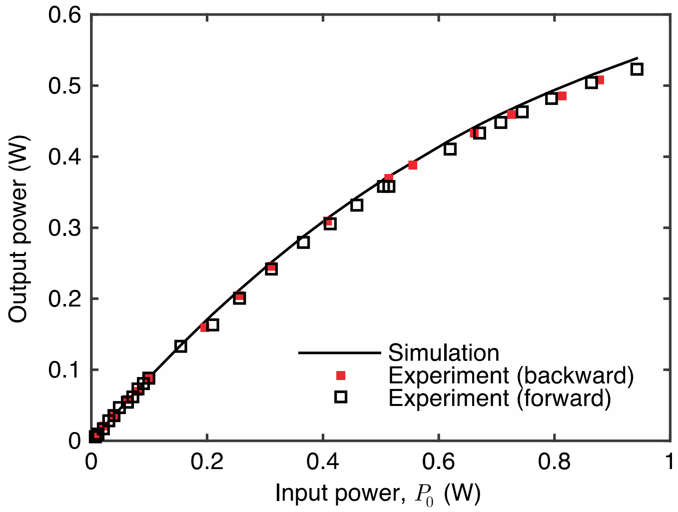

Figure 3.9: Comparison between measured and simulated pump peak power at the output of the waveguide as a funciton of the input peak power. The measurements were performed in both forward and backward coupling directions (forward and backward).

3.1.5 Discussion

In this section we have presented a thorough theoretical and experimental description of optical linear and nonlinear absorption mechanisms in silicon nano-waveguides at the spectral band around 1550 nm, as well as their contribution in carrier generation. Our pump-and-probe experiments along with developed analytical expressions allow to simultaneously measure the SPA and TPA coefficients and the instantaneous carrier life-time. Such comprehensive characterization, to the best of our knowledge, has not been presented before.

The measured SPA coefficient α_{SPA} = 1.9 $\pm$ 0.1 m^{-1} corresponds to approximately a 7% of the total linear propagation loss in our waveguides (~1.4 dB/cm). However, we have shown that its contribution to carrier generation is non-negligible and must be considered for a low and mid-range input power (below 300 mW). Even though, the measured SPA coefficient corresponds to the particular waveguide under test, considering that strip silicon waveguides of 220 nm × 450 nm cross-section are widely used and that our waveguide was fabricated at a CMOS foundry, that uses well-stablished processing methods, our results could be applied to similar waveguides. Moreover, our presented method can be used by other groups to test their samples and fabrication processes.

In regards to the TPA coefficient, its value has been characterized in different silicon wave-guiding structures that can be classified in three types [138, 161, 158, 62, 162, 156]:

(i) Waveguides with larger cross-section area than our tested nano-waveguide [138, 161, 158], which present measured TPA coefficients comparable with the values reported for bulk.

(ii) Photonic crystal waveguides that exhibit a significantly lower group velocity compared with bulk silicon [62, 162]. This reduction in the group velocity leads to the well-known slow-light enhancement of nonlinear optical effects [157] that, along with the optical tight confinement, have shown a significant enhancement of TPA compared with bulk.

(iii) Nano-waveguides with similar dimensions of our tested waveguide. In this case, only the study in [156] has reported measured values for the TPA coefficient and exhibit an enhancement compared with bulk. However, their measurements (performed at wavelengths longer than 1775 nm) do not allow to estimate the TPA coefficient at 1550 nm. Therefore, the measured β_{TPA} = 1.5 $\pm$ 0.1 cm/GW in our work is the first value reported for a silicon strip nano-waveguide at 1550 nm. In addition, by calculating the enhancement of the TPA coefficient that considers the reduction of the group velocity and the optical tight confinement [71, 72], the tested nano-waveguide results in a ≈20% enhancement compared with bulk. Considering this enhancement, our measurement is in agreement with the reported values for bulk silicon and larger cross-section waveguides (i.e., the top value within the range of 0.4 – 1.2 cm/GW).

Both the measured SPA and enhanced TPA lead to a large carrier density, even for low power applications. Given the importance of silicon strip nano-waveguides in several applications, most of them developed at the 1550 nm spectral band used for optical communications, our measurements and our proposed method are of great importance in the development of novel silicon photonic devices.

3.2 Nonlinear Carrier Recombination dynamics in Silicon Nano-Waveguides

Once excess carriers have been generated by means of a short optical pulse via SPA and TPA, the mechanisms of carrier diffusion and recombination start to modify the density of excess carriers that attenuate the optical probe through FCA. On the one hand, carriers diffuse spatially and rapidly become uniformly distributed over the waveguide cross-section. For instance, in the case of a silicon strip waveguide of 450 nm of width, we have calculated that takes about 5 ps for electrons and 15 ps for holes to diffuse until the carrier density reaches a uniform distribution over the waveguide cross-section [143]. On the other hand, we have already shown that for earlier stages the excess carriers recombine at an initial $\tau_c = 800$ ps. However, for later stages of recombination our experiments reveal that carriers do not recombine with a single carrier lifetime, but present a complex recombination dynamics that becomes slower as the carrier density is reduced. In order to illustrate this, we show in Figure 3.10(a) a sample of the normalized transmittance obtained by means of the same experimental setup described in Section 3.1.2, but in this case using a pulse of τ_{FWHM} = 130 ps and a 5.9 mm long silicon strip nano-waveguide of 220 nm × 450 nm cross-section and silica cladding. We also superimpose over the normalized transmittance of Figure 3.10(a) a fitting of the form $\exp[-A\exp(-t/\tau_c)]$ [58], where A is a constant and τ_c= 800 ps. Note that the exponential fitting matches just the initial stage of recombination, whereas there is an evident slower decay dynamics for later stages.

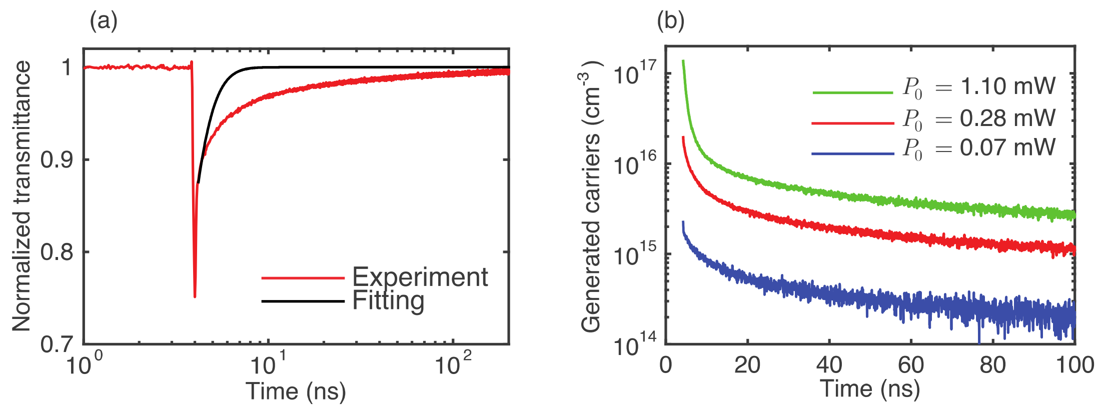

Figure 3.10: (a) Measured normalized transmittance and single lifetime fitting. (b) Measured averaged carrier density as a function of time for different pump power levels.

We also present our measurements of the average carrier density as a function of time in Figure 3.10(b) for different pump power levels, obtained from the normalized transmittance after the region dominated by non-degenerate TPA and using Equation (3.8). There are two important observations from our measurements in Figure 3.10(b): first, considering that the carrier density is presented in logarithmic scale, an exponential decay with a single lifetime would correspond to a straight line. In contrast, our results show a clear carrier lifetime dependency on the carrier density i.e., $\tau_c(N)$, in which there is a fast drop in the carrier density for higher densities and a slower dynamics for lower densities. Second, there is also a clear dependence of the decay dynamics on the initial pump power, which is evidenced by the different decay trajectories of the carrier density from a particular initial density (N_0). Our observations are qualitatively explained by the trap-assisted recombination that, although corresponds to a well-established process in semiconductors [163, 164] and has been applied in the context of solar cells [165], to the best of our knowledge, has not been explored in silicon photonics or other semiconductor photonic platforms.

3.2.1 Recombination via flaw states and carrier trapping in silicon nano-waveguides

In the optical generation of excess carriers via SPA and TPA in the nano-waveguide, electrons and holes are generated in equal amounts. Once generated, excess carriers recombine via states located within the gap that arise from permanent perturbations of the lattice, also known as flaws [163]. The term “flaw” was suggested in [166] and also adopted in [163] to generally describe all possible causes of lattice perturbations such as impurities and defects.

There are different ways by which carriers are recombined via flaws. For example, a flaw may capture an electron from the conduction band, and then transfer the electron to the valence band by capturing a hole [164]. However, besides acting as recombination centers between the bandgap, flaws may also act as temporary carrier traps. For example, the electron may be re-excited to the conduction band after being trapped in the flaw [163]. The role of flaws either as recombination centers or traps depends on the asymmetry between the capture cross-sections for electrons (σ_e) and holes (σ_h) and flaws energy levels [163] (which, will be explained in the next subsection 3.2.2). Particularly, significant trapping takes places for large density of flaws D_f, which implies that electrons or holes remain in the flaws long enough time and cause that the density of electrons in the conduction band (n_e) or holes in the valence band (p_e) decay at significantly different rates. This difference between the decay rates for electrons and holes results in a carrier imbalance (i.e., $p_e \neq n_e$), and therefore gives rise to a non-linear decay dynamics of the excess carrier density.

From our experiments, we are able observe the decay of the carrier density [see Figure 3.10(b)] by measuring FCA, which follows the dynamics of ($n_e + p_e$). Therefore, considering that the exact FCA coefficient $\left(\alpha_f = \sigma_r N\right)$ takes into account the weighted sum of excess electrons and holes as [61, 160]:

$$\alpha_f = (8.5n_e + 6.0p_e) \times 10^{-18}\mathrm{cm}^{-1}, \quad (3.16)$$

we cannot identify the decay of n_e and p_e separately by means of our pump-and-probe experiments. For this reason, we will use a theoretical model (that will be described in the next subsection 3.2.2) proposed in [167, 168, 163] that allows to evaluate the decay of n_e and p_e, taking into account the effect of recombination via flaws and carrier-trapping.

In the case of a nano-waveguide (illustrated in Figure 3.11), we assume that the number of flaws over the lateral surfaces is significantly larger. This is expected considering that top and bottom surfaces of silicon-on-insulator (SOI) waveguides are generally smooth [169] and that the lateral surfaces of the waveguides used in our experiments were patterned by optical lithography and Inductively Coupled Plasma - Reactive Ion Etching (ICP-RIE). In addition, given the large surface-to-volume ratio in nano-waveguides, we may anticipate that carrier-trapping at surface dominate in the recombination dynamics [152].

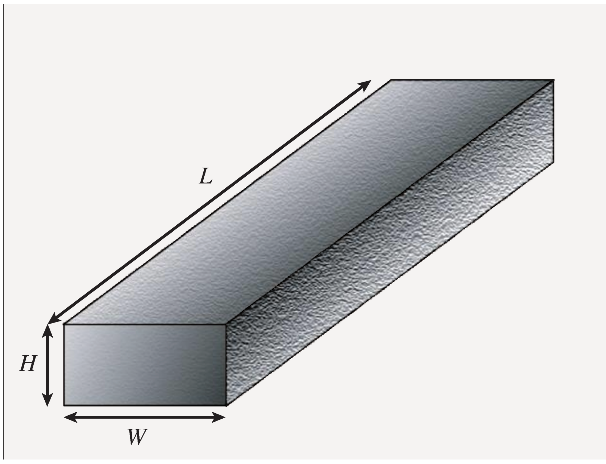

Figure 3.11: Illustration of a silicon nano-waveguide (of dimensions $W \times H \times L$) with surface and volume flaws.

If we consider that the recombination via flaws and carrier-trapping take place solely at the waveguide volume, thus, the fraction of flaws that must be filled to maintain charge neutrality (i.e., the net charge equals zero) is given by the ratio between the excess carrier imbalance between electrons and holes and the flaw density as:

$$\frac{(p_e - n_e)}{D_f}. \tag{3.17}$$

It is worth noting that p_e, n_e and D_f correspond to volume densities, which implies that these quantities scale with the waveguide dimensions. In contrast, if we consider that recombination via flaws and carrier-trapping take places mostly on the surface of the waveguide, the fraction of flaws that must be filled in order to maintain charge neutrality is now given by the ratio between the total number of carriers that must be in the flaws, i.e., $(p_e - n_e)W \times H \times L$, and the number of surface flaws, i.e., $2(H \times L)D_s$ (assuming that most flaws are located over the sidewalls with a flaw density D_s), hence:

$$\frac{(p_e - n_e)}{(2D_s/W)}. \tag{3.18}$$

Comparing Equations (3.17) and (3.18), one can see that the excess carrier unbalance can be as high as D_f or $2D_s/W$ in the cases of volume or surface carrier-trapping, respectively. However, in the case surface carrier-trapping, the carrier unbalance can be increased either by reducing W or increasing D_s, and therefore produce a significant non-linear decay dynamics as the one observed in our experiments.

In the next subsection we will describe the model used to evaluate the decay dynamics of n_e and $p_e$involving the process of recombination and carrier trapping through flaws.

3.2.2 Model of the dynamics of excess carriers in the presence of flaws

The model used in our study [163, 167, 168] considers that excess carriers recombine through a set of "monovalent" flaws with density D_f and a single energy level ϕ_f within the bandgap. The term monovalent stands for the possibility of the flaw to be in two states, either "full" or "empty," and separated by a charge q. The charge attributed to each state depends whether the flaw is donor or acceptor-like. A donor-like flaw is electrically neutral when full and charged when empty. Therefore, it is more likely to capture electrons than holes due to Coulomb attraction, resulting in a relationship between capture cross-sections such that $\sigma_n > \sigma_p$. In contrast, acceptor-like flaws are electrically neutral when empty, charged when full and characterized by $\sigma_p > \sigma_n$. As reported in [165], for the interface between silicon and silicon oxide (Si-SiO$_2$) $\sigma_n > \sigma_p$, thus we may assume that flaws at the surface of our tested waveguides can be considered as donor-like flaws.

The rate at which electrons are captured by flaws is given by [163]:

$$r = \frac{n\left[1 - P_e(\phi_f)\right]}{\tau_n}, \tag{3.19}$$

where n accounts for the equilibrium and excess electron densities, i.e. $(n_0 + n_e)$; $\tau_n = 1/(D_f \sigma_n v_n)$ is the shortest possible time constant for electron capture (being v_n the electron thermal velocity); and $P_e(\phi_f)$ corresponds to the flaw occupancy, considering those that are filled at thermal equilibrium and those that must be filled to maintain charge neutrality. In addition, besides electron-capture, in thermal equilibrium flaws may also emit electrons simultaneously at a rate given by [163]:

$$g = \frac{n_1 P_e(\phi_f)}{\tau_n}, \tag{3.20}$$

where $n_1$is the thermal electron density when the Fermi level ϕ is coincident with ϕ_f. Thus, the net rate for electron capture may be given by [163]:

$$\begin{aligned}(r-g) &= \frac{n\left[1-P_e\left(\phi_f\right)\right]-n_1 P_e\left(\phi_f\right)}{\tau_n} \\ &= \frac{1}{\tau_n}\left[\frac{(n_0+n_1+n_e)(n_e-p_e)}{D_f}+\frac{n_e n_1}{n_1+n_0}\right].\end{aligned} \tag{3.21}$$

Consequently, considering that the net carrier transitions to the flaws in Equation (3.21) correspond to the main recombination mechanism, that the carriers are generated at a rate G, and using the continuity equation for carrier dynamics of Equation (3.1), the temporal dynamics of the excess electron density n_e is then given by [163]:

$$\frac{\partial n_e}{\partial t} = G - \frac{1}{\tau_n}\left[\frac{(n_0+n_1+n_e)(n_e-p_e)}{D_f}+\frac{n_e n_1}{n_1+n_0}\right]. \tag{3.22}$$

Correspondingly, a similar equation that describes the temporal dynamics of the excess hole density p_e may be given as [163]:

$$\frac{\partial p_e}{\partial t} = G - \frac{1}{\tau_p}\left[\frac{(p_0+p_1+p_e)(p_e-n_e)}{D_f}+\frac{p_e p_1}{p_0+p_1}\right], \tag{3.23}$$

where $\tau_p = 1/(D_f \sigma_p v_p)$ is the shortest possible time constant for hole capture, v_p is the hole thermal velocity, p_0 is the equilibrium hole density, and $p_1$is thermal hole density when the Fermi level ϕ is coincident with ϕ_f.

Equations (3.22) and (3.23) can be handled by adopting a dimensionless notation, which is convenient when analyzing carrier transient decay dynamics [143, 163]. Considering that the silicon used to fabricate our tested SOI waveguides was p-type, the equilibrium hole density p_0 is used as a normalizing parameter and, therefore, Equations (3.22) and (3.23) can be written as:

$$\frac{\partial x}{\partial t'} = G' - \left[\frac{(x-y)[x+a(1+b)]}{D} + \frac{x}{1+b}\right], \tag{3.24}$$

$$\frac{\partial y}{\partial t'} = G' - \left[\frac{\gamma(y-x)(y+1+b)}{D} + \frac{\gamma b y}{1+b}\right], \tag{3.25}$$

where $x = n_e/p_0$ and $y = n_e/p_0$ are the normalized excess electron and hole densities, respectively. Similarly, the normalization applies for the thermal electron ($a = n_1/p_0$) and hole ($b = p_1/p_0$) densities when the Fermi level ϕ is coincident with ϕ_f, the density of flaws ($D = D_f/p_0$) and the generation rate ($G' = G\tau_n/p_0$). The parameter $\gamma = \tau_n/\tau_p$ determines whether a flaw is donor or acceptor-like, being smaller than unity for donor-like flaws and larger than unity for acceptor-like flaws. In addition, the time variable t' has been normalized by the shortest capture time constant that, in our case, corresponds to $t' = t/\tau_n$.

Given the short pulse excitation used in our experiments (i.e., $\tau_{FWHM} =$ 130 ps), we may assume that after carrier generation (via SPA and TPA) and at the beginning of the transient decay dynamics the excess densities of electrons and holes are equal, i.e., $x(0) = y(0)$. In Figure 3.12 we present the excess carrier decay for two values of the normalized flaw density D. Figure 3.12(a) corresponds to a small normalized flaw density of $D =$ 0.1 (D_f is an order of magnitude smaller than p_0). One can observe in Figure 3.12(a) that the excess electron (x) and hole (y) densities and the sum of both ($N' = x + y$) decay at the same rate, which evidences that no significant carrier-trapping takes place. In contrast, Figure 3.12(b) illustrates the transient decay of excess carriers assuming a large normalized flaw density of $D =$ 10 (D_f is an order of magnitude larger than p_0). In this case, the excess electron (x) and hole (y) densities evidently decay at different rates. On the one hand, given the donor-like characteristic of the flaws (we have used $\sigma_n = 8\sigma_p$), most electrons are trapped at earlier stages, not being able to immediately return to the valence band. For example, by assuming ϕ_f to be at the middle of the bandgap, the trap occupancy at thermal equilibrium, given as $b/(1+b)$ in the normalized notation, is of the order of 10^{-6}. On the other hand, the holes are less likely to be captured by flaws at earlier stages, since no significant amount of flaws have been filled by electrons. Therefore, as a consequence of carrier-trapping, the excess electron density decays at a much faster rate than that of the excess hole density, causing a significant carrier unbalance. The effect of this unbalance is also observed in the decay dynamics of the sum of both excess electrons and hole densities (which is presented as $N'/2$ to fit in the same scale of x and y) in Figure 3.12(b). One can see that at initial stages the decay is dominated by the fast decay in the excess electron density, whereas at later stages the decay is dominated by the slower decay of the excess hole density. This nonlinear decay dynamics is, therefore, in qualitative agreement with the one observed in our experiments of Figure 3.10(b).

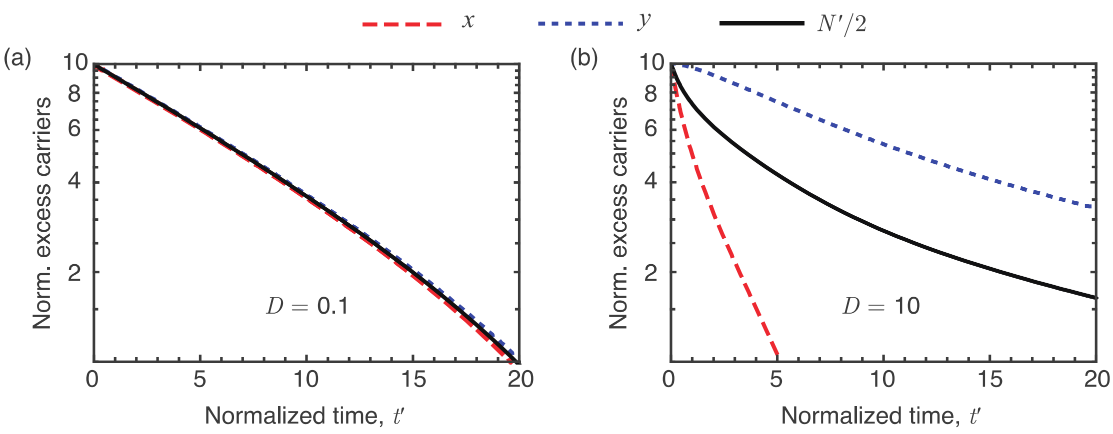

Figure 3.12: Transient decay dynamics of the normalized electron (x), hole (y) and half of the total carrier ($N'/2$) densities for different normalized flaw densities (a) $D = 0.1$ and (b) $D = 10$.

Symbol	Definition	Expression / Reference	Value
$\boldsymbol{\phi}$	Fermi level, assuming p-type and 10 (Ω-cm) SOI resistivity at 300 K	[151]	0.24 eV
$\boldsymbol{N_c}$	Effective density of states in the conduction band	[151]	2.8×10^{19} cm^{-3}
$\boldsymbol{N_v}$	Effective density of states in the valence band	[151]	1×10^{19} cm^{-3}
$\boldsymbol{E_g}$	Bandgap energy	[151]	1.12 eV
$\boldsymbol{n_0}$	Equilibrum free electron density	$N_c \exp\left(\frac{\phi - E_c}{k_B T}\right)$	4.4×10^{4} cm^{-3}
$\boldsymbol{p_0}$	Equilibrum free hole density	$N_v \exp\left(\frac{E_c - E_g - \phi}{k_B T}\right)$	1×10^{15} cm^{-3}

$\boldsymbol{\phi_f}$	Flaw energy level	Input parameter	0.5 eV
$\boldsymbol{n_1}$	Thermal electron density when $\phi = \phi_f$	$N_c \exp\left(\frac{\phi_f - E_c}{k_B T}\right)$	1.1×10^9 cm^{-3}
$\boldsymbol{p_1}$	Thermal hole density when $\phi = \phi_f$	$N_v \exp\left(\frac{E_c - E_g - \phi_f}{k_B T}\right)$	4.1×10^{10} cm^{-3}
$\boldsymbol{\sigma_n}$	Electron capture cross section	$\sigma_n = 8\sigma_p$	2.1×10^{-15} cm^2
$\boldsymbol{\sigma_p}$	Hole capture cross section	Input parameter	2.6×10^{-16} cm^2
$\boldsymbol{v_n}$	Electron thermal velocity	[151]	1.7×10^7 cm/s
$\boldsymbol{v_p}$	Hole thermal velocity	[151]	1.3×10^7 cm/s
$\boldsymbol{D_f}$	Flaw density	$2D_s/W$	$10^{14} - 10^{16}$ cm^{-3}
$\boldsymbol{D}$	Normalized flaw density	D_f/p_0	0.1 – 10
$\boldsymbol{\tau_n}$	Shortest electron capture time constant	$1/(D_f \sigma_n v_n)$	
$\boldsymbol{\tau_p}$	Shortest hole capture time constant	$1/(D_f \sigma_p v_p)$	
$\boldsymbol{\gamma}$	Ratio between shortest capture time constants	τ_n/τ_p	0.1
$\boldsymbol{t'}$	Normalized time	t/τ_n	0 – 100
$\boldsymbol{x}$	Normalized excess electron density	n_e/p_0	
$\boldsymbol{y}$	Normalized excess hole density	p_e/p_0	
$\boldsymbol{N'}$	Normalized excess carrier density	$N' = x + y$	
$\boldsymbol{a}$	Normalized thermal electron density when $\phi = \phi_f$	n_1/p_0	
$\boldsymbol{b}$	Normalized thermal hole density when $\phi = \phi_f$	p_1/p_0	

Table 3.2: Summary of definitions and parameters used in our calculations.

3.2.3 Comparing experimental and theoretical results

In Figure 3.13 we compare our experimental results of the carrier density as a function of time [Figure 3.13(a)] and instantaneous carrier lifetime as a function of carrier density [Figure 3.13(b)] with the theoretical results for the equivalent normalized parameters calculated by means of the single-energy flaw model [Figure 3.13(c) and Figure 3.13(d)]. It is worth noting that the calculated decay dynamics is in qualitative agreement with our measurements considering two main observations.

First, the non-exponential decay of the carrier density observed in our experiments shown in Figure 3.13(a) [a detail of the first few nanoseconds of the measurements shown in Figure 3.10(b)] is also displayed in our calculations shown in Figure 3.13(c). Both measurements and calculations exhibit an early fast decay of the carrier density, which is explained due to significant-trapping of excess electrons by the empty flaws, followed by a slower decay due to trapping of excess holes by the flaws that have been filled.

Second, the measured and calculated decay dynamics show a clear dependence on the initial carrier density, which is observed by using different pump power levels in the experiments and normalized initial carrier densities $N'(0)$ in the calculations. This dependency leads to different carrier density decay trajectories, which does not correspond to a simple shift in the vertical scale between curves in Figure 3.13(a) and Figure 3.13(c). In order to clearly illustrate this effect, we present the measured and calculated instantaneous carrier lifetime, that can be estimated by $\tau_c = -N(t)[dN(t)/dt]^{-1}$ [143, 170, 171], as a function of the measured and normalized carrier densities in Figure 3.13(b) and Figure 3.13(d), respectively. One can see that for the same carrier density, different curves in Figure 3.13(b) or Figure 3.13(d) present a different instantaneous carrier lifetime. Therefore, given the qualitative good agreement of our calculations with our measurements, the “memory-like” behavior of the carrier density in terms of the initial carrier density may also be explained as result of the significant carrier-trapping in the nano-waveguide.

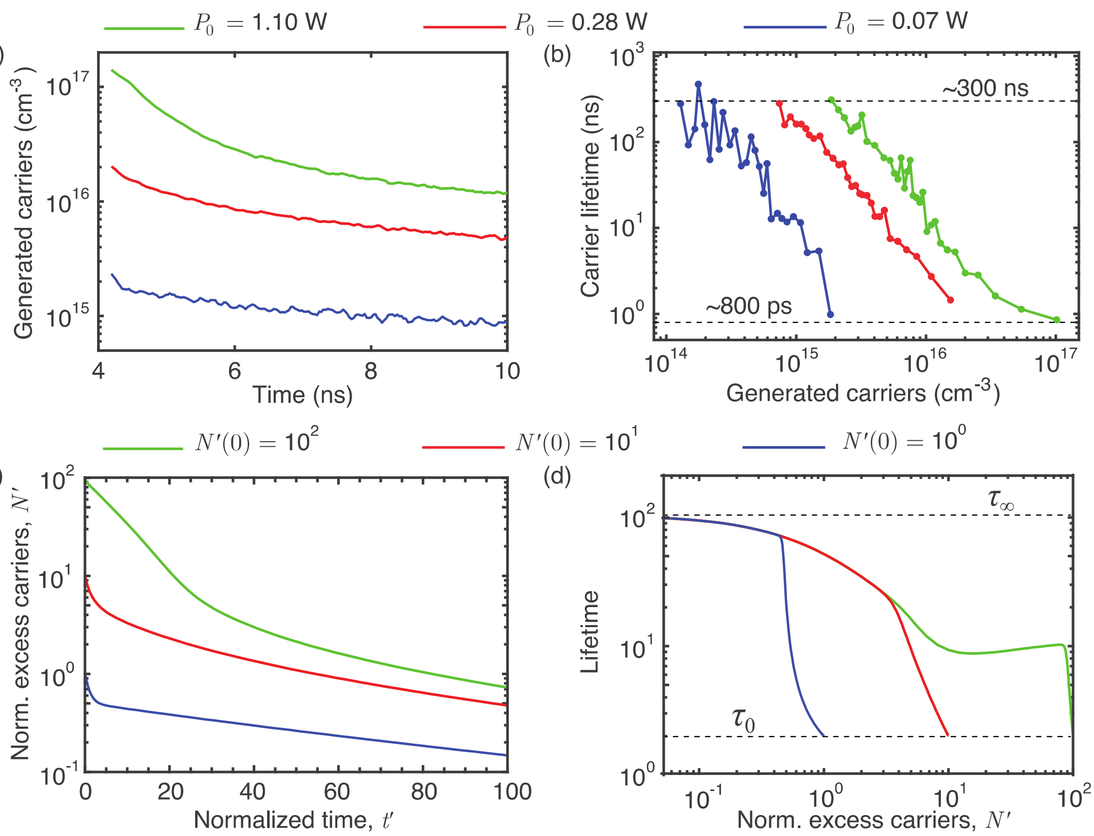

Figure 3.13:Experimental results for (a) carrier density as a function of time and (b) carrier lifetime as a function of carrier density. Theoretical results for (c) normalized carrier density as a function of normalized time and (d) normalized carrier life time as a function of normalized carrier density.

We want to point out that performing a quantitative analysis of the carrier decay dynamics for a particular waveguide would require, besides a more complex model that considers different types of flaws and Auger recombination, proper characterization of the flaw energy distribution and capture cross-sections. However, the single-energy flaw model used in our study also allows us to predict that the carrier lifetime has slow and fast limits, which is also observed in our measurements. These limits are denoted by discontinuous lines in Figure 3.13(b) and Figure 3.13(d).

The slow limit of the carrier lifetime corresponds to the slow decay dynamics observed at later stages in Figure 3.13(a) and Figure 3.13(c). Considering that at this stage ($t' = \infty$), most excess electrons have been captured by flaws, i.e., $x(\infty) \approx 0$, and that the decay dynamics is mainly determined by the decay of the excess hole density [Equation (3.25)], it is possible to obtain an expression for the slow limit of the carrier lifetime (τ_∞) in terms of normalized parameters given by:

$$\tau_\infty = \frac{D(1+b)}{\gamma[Db + (1+b)^2]}, \tag{3.26}$$

If we consider that the flaw energy level (ϕ_f) is located near the middle of the bandgap and that the Fermi level is close to the valence band in a p-type semiconductor (see Table 3.2), we find that $b \approx 0$. This allows us to obtain an approximation for the slow limit of the carrier lifetime as $\tau_\infty \approx D\gamma^{-1}$ and also in terms of absolute parameters as $t_\infty \approx 1/(p_0\sigma_p v_p)$. From our measurements $t_\infty \approx 300$ ns, and by using the parameters used in our calculations the hole capture cross-section results to be $\sigma_p \approx 2.6 \times 10^{-16}$ cm^2. Even though the capture cross-sections would depend on the type of oxide used as cladding material and particular waveguide fabrication processes, the estimated value for σ_p lies between the order of magnitude of the measurements for the interface between Si and SiO_2 reported in [165], which were performed in metal-oxide-semiconductor (MOS) capacitors by means of small pulse deep level transient spectroscopy.

The fast limit of the carrier lifetime, on the other hand, corresponds to the early fast decay dynamics observed in Figure 3.13(a) and Figure 3.13(c). At this stage ($t' = 0$), the densities of excess electrons and holes are equal, i.e., $x(0) = y(0)$, and the decay dynamics is dominated by the fast decay of the excess electron density [Equation (3.24)], then the fast limit of the carrier lifetime (τ_0) can be given as:

$$\tau_0 = 2(1+b), \tag{27}$$

Correspondingly, considering $b \approx 0$, the fast limit can be also approximated as $\tau_0 \approx 2$ and in terms of absolute parameters as $t_0 \approx W/(D_s\sigma_n v_n)$. It is worth noting that, in contrast to the slow limit of the carrier lifetime (t_∞), the fast limit may be modified by changing the width of the waveguide (W) or the surface density of flaws (D_s). This could be used to even obtain a faster decay dynamics, either by reducing the waveguide dimensions or processing its surface, and be exploited in the development of all-optical switching devices, as we will show in the next subsection. From our measurements $t_0 \approx 800$ ps, which leads to a surface flaw density

$D_s \approx 1.6 \times 10^{12}$ cm^{-2} (obtained by using the parameters employed in our calculations). This estimated density of surface flaws lays within the order of magnitude of other measurements for the interface between silicon and oxide [165, 172].

3.2.4 Possibilities of free-carrier dynamics in all-optical switching applications

Given the "memory-like" behavior of the dynamics observed in the previous subsection (Figure 3.13), one may note that operating at high carrier densities leads to a faster dynamics. Therefore, one possible application based on this observation would be all-optical switching based on the optical loss induced by optical pump pulses of few ns duration (i.e. non-degenerate TPA and FCA). Thus, we have changed the short pulse pump by a pseudo-random sequence of 10 ns symbol duration and measure the normalized nonlinear loss of the probe by using different pump power levels (see Figure 3.14). It is worth noting the effect of accumulated carriers generated by each symbol, evidenced by the change in the dynamics along the sequence. In addition, one can observe that by using higher pumping power (i.e., a higher carrier density), not only the decay but also the built-up dynamics become faster.

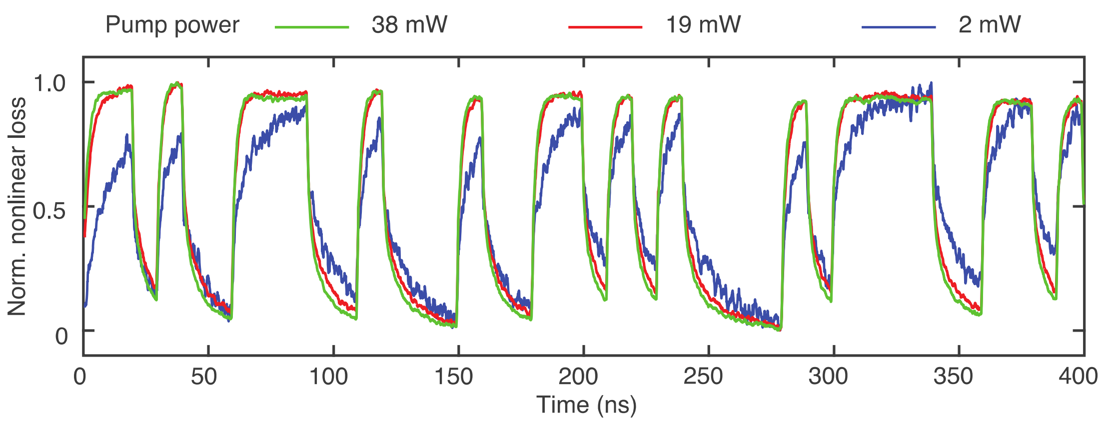

Figure 3.14: Normalized nonlinear loss when using a pseudo-random sequence of 40-symbols of length and different pump power levels.

Considering the word-dependency observed in Figure 3.14 due to the accumulation of free-carriers, in order to have a more clear estimate of the time responses for a possible switching application, we have also evaluated the dynamics resulting from a single pump pulse of 20 ns of width. The normalized nonlinear loss in the case of a single pulse is shown in Figure 3.15(a) for different pump power levels. We have also evaluated the rising and falling times for each pump power, which are presented in Figure 3.15(b). Note that the rising time decreases by one order of magnitude, whereas the falling time decreases by more than one order of magnitude over the range of pump power used (i.e., from 2 to 170 mW).

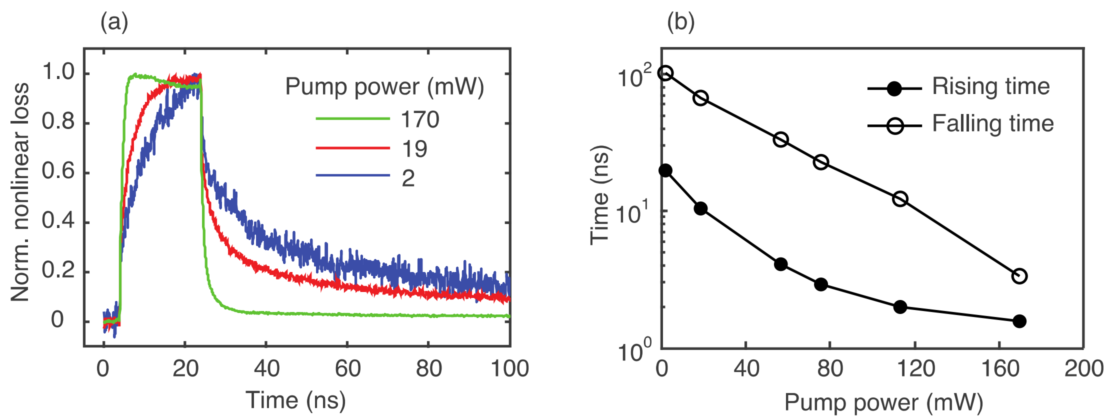

Figure 3.15: (a) Normalized nonlinear loss by using a single pump pulse of 20 of width and different pump power levels. (b) Rising (10 to 90%) and falling (90 to 10%) times as a function of the pump power.

We want to point out that even though our demonstrations seem to be far from a practical all-optical switching application, our experiments along with our physical explanation for the observed non-linear free-carrier dynamics based on trap-assisted recombination, give some insights for the development of practical all-optical switches. On the one hand, as we have discussed in the previous subsection, even a fast response time could be achieved by reducing the waveguide dimensions or increasing the density of surface flaws by surface processing. On the other hand, considering the free-carrier accumulation effect observed in Figure 3.14, one could in principle use a CW laser as a bias of the carrier density and, therefore, reduce the change of the dynamics along the sequence.

3.2.5 Discussion

In this section we have presented an experimental and theoretical description of the recombination dynamics of free carriers in silicon nano-waveguides. By performing pump-and-probe experiments we have been able to observe the decay dynamics of the density of free carriers generated by a short optical pump pulse. In contrast to an exponential decay with a single lifetime (usually assumed in silicon photonics applications), the observed dynamics displays two interesting characteristics:

(i) A clear lifetime dependency on the carrier density evidenced by a faster decay rate at the beginning of the recombination and a slower decay at later stages.

(ii) A kind of memory in the decay dynamics given by the dependency of the evolution of the carrier lifetime on the initial carrier density.

Considering that radiative and Auger recombination could be ignored in our study, our experimental observations can be explained in terms of carrier-recombination via states located within the bandgap that arise from flaws. However, we want to point out that carrier recombination via flaw states can lead to two different scenarios.

On the one hand, for relatively small flaw densities (i.e., $D_f \ll p_0$) flaws act mainly as recombination centers and, therefore, excess electron and hole densities decay at the same rate. Under these conditions, it is possible to obtain an expression for the carrier lifetime as it was derived by *Shockley and Read* [164] and also by *Hall* [173]. The so-called *Shockley-Read-Hall* (SRH) recombination model could also reproduce a dependency of the carrier lifetime on the carrier density that leads to a non-linear decay dynamics. However, the SRH model cannot explain the carrier lifetime dependency on the initial carrier density.

On the other hand, for large flaw densities (comparable to the excess carrier density) significant carrier-trapping by flaws takes place, which causes the density of excess electrons and holes to decay at different rates leading to a non-linear decay dynamics. This situation is more likely to occur in nano-waveguides, considering that the flaw density can be high due to the large surface-to-volume ratio and the presence of surface states at the Si/SiO_2 interface. Therefore, we have used a single-energy flaw theoretical model that allows to evaluate the effect of carrier-trapping and separately identify the decay dynamics of both excess electron and hole densities.

Our theoretical calculations present a qualitative agreement with our experiments, and allows us to explain our main observations in terms of carrier trapping by flaws. The observed initial decay in the carrier density can be attributed to the fast decay of the excess electron density, considering that at early stages electrons are being rapidly trapped by empty flaws given their donor-like characteristics for the Si/SiO_2 interface [165]. In contrast, the slower dynamics observed at later stages can be explained in terms of hole capture by flaws that have been filled. In addition, the memory behavior, given by the dependency of the carrier density decay evolution on the initial carrier density, can be also attributed to carrier trapping. This dependency exhibits a faster decay for higher excess carrier densities which could be explained by the fact that more electrons are available to be trapped by empty flaws.

An additional agreement between our calculations and our experiments is the existence of slow and fast limits in the instantaneous carrier lifetime. For our tested waveguide, these limits correspond to $t_\infty \approx 300$ ns and $t_0 \approx 800$ ps. Interestingly, by means of the theoretical model we can anticipate that it is possible to obtain an even faster limit by reducing the waveguide width or increasing the density of flaws. For example, one interesting study would be the change in the dynamics for the quasi-TM mode that has a larger overlap with the waveguide sidewalls. This possibility, along with the fact that a faster dynamics is obtained operating at high-carrier densities, gives some insights that can be exploited in the development of all-optical switching applications as we have shown in this section.

3.3 Conclusions

In conclusion, we have presented a comprehensive experimental and theoretical description of the linear and nonlinear generation and dynamics of free carriers in silicon nano-waveguides at the spectral band of 1550 nm that, to the best of our knowledge, has not been presented elsewhere.

Our pump-and-probe experiments along with the derived expressions allowed us to simultaneously measure the instantaneous carrier lifetime and SPA and TPA coefficients of a silicon strip nano-waveguide with good accuracy. Our reported SPA and TPA coefficients and our detailed description of the linear and nonlinear carrier generation may impact several linear and nonlinear applications based on silicon strip nano-waveguides. In addition, our proposed method may be useful for other groups to test their own waveguides and fabrication processes.

On the other hand, we have been able to explain the observed complex decay dynamics of the generated carrier density in terms of significant carrier-trapping by flaws that result from the large surface-to-volume ratio in nano-waveguides. That is, the dependency of the instantaneous carrier lifetime with the carrier density and the dependency on the decay evolution with the initial carrier density or pumping power. In addition, our pump-and-probe experiments along with the implemented theoretical model allowed us to give some insights for obtaining even a faster dynamics by reducing the waveguide geometry or increasing the density of flaws and, therefore, open new opportunities in the development of all-optical switching applications based on silicon nano-waveguides.

4. General Conclusions and Future Work

The main goal of this thesis was to explore fundamental limitations in the development of practical applications of nonlinear optics in well-stablished waveguide platforms such as optical fibers and silicon nano-waveguides.

In optical fibers, the presence of dispersion fluctuations has been recognized as a main limitation in FWM-based devices. Although, theoretical predictions have shown the effect of fluctuations of the zero-dispersion wavelength in the efficiency of FWM, we have identified a lack of experimental evidence of the characteristics and origins of such fluctuations. By exploiting the sensitivity of FWM pumped by an incoherent source and based on numerical calculations of fiber dispersion, we have been able to show that besides the zero-dispersion wavelength, high-order dispersion significantly contributes to the dispersion fluctuations in an optical fiber. In addition, we have been able to show that bending causes a significant change in the dispersive characteristics of an optical fiber, and that the effect of bending is strongly related with changes of fiber geometry and mode confinement. Our main observations, not reported before to the best of our knowledge, are fundamental in the development of compact FWM-based devices in optical fibers. We also believe that the identified relationship between bending and waveguide geometry could be exploited for dispersion engineering of novel fiber designs and integrated waveguides.

By performing several experimental improvements and obtaining a better interpretation of the phase-matching condition of the FWM process, we have been able to show the capabilities of our method for measuring high-order dispersion parameters with good accuracy. Therefore, we have shown theoretical examples in silicon-nano waveguides, although neglecting the effect of two-photon absorption and free-carrier effects. Our study shows that the high-nonlinearity and large high-order dispersion in these waveguides allow the application of our measuring method. Therefore, an interesting future study would be to apply our method for accurately measuring high-order dispersion in silicon nano-waveguides, a task that has been limited by using other characterization methods.

Despite the promising nonlinear optical demonstrations in silicon nano-waveguides, the generation of free carriers via two-photon absorption has been recognized as the main limitation in the development of nonlinear devices around 1550 nm. However, we have identified that a better understanding of carrier generation and recombination mechanisms and their dynamics is fundamental for studies of nonlinear optical phenomena and the development of all-optical devices in silicon nano-waveguides. Therefore, by using time-resolved pump-and-probe experiments and theoretical developments we have provided a detailed description of the carrier generation mechanisms, identifying the contributions of single and two-photon absorption. This description has not been presented in the literature, to the best of our knowledge. In addition, our experiments allowed us to observe a complex decay dynamics of the carrier density, showing that the instantaneous carrier lifetime changes as the carrier density decays and a dependency of the decay trajectory with the pumping power. We have explained this complex dynamics in terms of significant carrier-trapping due to the large surface-to-volume ratio and surface termination of the nano-waveguides, also not reported in the literature. We have also shown that the observed complex dynamics leads to a faster operation at high carrier densities, which can be useful, for example, in all-optical switching applications. Therefore, an interesting future study consists in engineering the geometry and processing conditions of nano-waveguides in order to develop all-optical switches.

References

[1] P. A. Franken, A. E. Hill, C. W. Peters y G. Weinreich, «Generation of optical harmonics,» *Physical Review Letters,* vol. 7, nº 4, p. 118, 1961.

[2] T. H. Maiman, «Stimulated optical radiation in ruby,» *Nature,* vol. 187, pp. 493-494, 1960.

[3] I. P. Kaminow y E. H. Turner, «Electrooptic light modulators,» *Applied Optics,* vol. 5, nº 10, pp. 1612-1628, 1966.

[4] R. H. Stolen y E. P. Ippen, «Raman gain in glass optical waveguides,» *Applied Physics Letters,* vol. 22, nº 6, pp. 276-278, 1973.

[5] C. Headley y G. P. Agrawal, Raman amplification in fiber optical communication systems, Elsevier Academic Press, 2005.

[6] J. A. Armstrong, N. Bloembergen, J. Ducuing y P. S. Pershan, «Interactions between light waves in a nonlinear dielectric,» *Physical review,* vol. 127, nº 6, p. 1918, 1962.

[7] G. Cerullo y S. De Silvestri, «Ultrafast optical parametric amplifiers,» *Review of scientific instruments,* vol. 74, nº 1, pp. 1-18, 2003.

[8] J. K. Ranka, R. S. Windeler y A. J. Stentz, «Visible continuum generation in air--silica microstructure optical fibers with anomalous dispersion at 800 nm,» *Optics letters,* vol. 25, nº 1, pp. 25-27, 2000.

[9] G. Genty, S. Coen y J. M. Dudley, «Fiber supercontinuum sources,» *JOSA B,* vol. 24, nº 8, pp. 1771-1785, 2007.

[10] R. W. Boyd y G. L. Fischer, «Nonlinear Optical Materials,» de *Encyclopedia of Materials: Science and Technology 2nd Ed.*, Elsevier Science, 2001.

[11] P. Russell, «Photonic crystal fibers,» *science,* vol. 299, nº 5605, pp. 358-362, 2003.

[12] J. M. Dudley y J. R. Taylor, «Ten years of nonlinear optics in photonic crystal fibre,» *Nature Photonics,* vol. 3, nº 2, p. 85, 2009.

[13] J. Leuthold, C. Koos y W. Freude, «Nonlinear silicon photonics,» *Nature Photonics,* vol. 4, nº 8, p. 535, 2010.

[14] D. J. Moss, R. Morandotti, A. L. Gaeta y M. Lipson, «New CMOS-compatible platforms based on silicon nitride and Hydex for nonlinear optics,» *Nature photonics,* vol. 7, nº 8, p. 597, 2013.

[15] R. Stolen y J. Bjorkholm, «Parametric amplification and frequency conversion in optical fibers,» *IEEE Journal of Quantum Electronics,* vol. 18, nº 7, pp. 1062-1072, 1982.

[16] M. E. Marhic, Y. Park, F. S. Yang y L. G. Kazovsky, «Broadband fiber-optical parametric amplifiers and wavelength converters with low-ripple Chebyshev gain spectra,» *Optics letters,* vol. 21, nº 17, pp. 1354-1356, 1996.

[17] M. E. Marhic, Fiber Optical Parametric Amplifiers, Oscillators and Related Devices, Cambridge University Press, 2008.

[18] C. J. McKinstrie y M. G. Raymer, «Four-wave-mixing cascades near the zero-dispersion frequency,» *Optics express,* vol. 14, nº 21, pp. 9600-9610, 2006.

[19] A. C. S Jr, J. M. C. Boggio, A. A. Rieznik, H. E. Hernandez-Figueroa, H. L. Fragnito y J. C. Knight, «Highly efficient generation of broadband cascaded four-wave mixing products,» *Optics Express,* vol. 16, nº 4, pp. 2816-2828, 2008.

[20] S. Coen, A. H. L. Chau, R. Leonhardt, J. D. Harvey, J. C. Knight, W. J. Wadsworth y P. S. J. Russell, «Supercontinuum generation by stimulated Raman scattering and

parametric four-wave mixing in photonic crystal fibers,» *JOSA B,* vol. 19, nº 4, pp. 753-764, 2002.

[21] J. C. Travers, «High average power supercontinuum sources,» *Pramana,* vol. 75, nº 5, pp. 769-785, 2010.

[22] E. J. R. Kelleher, «Pump wave coherence, modulation instability and their effect on continuous-wave supercontinua,» *Optical Fiber Technology,* vol. 18, nº 5, pp. 268-282, 2012.

[23] M. A. Foster, A. C. Turner, J. E. Sharping, B. S. Schmidt, M. Lipson y A. L. Gaeta, «Broad-band optical parametric gain on a silicon photonic chip,» *Nature,* vol. 441, nº 7096, p. 960, 2006.

[24] A. Pasquazi, Y. Park, J. Azaña, F. Légaré, R. Morandotti, B. E. Little, S. T. Chu y D. J. Moss, «Efficient wavelength conversion and net parametric gain via Four Wave Mixing in a high index doped silica waveguide,» *Optics express,* vol. 18, nº 8, pp. 7634-7641, 2010.

[25] Y. Okawachi, K. Saha, J. S. Levy, Y. H. Wen, M. Lipson y A. L. Gaeta, «Octave-spanning frequency comb generation in a silicon nitride chip,» *Optics letters,* vol. 36, nº 17, pp. 3398-3400, 2011.

[26] W. H. Reeves, D. V. Skryabin, F. Biancalana, J. C. Knight, P. S. J. Russell, F. G. Omenetto, A. Efimov y A. J. Taylor, «Transformation and control of ultra-short pulses in dispersion-engineered photonic crystal fibres,» *Nature,* vol. 424, nº 6948, p. 511, 2003.

[27] A. C. Turner-Foster, M. A. Foster, R. Salem, A. L. Gaeta y M. Lipson, «Frequency conversion over two-thirds of an octave in silicon nanowaveguides,» *Optics express,* vol. 18, nº 3, pp. 1904-1908, 2010.

[28] M. Karlsson, «Four-wave mixing in fibers with randomly varying zero-dispersion wavelength,» *JOSA B,* vol. 15, nº 8, pp. 2269-2275, 1998.

[29] N. Kuwaki y M. Ohashi, «Evaluation of longitudinal chromatic dispersion,» *Journal of Lightwave Technology,* vol. 8, nº 10, pp. 1476-1481, 1990.

[30] M. Farahmand y M. de Sterke, «Parametric amplification in presence of dispersion fluctuations,» *Optics express,* vol. 12, nº 1, pp. 136-142, 2004.

[31] B. P.-P. Kuo, J. M. Fini, L. Grüner-Nielsen y S. Radic, «Dispersion-stabilized highly-nonlinear fiber for wideband parametric mixer synthesis,» *Optics express,* vol. 20, nº 17, pp. 18611-18619, 2012.

[32] F. Yaman, Q. Lin, S. Radic y G. P. Agrawal, «Impact of dispersion fluctuations on dual-pump fiber-optic parametric amplifiers,» *IEEE Photonics Technology Letters,,* vol. 16, nº 5, pp. 1292-1294, 2004.

[33] J. S. Y. Chen, S. G. Murdoch, R. Leonhardt y J. D. Harvey, «Effect of dispersion fluctuations on widely tunable optical parametric amplification in photonic crystal fibers,» *Optics express,* vol. 14, nº 20, pp. 9491-9501, 2006.

[34] C. Mazzali, D. F. Grosz y H. L. Fragnito, «Simple method for measuring dispersion and nonlinear coefficient near the zero dispersion wavelength of optical fibers,» *IEEE Photonics Technology Letters,* vol. 11, nº 2, pp. 251-253, 1999.

[35] B. Auguie, A. Mussot, A. Boucon, E. Lantz y T. Sylvestre, «Ultralow chromatic dispersion measurement of optical fibers with a tunable fiber laser,» *IEEE Photonics Technology Letters,* vol. 18, nº 17, pp. 1825-1827, 2006.

[36] J. M. C. Boggio y H. L. Fragnito, «Simple four-wave-mixing-based method for measuring the ratio between the third-and fourth-order dispersion in optical fibers,» *JOSA B,* vol. 24, nº 9, pp. 2046-2054, 2007.

[37] H. Onaka, K. Otsuka, H. Miyata y T. Chikama, «Measuring the longitudinal distribuition of four-wave- mixing efficiency in dispersion-shifted fibers,» *IEEE photonics technology letters},* vol. 6, nº 12, pp. 1454-1456, 1994.

[38] I. Brener, P. P. Mitra, D. D. Lee, D. Thomson y D. L. Philen, «High-resolution zero-dispersion wavelength mapping in single-mode fiber,» *Optics letters,* vol. 23, nº 19, pp. 1520-1522, 1998.

[39] M. González-Herráez, P. Corredera y M. L. a. M. J. A. Hernanz, «Retrieval of the zero-dispersion wavelength map of an optical fiber from measurement of its continuous-wave four-wave mixing efficiency,» *Optics letters,* vol. 27, nº 17, pp. 1546-1548, 2002.

[40] A. Mussot, E. Lantz, A. Durecu-Legrand, C. Simonneau, D. Bayart, T. Sylvestre y H. Maillotte, «Zero- dispersion wavelength mapping in short single-mode optical fibers using parametric amplification,» *IEEE photonics technology letters,* vol. 18, nº 1, pp. 22-24, 2006.

[41] M. Eiselt, R. M. Jopson y R. H. Stolen, «Nondestructive position-resolved measurement of the zero-dipersion wavelength in an optical fiber,» *Journal of lightwave technology,* vol. 15, nº 1, pp. 135-143, 1997.

[42] R. M. Jopson, M. Eiselt, R. H. Stolen, R. M. Derosier, A. M. Vengsarkar y U. Koren, «Non-destructive dispersion-zero measurements along an optical fibre,» *Electronics Letters,* vol. 31, nº 24, pp. 2115-2117, 1995.

[43] S. Nishi y M. Saruwatari, «Technique for measuring the distributed zero dispersion wavelength of optical fibers using pulse amplification caused by modulation instability,» *Electronics Letters,* vol. 31, nº 3, pp. 225-226, 1995.

[44] L. F. Mollenauer, P. V. Mamyshev y M. J. Neubelt, «Method for facile and accurate measurement of optical fiber dispersion maps,» *Optics letters,* vol. 21, nº 21, pp. 1724-1726, 1996.

[45] K.-Y. Song, M. G. Herráez y L. Thévenaz, «Mapping of chromatic-dispersion distribution along optical fibers with 20-m spatial resolution,» *Journal of lightwave technology,* vol. 23, nº 12, p. 4140, 2005.

[46] E. Myslivets, N. Alic, J. R. Windmiller y S. Radic, «A new class of high-resolution measurements of arbitrary-dispersion fibers: localization of four-photon mixing process,» *Journal of Lightwave Technology,* vol. 27, nº 3, pp. 364-375, 2009.

[47] P. K. A. Wai, C. R. Menyuk, H. Chen y Y. C. Lee, «Soliton at the zero-group-dispersion wavelength of a single-model fiber,» *Optics letters,* vol. 12, nº 8, pp. 628-630, 1987.

[48] N. Akhmediev y M. Karlsson, «Cherenkov radiation emitted by solitons in optical fibers,» *Physical Review A,* vol. 51, nº 3, p. 2602, 1995.

[49] A. Blanco-Redondo, C. M. De Sterke, J. E. Sipe, T. F. Krauss, B. J. Eggleton y C. Husko, «Pure-quartic solitons,» *Nature communications,* vol. 7, p. 10427, 2016.

[50] G. P. Agarwal, Nonlinear fiber optics, 5th edition, San Diego, CA: Academic Press, 2001.

[51] J. M. Dudley y J. R. Taylor, Supercontinuum generation in optical fibers, Cambridge University Press, 2010.

[52] M. Nakazawa, T. Yamamoto y K. R. Tamura, «1.28 Tbit/s-70 km OTDM transmission using third-and fourth-order simultaneous dispersion compensation with a phase modulator,» *Electronics letters,* vol. 36, nº 24, pp. 2027-2029, 2000.

[53] J. Capmany, D. Pastor, S. Sales y B. Ortega, «Effects of fourth-order dispersion in very high-speed optical time-division multiplexed transmission,» *Optics letters,* vol. 27, nº 11, pp. 960-962, 2002.

[54] L. Zong, F. Luo, Y. Wang y X. Cao, «Dispersion compensation module for 100 Gbit/s optical system and beyond,» *Optical Fiber Technology,* vol. 17, nº 3, pp. 227-232, 2011.

[55] M. A. Foster, A. C. Turner, R. Salem, M. Lipson y A. L. Gaeta, «Broad-band continuous-wave parametric wavelength conversion in silicon nanowaveguides,» *Optics Express,* vol. 15, nº 29, pp. 12949-12958, 2007.

[56] R. Jones, H. Rong, A. Liu, A. W. Fang, M. J. Paniccia, D. Hak y O. Cohen, «Net continuous wave optical gain in a low loss silicon-on-insulator waveguide by stimulated Raman scattering,» *Optics Express},* vol. 13, nº 2, pp. 519-522, 2005.

[57] E. A. Kittlaus, H. Shin y P. T. Rakich, «Large Brillouin amplification in silicon,» *Nature Photonics,* vol. 10, nº 7, p. 463, 2016.

[58] R. Van Laer, B. Kuyken, D. Van Thourhout y R. Baets, «Interaction between light and highly confined hypersound in a silicon photonic nanowire,» *Nature Photonics,* vol. 9, nº 3, p. 199, 2015.

[59] L. Yin y G. P. Agrawal, «Impact of two-photon absorption on self-phase modulation in silicon waveguides,» *Optics letters,* vol. 32, nº 14, pp. 2031-2033, 2007.

[60] F. Leo, S.-P. Gorza, S. Coen, B. Kuyken y G. Roelkens, «Coherent supercontinuum generation in a silicon photonic wire in the telecommunication wavelength range,» *Optics letters,* vol. 40, nº 1, pp. 123-126, 2015.

[61] Q. Lin, O. J. Painter y G. P. Agrawal, «Nonlinear optical phenomena in silicon waveguides: modeling and applications,» *Optics express,* vol. 15, nº 25, pp. 16604-16644, 2007.

[62] Y. Zhang, C. Husko, S. Lefrancois, I. H. Rey, T. F. Krauss, J. Schröder y B. J. Eggleton, «Non-degenerate two-photon absorption in silicon waveguides: analytical and experimental study,» *Optics express,* vol. 23, nº 13, pp. 17101-17110, 2015.

[63] A. R. Motamedi, A. H. Nejadmalayeri, A. Khilo, F. X. Kärtner y E. P. Ippen, «Ultrafast nonlinear optical studies of silicon nanowaveguides,» *Optics express,* vol. 20, nº 4, pp. 4085-4101, 2012.

[64] Y. Zhang, C. a. S. J. Husko y B. J. Eggleton, «Pulse evolution and phase-sensitive amplification in silicon waveguides,» *Optics letters,* vol. 39, nº 18, pp. 5329-5332, 2014.

[65] I. D. Rukhlenko, M. Premaratne y G. P. Agrawal, «Nonlinear propagation in silicon-based plasmonic waveguides from the standpoint of applications,» *Optics express,* vol. 19, nº 1, pp. 206-217, 2011.

[66] A. Blanco-Redondo, C. Husko, D. Eades, Y. Zhang, J. Li, T. Krauss y B. Eggleton, «Observation of soliton compression in silicon photonic crystals,» *Nature communications,* vol. 5, p. 3160, 2014.

[67] V. R. Almeida, C. A. Barrios, R. R. Panepucci y M. Lipson, «All-optical control of light on a silicon chip,» *Nature,* vol. 431, nº 7012, p. 1081, 2004.

[68] L. Fan, J. Wang, L. T. Varghese, H. Shen, B. Niu, Y. Xuan, A. M. Weiner y M. Qi, «An all-silicon passive optical diode,» *Science,* vol. 335, nº 6067, pp. 447-450, 2011.

[69] R. W. Boyd, Nonlinear Optics, Elsevier, 2008.

[70] P. N. a. C. D. Butcher, The elements of nonlinear optics, Cambridge university press, 1991.

[71] S. Afshar y T. M. Monro, «A full vectorial model for pulse propagation in emerging waveguides with subwavelength structures part I: Kerr nonlinearity,» *Optics express,* vol. 17, nº 4, pp. 2298-2318, 2009.

[72] V. S. Afshar, T. Monro y C. M. De Sterke, «Understanding the contribution of mode area and slow light to the effective Kerr nonlinearity of waveguides,» *Optics Express,* vol. 21, nº 15, pp. 18558-18571, 2013.

[73] D. T. H. Tan, K. Ikeda, P. C. Sun y Y. Fainman, «Group velocity dispersion and self phase modulation in silicon nitride waveguides,» *Applied Physics Letters,* vol. 96, nº 6, p. 061101, 2010.

[74] E. Dulkeith, F. Xia, L. Schares, W. M. J. Green y Y. A. Vlasov, «Group index and group velocity dispersion in silicon-on-insulator photonic wires,» *Optics express,* vol. 14, nº 9, pp. 3853-3863, 2006.

[75] A. C. Turner, C. Manolatou, B. S. Schmidt, M. Lipson, M. A. Foster, J. E. Sharping y A. L. Gaeta, «Tailored anomalous group-velocity dispersion in silicon channel waveguides,» *Optics express,* vol. 14, nº 10, pp. 4357-4362, 2006.

[76] J. M. C. Boggio, D. Bodenmüller, T. Fremberg, R. Haynes, M. M. Roth, R. Eisermann, M. Lisker, L. Zimmermann y M. Böhm, «Dispersion engineered silicon nitride waveguides by geometrical and refractive-index optimization,» *JOSA B,* vol. 31, nº 11, pp. 2846-2857, 2014.

[77] L. Zhang, Y. Yue, R. G. Beausoleil y A. E. Willner, «Flattened dispersion in silicon slot waveguides,» *Optics express,* vol. 18, nº 19, pp. 20529-20534, 2010.

[78] J. I. Dadap, N. C. Panoiu, X. Chen, I. W. Hsieh, X. Liu, C. Y. Chou, E. Dulkeith, S. J. McNab, F. Xia, W. M. J. Green, L. Sekaric, Y. A. Vlasov y R. M. J. Osgood, «Nonlinear-optical phase modification in dispersion-engineered Si photonic wires,» *Optics Express,* vol. 16, nº 2, pp. 1280-1299, 2008.

[79] X. Liu, W. M. J. Green, X. Chen, I.-W. Hsieh, J. I. Dadap, Y. A. Vlasov y R. M. Osgood Jr, «Conformal dielectric overlayers for engineering dispersion and effective nonlinearity of silicon nanophotonic wires,» *Optics letters,* vol. 33, nº 24, pp. 2889-2891, 2008.

[80] M. E. Marhic, N. Kagi, T. K. Chiang y L. G. Kazovsky, «Broadband fiber optical parametric amplifiers,» *Optics letters,* vol. 21, nº 8, pp. 573-575, 1996.

[81] J. M. C. Boggio, S. Tenenbaum y H. L. Fragnito, «Amplification of broadband noise pumped by two lasers in optical fibers,» *JOSA B,* vol. 18, nº 10, pp. 1428-1435, 2001.

[82] C. Floridia, M. L. Sundheimer, L. d. S. Menezes y A. S. L. Gomes, «Optimization of spectrally flat and broadband single-pump fiber optic parametric amplifiers,» *Optics communications,* vol. 223, nº 4-6, pp. 381-388, 2003.

[83] J. M. C. Boggio, J. D. Marconi y H. L. Fragnito, «Double-pumped fiber optical parametric amplifier with flat gain over 47-nm bandwidth using a conventional dispersion-shifted fiber,» *IEEE photonics technology letters,* vol. 17, nº 9, pp. 1842-1844, 2005.

[84] P. Dainese, G. S. Wiederhecker, A. A. Rieznik, H. L. Fragnito y H. E. Hernandez-Figueroa, «Designing fiber dispersion for broadband parametric amplifiers,» de *IEEE-SBMO, International Microwave and Optoelectronics Conference (IMOC)*, 2005.

[85] J. M. C. Boggio, J. D. Marconi, S. R. Bickham y H. L. Fragnito, «Spectrally flat and broadband double-pumped fiber optical parametric amplifiers,» *Optics express,* vol. 15, nº 9, pp. 5288-5309, 2007.

[86] S. Pitois y G. Millot, «Experimental observation of a new modulational instability spectral window induced by fourth-order dispersion in a normally dispersive single-mode optical fiber,» *Optics communications,* vol. 226, nº 1-6, pp. 415-422, 2003.

[87] J. D. Harvey, R. Leonhardt, S. Coen, G. K. L. Wong, J. C. Knight, W. J. Wadsworth y P. S. J. Russell, «Scalar modulation instability in the normal dispersion regime by use of a photonic crystal fiber,» *Optics letters,* vol. 28, nº 22, pp. 2225-2227, 2003.

[88] M. E. Marhic, K. K. Y. Wong y L. G. Kazovsky, «Wide-band tuning of the gain spectra of one-pump fiber optical parametric amplifiers,» *IEEE Journal of Selected Topics in Quantum Electronics,* vol. 10, nº 5, pp. 1133-1141, 2004.

[89] A. Y. H. Chen, G. K. L. Wong, S. G. Murdoch, R. Leonhardt, J. D. Harvey, J. C. Knight, W. J. Wadsworth y P. S. J. Russell, «Widely tunable optical parametric generation in a photonic crystal fiber,» *Optics letters,* vol. 30, nº 7, pp. 762-764, 2005.

[90] X. Liu, Kuyken, R. G. B, R. Baets, R. M. Osgood Jr y W. M. Green, «Bridging the mid-infrared-to-telecom gap with silicon nanophotonic spectral translation,» *Nature Photonics,* vol. 6, nº 10, p. 667, 2012.

[91] B. Kuyken, P. Verheyen, P. Tannouri, X. Liu, J. Van Campenhout, R. Baets, W. M. J. Green y G. Roelkens, «Generation of 3.6 μm radiation and telecom-band amplification by four-wave mixing in a silicon waveguide with normal group velocity dispersion,» *Optics letters,* vol. 39, nº 6, pp. 1349-1352, 2014.

[92] R. Hui y M. O'Sullivan, Fiber optic measurement techniques, Academic Press, 2009.

[93] S. E. Mechels, J. B. Schlager y D. L. Franzen, «Accurate measurements of the zero-dispersion wavelength in optical fibers,» *Journal of research of the National Institute of Standards and Technology,* vol. 102, nº 3, p. 333, 1997.

[94] A. Gil-Molina, A. Perez-Ramirez, J. C. Ramirez, L. H. Gabrielli y H. L. Fragnito, «Shift of zero-dispersion wavelength in bent optical fibers,» *Optics express,* vol. 26, nº 6, pp. 6700-6714, 2018.

[95] M. Hirano, T. Nakanishi, T. Okuno y M. Onishi, «Silica-based highly nonlinear fibers and their application,» *IEEE Journal of Selected Topics in Quantum Electronics,* vol. 15, nº 1, p. 2009, 2009.

[96] J. A. Castañeda, MSc Thesis: Pulsed laser-noise interaction in optical fibers: application in maps of high- order dispersion, Campinas: Institute of Physics “Gleb Wataghin,” University of Campinas, 2012 (http://repositorio.unicamp.br/jspui/handle/REPOSIP/277935).

[97] Y. S. Jang y Y. C. Chung, «Four-wave mixing of incoherent light in a dispersion-shifted fiber using a spectrum-sliced fiber amplifier light source,» *IEEE photonics technology letters,* vol. 10, nº 2, pp. 218-220, 1998.

[98] F. Gholami, J. M. C. Boggio, S. Moro, N. Alic y S. Radic, «Measurement of ultra-low fourth order dispersion coefficient of nonlinear fiber by distant low-power FWM,» de *IEEE Photonics Society Summer Topical Meeting Series*, Playa del Carmen, Mexico, 2010.

[99] Y. Tamura, H. Sakuma, K. Morita, M. Suzuki, Y. Yamamoto, K. Shimada, Y. Honma, K. Sohma, T. Fujii y T. Hasegawa, «Lowest-ever 0.1419-dB/km loss optical fiber,» de *Optical Fiber Communication Conference*, Los Angeles, 2017.

[100] K. Byron, M. Bedgood, A. Finney, C. McGauran, S. Savory y I. Watson, «Shifts in zero dispersion wavelength due to pressure, temperature and strain in dispersion shifted singlemode fibres,» *Electronics Letters,* vol. 28, nº 18, pp. 1712-1714, 1992.

[101] A. A. Rieznik, T. Tolisano, F. A. Callegari, D. F. Grosz y H. L. Fragnito, «Uncertainty relation for the optimization of optical-fiber transmission systems simulations,» *Uncertainty relation for the optimization of optical-fiber transmission systems simulations,* vol. 13, nº 10, pp. 3822-3834, 2005.

[102] L. H. Gabrielli, H. E. Hernandez-Figueroa y H. L. Fragnito, «Robustness optimization of fiber index profiles for optical parametric amplifiers,» *Journal of Lightwave Technology,* vol. 27, nº 24, pp. 5571-5579, 2009.

[103] J. W. Fleming, «Dispersion in GeO2-SiO2 glasses,» *Applied Optics,* vol. 23, nº 24, pp. 4486-4493, 1984.

[104] S. H. Wemple, D. A. Pinnow, T. C. Rich, R. E. Jaeger y L. G. Van Uitert, «Binary SiO2-B2O3 glass system: Refractive index behavior and energy gap considerations,» *Journal of Applied Physics,* vol. 44, nº 12, pp. 5432-5437, 1973.

[105] A. Mussot, A. Kudlinski, R. Habert, I. Dahman, G. Mélin, L. Galkovsky, A. Fleureau, S. Lempereur, L. Lago, D. Bigourd y T. Sylvestre, «20 THz-bandwidth continuous-wave fiber optical parametric amplifier operating at 1 µm using a dispersion-stabilized photonic crystal fiber,» *Optics express,* vol. 20, nº 27, pp. 28906-28911, 2012.

[106] J. C. Boggio, S. Zlatanovic, F. Gholami, J. M. Aparicio, S. Moro, K. Balch, N. Alic y S. Radic, «Short wavelength infrared frequency conversion in ultra-compact fiber device,» *Optics Express,* vol. 18, nº 2, pp. 439-445, 2010.

[107] S. Zlatanovic, J. S. Park, S. Moro, J. M. C. Boggio, I. B. Divliansky, N. Alic, S. Mookherjea y S. Radic, «Mid-infrared wavelength conversion in silicon waveguides using ultracompact telecom-band-derived pump source,» *Nature Photonics,* vol. 4, nº 8, p. 561, 2010.

[108] S. J. Garth, «Effect of bending on zero dispersion operation of single-mode optical fibers,» *Applied optics,* vol. 30, nº 9, pp. 1048-1051, 1991.

[109] I. J. Blewett, «Effect of bending on chromatic dispersion of singlemode optical fibres,» *Electronics Letters,* vol. 30, nº 7, pp. 592-594, 1994.

[110] R. T. Schermer y J. H. Cole, «Improved bend loss formula verified for optical fiber by simulation and experiment,» *IEEE Journal of Quantum Electronics,* vol. 43, nº 10, pp. 899-909, 2007.

[111] R. T. Schermer, «Mode scalability in bent optical fibers,» *Optics Express,* vol. 15, nº 24, pp. 15674-15701, 2007.

[112] M. Heiblum y J. Harris, «Analysis of curved optical waveguides by conformal transformation,» *IEEE Journal of Quantum Electronics,* vol. 11, nº 2, pp. 75-83, 1975.

[113] L. Zhang, Y. Yue, R. G. Beausoleil y A. E. Willner, «Analysis and engineering of chromatic dispersion in silicon waveguide bends and ring resonators,» *Optics express,* vol. 19, nº 9, pp. 8102-8107, 2011.

[114] Q. Lin, T. J. Johnson, R. Perahia, C. P. Michael y O. J. Painter, «A proposal for highly tunable optical parametric oscillation in silicon micro-resonators,» *Optics express,* vol. 16, nº 14, pp. 10596-10610, 2008.

[115] R. Ulrich, S. C. Rashleigh y W. Eickhoff, «Bending-induced birefringence in single-mode fibers,» *Optics letters,* vol. 5, nº 6, pp. 273-275, 1980.

[116] B. Ainslie y C. Day, «A review of single-mode fibers with modified dispersion characteristics,» *Journal of lightwave technology,* vol. 4, nº 8, pp. 967-979, 1986.

[117] W. A. Reed, L. G. Cohen y H.-T. Shang, «Tailoring optical characteristics of dispersion-shifted lightguides for applications near 1.55 µm,» *Bell Labs Technical Journal,* vol. 65, nº 5, pp. 105-122, 1986.

[118] F. Wassmann, «Modal field analysis of circularly bent single-mode fibers,» *Journal of lightwave technology,* vol. 17, nº 5, pp. 957-968, 1999.

[119] P. Moin, «Chapter 2: Numerical Differentiation - Finite Differences,» de *Fundamentals of engineering numerical analysis*, New York, Cambridge University Press, 2010.

[120] W. A. Gambling, H. Matsumura y R. A. Sammut, «Mode shift at bends in single-mode fibres,» *Electronics Letters,* vol. 12, nº 23, pp. 695-697, 1977.

[121] A. Kudlinski, A. Mussot, R. Habert y T. Sylvestre, «Widely tunable parametric amplification and pulse train generation by heating a photonic crystal fiber,» *IEEE Journal of Quantum Electronics,* vol. 47, nº 12, pp. 1514-1518, 2011.

[122] E. Myslivets, C. Lundström, J. M. Aparicio, S. Moro, A. O. J. Wiberg, C.-S. Bres, N. Alic, P. A. Andrekson y S. Radic, «Spatial equalization of zero-dispersion wavelength profiles in nonlinear fibers,» *IEEE Photonics Technology Letters,* vol. 21, nº 21, p. 1807, 2009.

[123] A. Kudlinski, A. K. George, J. C. Knight, J. C. Travers, A. B. Rulkov, S. V. Popov y J. R. Taylor, «Zero-dispersion wavelength decreasing photonic crystal fibers for ultraviolet-extended supercontinuum generation,» *Optics Express,* vol. 14, nº 12, pp. 5715-5722, 2006.

[124] L. Chrostowski y M. Hochberg, Silicon photonics design: from devices to systems, Cambridge University Press, 2015.

[125] M. Lipson, «Guiding, modulating, and emitting light on silicon-challenges and opportunities,» *Journal of Lightwave Technology,* vol. 23, nº 12, p. 4222, 2005.

[126] H. K. Tsang y Y. Liu, «Nonlinear optical properties of silicon waveguides,» *Semiconductor Science and Technology,* vol. 23, nº 6, p. 064007, 2008.

[127] X. Liu, R. M. Osgood Jr, Y. A. Vlasov y W. M. Green, «Mid-infrared optical parametric amplifier using silicon nanophotonic waveguides,» *Nature Photonics,* vol. 4, nº 8, p. 557, 2010.

[128] R. L. Espinola, J. I. Dadap, R. M. Osgood, S. J. McNab y Y. A. Vlasov, «C-band wavelength conversion in silicon photonic wire waveguides,» *Optics express,* vol. 13, nº 11, pp. 4341-4349, 2005.

[129] W. Mathlouthi, H. Rong y M. Paniccia, «Characterization of efficient wavelength conversion by four-wave mixing in sub-micron silicon waveguides,» *Optics express,* vol. 16, nº 21, pp. 16735-16745, 2008.

[130] B. Kuyken, X. Liu, G. Roelkens, R. Baets, R. M. Osgood Jr y W. M. Green, «50 dB parametric on-chip gain in silicon photonic wires,» *Optics letters,* vol. 36, nº 22, pp. 4401-4403, 2011.

[131] I.-W. Hsieh, X. Chen, X. Liu, J. I. Dadap, N. C. Panoiu, C.-Y. Chou, F. Xia, W. M. Green, Y. A. Vlasov y R. M. Osgood, «Supercontinuum generation in silicon photonic wires,» *Optics express,* vol. 15, nº 23, pp. 15242-15249, 2007.

[132] R. K. Lau, M. R. Lamont, A. G. Griffith, Y. Okawachi, M. Lipson y A. L. Gaeta, «Octave-spanning mid-infrared supercontinuum generation in silicon nanowaveguides,» *Optics letters,* vol. 39, nº 15, pp. 4518-4521, 2014.

[133] N. Singh, D. D. Hudson, Y. Yu, C. Grillet, S. D. Jackson, A. Casas-Bedoya, A. Read, P. Atanackovic, S. G. Duvall, S. Palomba y B. Luther-Davies, «Midinfrared supercontinuum generation from 2 to 6 μm in a silicon nanowire,» *Optica,* vol. 2, nº 9, pp. 797-802, 2015.

[134] B. Kuyken, X. Liu, R. M. Osgood, R. Baets, G. Roelkens y W. M. J. Green, «Mid-infrared to telecom-band supercontinuum generation in highly nonlinear silicon-on-insulator wire waveguides,» *Optics Express,* vol. 19, nº 21, pp. 20172-20181, 2011.

[135] B. Kuyken, T. Ideguchi, S. Holzner, M. Yan, T. W. Hänsch, J. Van Campenhout, P. Verheyen, S. Coen, F. Leo, R. Baets y G. Roelkens, «An octave-spanning mid-infrared frequency comb generated in a silicon nanophotonic wire waveguide,» *Nature communications,* vol. 6, p. 6310, 2015.

[136] A. G. Griffith, R. K. Lau, J. Cardenas, Y. Okawachi, A. Mohanty, R. Fain, Y. H. D. Lee, M. Yu, C. T. Phare, C. B. Poitras, A. L. Gaeta y L. M, «Silicon-chip mid-infrared frequency comb generation,» *Nature communications,* vol. 6, p. 6299, 2015.

[137] M. A. Foster, J. S. Levy, O. Kuzucu, K. Saha, M. Lipson y A. L. Gaeta, «Silicon-based monolithic optical frequency comb source,» *Optics Express,* vol. 19, nº 15, pp. 14233-14239, 2011.

[138] H. K. Tsang, C. Wong, T. Liang, I. Day, S. Roberts, A. Harpin, J. Drake y M. Asghari, «Optical dispersion, two-photon absorption and self-phase modulation in silicon waveguides at 1.5 μm wavelength,» *Applied Physics Letters,* vol. 80, nº 3, pp. 416-418, 2002.

[139] K. Luke, Y. Okawachi, M. R. E. Lamont, A. L. Gaeta y M. Lipson, «Broadband mid-infrared frequency comb generation in a Si 3 N 4 microresonator,» *Optics letters,* vol. 40, nº 21, pp. 4823-4826, 2015.

[140] W. M J, Handbook of optical materials, Boca Raton: CRC Press, 2003.

[141] B. E. a. T. M. C. a. S. B. E. Saleh, «Chapter 5: Electromagnetic Optics,» de *Fundamentals of photonics*, New York, Wiley, 1991.

[142] A. Gil-Molina, I. Aldaya, J. L. Pita, L. H. Gabrielli, H. L. Fragnito y P. Dainese, «Optical free-carrier generation in silicon nano-waveguides at 1550 nm,» *Applied Physics Letters,* vol. 112, nº 25, p. 251104, 2018.

[143] I. Aldaya, A. Gil-Molina, J. L. Pita, L. H. Gabrielli, H. L. Fragnito y P. Dainese, «Nonlinear carrier dynamics in silicon nano-waveguides,» *Optica,* vol. 4, nº 10, pp. 1219-1227, 2017.

[144] T. Liang y H. Tsang, «Role of free carriers from two-photon absorption in Raman amplification in silicon-on-insulator waveguides,» *Applied Physics Letters,* vol. 84, nº 15, pp. 2745-2747, 2004.

[145] T. J. Johnson, M. Borselli y O. Painter, «Self-induced optical modulation of the transmission through a high-Q silicon microdisk resonator,» *Optics express,* vol. 14, nº 2, pp. 817-831, 2006.

[146] W. H. Pernice, M. Li y H. X. Tang, «Time-domain measurement of optical transport in silicon micro-ring resonators,» *Optics express,* vol. 18, nº 17, pp. 18438-18452, 2010.

[147] I. Aldaya, A. Gil-Molina, H. L. Fragnito y P. Dainese, «Time-domain interferometric characterization of nonlinear and thermal-induced phase-shift in silicon waveguides,» de *Conference on Lasers and Electro-Optics (CLEO)*, San Jose, 2016.

[148] S. Grillanda y F. Morichetti, «Light-induced metal-like surface of silicon photonic waveguides,» *Nature communications,* vol. 6, p. 8182, 2015.

[149] J. J. Ackert, A. S. Karar, D. J. Paez, P. E. Jessop, J. C. Cartledge y A. P. Knights, «10 Gbps silicon waveguide-integrated infrared avalanche photodiode,» *Optics Express,* vol. 21, nº 17, pp. 19530-19537, 2013.

[150] F. Morichetti, S. Grillanda, M. Carminati, G. Ferrari, M. Sampietro, M. J. Strain, M. Sorel y A. Melloni, «Non-invasive on-chip light observation by contactless waveguide conductivity monitoring,» *IEEE Journal of Selected Topics in Quantum Electronics,* vol. 20, nº 4, pp. 292-301, 2014.

[151] S. M. Sze y K. K. Ng, Physics of semiconductor devices, Hoboken: John Wiley & Sons, 2007.

[152] D. Dimitropoulos, R. Jhaveri, R. Claps, J. Woo y B. Jalali, «Lifetime of photogenerated carriers in silicon-on-insulator rib waveguides,» *Applied Physics Letters,* vol. 86, nº 7, p. 071115, 2005.

[153] A. D. Bristow, N. Rotenberg y H. M. Van Driel, «Two-photon absorption and Kerr coefficients of silicon for 850--2200 nm,» *Applied Physics Letters,* vol. 90, nº 19, p. 191104, 2007.

[154] Q. Lin, J. Zhang, G. Piredda, R. W. Boyd, P. M. Fauchet y G. P. Agrawal, «Dispersion of silicon nonlinearities in the near infrared region,» *Applied physics letters,* vol. 91, nº 2, p. 021111, 2007.

[155] M. Dinu, F. Quochi y H. Garcia, «Third-order nonlinearities in silicon at telecom wavelengths,» *Applied physics letters,* vol. 82, nº 18, pp. 2954-2956, 2003.

[156] X. Liu, J. B. Driscoll, J. I. Dadap, R. M. Osgood, S. Assefa, Y. A. Vlasov y W. M. Green, «Self-phase modulation and nonlinear loss in silicon nanophotonic wires near the mid-infrared two-photon absorption edge,» *Optics express,* vol. 19, nº 8, pp. 7778-7789, 2011.

[157] C. Monat, B. Corcoran, D. Pudo, M. Ebnali-Heidari, C. Grillet, M. D. Pelusi, D. J. Moss, B. J. Eggleton, T. P. White y L. O'Faolain, «Slow light enhanced nonlinear optics in silicon photonic crystal waveguides,» *IEEE Journal of Selected Topics in Quantum Electronics,* vol. 16, nº 1, pp. 344-356, 2010.

[158] R. Claps, D. Dimitropoulos, V. Raghunathan, Y. Han y B. Jalali, «Observation of stimulated Raman amplification in silicon waveguides,» *Optics express,* vol. 11, nº 15, pp. 1731-1739, 2003.

[159] H. Tsang, P. Snow, I. Day, I. White, R. Penty, R. Grant, Z. Su, G. Kennedy y W. Sibbett, «All-optical modulation with ultrafast recovery at low pump energies in passive InGaAs/InGaAsP multiquantum well waveguides,» *Applied physics letters,* vol. 62, nº 13, pp. 1451-1453, 1993.

[160] R. A. Soref y B. R. Bennett, «Electrooptical effects in silicon,» *IEEE journal of quantum electronics,* vol. 23, nº 1, pp. 123-129, 1987.

[161] G. W. Rieger, K. S. Virk y J. F. Young, «Nonlinear propagation of ultrafast 1.5 μm pulses in high-index-contrast silicon-on-insulator waveguides,» *Applied physics letters,* vol. 84, nº 6, pp. 900-902, 2004.

[162] K. Kondo y T. Baba, «On-chip autocorrelator using counter-propagating slow light in a photonic crystal with two-photon absorption photodiodes,» *Optica,* vol. 4, nº 9, pp. 1109-1112, 2017.

[163] J. S. Blakemore, Semiconductor statistics, Courier Corporation, 2002.

[164] W. Shockley y W. Read Jr, «Statistics of the recombinations of holes and electrons,» *Physical review,* vol. 87, nº 5, p. 835, 1952.

[165] A. G. Aberle, S. Glunz y W. Warta, «Impact of illumination level and oxide parameters on Shockley--Read--Hall recombination at the Si-SiO2 interface,» *Journal of Applied Physics,* vol. 71, nº 9, pp. 4422-4431, 1992.

[166] W. Shockley y J. Last, «Statistics of the charge distribution for a localized flaw in a semiconductor,» *Physical Review,* vol. 107, nº 2, pp. 392-396, 1957.

[167] K. C. Nomura y J. S. Blakemore, «Decay of excess carriers in semiconductors,» *Physical Review,* vol. 112, nº 5, pp. 1607-1615, 1958.

[168] K. C. Nomura y J. S. Blakemore, «Decay of excess carriers in semiconductors. II,» *Physical Review,* vol. 121, nº 3, pp. 734-740, 1961.

[169] K. K. Lee, D. R. Lim, H.-C. Luan, A. Agarwal, J. Foresi y L. C. Kimerling, «Effect of size and roughness on light transmission in a Si/SiO2 waveguide: Experiments and model,» *Applied Physics Letters,* vol. 77, nº 11, pp. 1617-1619, 2000.

[170] H. a. B. C. a. A. A. G. Nagel, «Generalized analysis of quasi-steady-state and quasi-transient measurements of carrier lifetimes in semiconductors,» *Journal of Applied Physics,* vol. 86, nº 11, pp. 6218-6221, 1999.

[171] E. Yablonovitch y T. Gmitter, «Auger recombination in silicon at low carrier densities,» *Applied physics letters,* vol. 49, nº 10, pp. 587-589, 1986.

[172] P. J. Caplan, E. H. Poindexter, B. E. Deal y R. R. Razouk, «ESR centers, interface states, and oxide fixed charge in thermally oxidized silicon wafers,» *Journal of applied Physics,* vol. 50, nº 9, pp. 5847-5854, 1979.

[173] R. N. Hall, «Electron-hole recombination in germanium,» *Physical review,* vol. 87, nº 2, p. 387, 1952.